Fall 2013

Mechanisms of Microstructure Formation Under the Influence of Ultrasonic Vibrations

Milan Rakita
Purdue University

Graduate School ETD Form 9
(Revised 12/07)

PURDUE UNIVERSITY
GRADUATE SCHOOL
Thesis/Dissertation Acceptance

This is to certify that the thesis/dissertation prepared

By Milan Rakita

Entitled
Mechanisms of Microstructure Formation Under the Influence of Ultrasonic Vibrations

For the degree of Doctor of Philosophy

Is approved by the final examining committee:

Qingyou Han
Chair

David R. Johnson

Xiaoming Wang

Richard M. French

To the best of my knowledge and as understood by the student in the *Research Integrity and Copyright Disclaimer (Graduate School Form 20)*, this thesis/dissertation adheres to the provisions of Purdue University's "Policy on Integrity in Research" and the use of copyrighted material.

Approved by Major Professor(s): Qingyou Han

Approved by: James L. Mohler 12/02/2013
Head of the Graduate Program Date

MECHANISMS OF MICROSTRUCTURE FORMATION UNDER THE INFLUENCE OF ULTRASONIC VIBRATIONS

A Dissertation

Submitted to the Faculty

of

Purdue University

by

Milan Rakita

In Partial Fulfillment of the

Requirements for the Degree

of

Doctor of Philosophy

December 2013

Purdue University

West Lafayette, Indiana

ACKNOWLEDGMENTS

I would like to thank my advisor Dr. Qingoyu Han for his unconditional support, encouragement, unlimited patience, trust in me, and countless insightful discussions from which I learned a lot. His scientific enthusiasm and need to know why and how things work served me as an inspiration to persevere. I am indebted to Dr. Mark French for giving me a high-speed camera on indefinitely long use. This piece of equipment turned out to be the main tool in this research. The best course I have taken in my rich student career is Solidification of Castings, taught by Dr. David Johnson, and I am grateful for that. Thanks to Dr. Xiaoming Wang for accepting on short notice to serve as my committee member and giving very useful help.

I am indebted to Dr. Mileta Tomovic, who accepted me to graduate studies here. His knack for future trends has always impressed me. He also gave me a chance to work for TAP, where I truly enjoyed collaboration and support from him, Dr. David McKinnis, Mr. Randy Hountz, Ms. Karen Leaman, and Ms. Mary Prill. I am thankful to all those people. Thank you, Vukica and Sreten, for all the help and good times.

I have to acknowledge a great influence of Dr. Damir Kakas and Dr. Leposava Sidjanin from University of Novi Sad, and great colleagues from Vinca Institute of Nuclear Sciences led by Dr. Aleksandar Dobrosavljevic and Dr. Nebojsa Neskovic.

My true love and gratitude goes to my wife Mariya and our daughter Ana for their love, constant support and encouragement in whatever I do. Their cheerfulness and creativity to live full and enjoyable life and have a great time, not just wait for me to graduate, kept my spirit always up. My parents Sima and Dragomir, and sister Milena, and my wife's parents Elena and Boris gave us tremendous help, both moral and financial. Recent visit from my mother was crucial in finishing this dissertation, finally. Financial help from Elena and Boris throughout these years was far more than generous.

TABLE OF CONTENTS

Page

Page

LIST OF TABLES

Table Page

LIST OF FIGURES

Figure Page

Figure Page

Figure Page

Figure Page

Figure Page

Figure Page

Figure Page

Figure Page

Figure Page

Figure Page

Figure Page

Figure Page

Figure Page

ABSTRACT

Rakita, Milan. Ph.D., Purdue University, December 2013. Mechanisms of Microstructure Formation Under the Influence of Ultrasonic Vibrations. Major Professor: Qingyou Han.

Positive effects of ultrasound on crystallization have been known for almost 90 years. Application of ultrasound has been very successful in many industries, most notably in chemistry, creating a new branch of science – sonochemistry. However, ultrasonication has not found wide commercial application in the solidification processing. The reason for that is the complexity of underlying phenomena and the lack of predicting models which correlate processing parameters with the properties of a product. The purpose of this study is to give some contribution toward better understanding of mechanisms that lead to changes in the solidifying microstructure. It has been found that, under experimental conditions used in this work, cavitation-induced nucleation is the major contributor to the grain refinement. Ultrasonication at minimal supercoolings is expected to give maximal grain refinement. Dendrite fragmentation has not shown to be a significant contributor to the grain refinement. Dendrite fragmentation is maximal if done by bubbles that come in contact with the solidifying phase, or that are created there. Alloys/solutions with long solidification interval, or wide mushy zone, are expected to exhibit more dendrite fragmentation. Bubbles are recognized as a crucial feature in ultrasonication. Their size distribution in the liquid phase prior to ultrasonication dictates the cavitation threshold and intensity of cavitation. For the first time, radiation pressure has been recognized as potentially significant factor in grain refinement. In the experimental setup used in this study, acoustic pressure at the main (driving) frequency is not substantial to cause significant fragmentation, and only dendrites close to the sonotrode were fragmented. However, application of ultrasound with frequencies that are

several times higher than the current industrial practice could substantially increase dendrite fragmentation. Appearance of fractional harmonics has also been recognized for the first time as potentially influential factor. The amplitude of pressure caused by these vibrations is quite sensible, and since resonant in nature, these pressure variations propagate throughout entire liquid volume. Although ultrasonication is a very efficient method for degassing melts, there is a risk of gas entrapment if ultrasound is applied during solidification. Heating can create unwanted effects during ultrasonication at small supercoolings.

CHAPTER 1. INTRODUCTION

1.1. Statement of the Problem

It has been known for decades that a metal which solidifies when exposed to high-intensity ultrasonic vibrations may get microstructure that cannot be obtained under conventional solidification conditions. For example, many metals naturally form dendritic structure during solidification (Kurz & Fisher, 1998; Flemings, 1974). Hot tearing, the most frequent and yet not well explained defect in castings, is connected with the existence of dendrites (Campbell, 2000). However, if the same material is treated with high-intensity ultrasonic vibrations during solidification, instead of dendritic, a completely equiaxed structure can be achieved (Eskin, 1994; Eskin, 1998; Eskin, 2001; Jian, Xu, Meek, & Han, 2005). It has been observed that materials otherwise prone to hot tearing do not experience this defect if they develop a structure without dendrites (Eskin, 2001).[1] Potentially efficient way to achieve such structure is by the application of ultrasonic vibrations. Other benefits are better mechanical properties of as-cast material.

The topic of ultrasonically controlled solidification has regained increased interest over the past two decades, and that coincided with two trends. One trend is emergence of the single-bubble sonoluminescence (Gaitan, Crum, Church, & Roy, 1992),[2] which renewed interest in cavitation and bubble dynamics. Another trend is a series of publications from Russian scientists on positive effects of ultrasonication. Maybe the best

---

[1] Although hot tearing still may occur in materials with non-dendritic structure, this danger is greatly reduced or eliminated in most materials.

[2] Sonoluminescence has been known for decades, but research efforts have been directed to clouds of bubbles. The new trend started by the group of Lawrence Crum was to capture a single bubble in the ultrasonic field and drive it into stable cavitation regime.

known authors in this area are O. V. Abramov and G. I. Eskin (Abramov O. V., 1987; Abramov O. V., 1998; Abramov V. O., Abramov O. V., Bulgakov, & Sommer, 1998; Abramov V. O., Abramov O. V., Straumal, & Gust, 1997; Eskin, 1994; Eskin, 2001). It is interesting that many of these publications contain results that are a few decades old.

Two phenomena are recognized as the main contributors to changes in solidified microstructure which is exposed to the ultrasonic filed; they are increased nucleation rate and dendrite fragmentation. Chalmers (1964) stated that there is no decisive way to give a preference to either of these two mechanisms. It seems that agreement has not been reached today. For example, Glicksman (2011) recognizes fragmentation of dendrites as the main reason for grain refinement by ultrasonication, while Qian et al. (2009) concluded that fragmentation of crystals is not significant contributor and gave preference to increased nucleation rate.

It is widely agreed upon that high pressures in the liquid phase developed during the collapse and rebound of cavities increase nucleation rate. It is also believed that acoustic streaming, a convection forced by applied ultrasonic vibrations, helps fragmentation of growing dendrites as other methods of mechanical stirring have.[3] In addition to acoustic streaming, it has been reported that bubbles can fragment growing dendrites when they come in contact (Swallowe, Fields, Rees, & Duckworth, 1989; Chow, Blindt, Kamp, Grocutt, & Chivers, 2004; Shu, Sun, Mi, & Grant, 2012). However, lack of agreement about the importance of different processes that occur in the melt with the presence of the ultrasonic field, and quantification, might have been the reason which has prevented wide industrial use of the high-intensity ultrasonic vibrations in solidification processing.

---

[3] Convection itself does not break dendrites, but helps remelting dendrites in their roots (Jackson, Hunt, Uhlmann, & Seward, 1966; Paradies, Kim, Glicksman, & Smith, 1993; Paradies, Smith, & Glicksman, 1997; Glicksman M. E., 2011).

1.2. Research Questions

According to previous section, the following questions naturally arise:

1. What is the main contributor to observed grain refinement when ultrasound is applied: increased nucleation rate or fragmentation of dendrites?
2. How much is nucleation rate increased by ultrasonically induced cavitation?
3. How much is acoustic streaming effective in dendrite fragmentation?
4. How effective are bubbles in the fragmentation of dendrites?
5. Are there some other phenomena associated with the ultrasonic filed in liquids that could contribute grain refinement, but have not been credited so far?

1.3. Significance of the Problem

Effects of ultrasonic have been studied for almost 90 years, since the pioneering work of Richards and Loomis (1927). Since then, application of ultrasonic fields has found many applications in materials processing, like chemical industry, electrochemistry, plating, welding, machining, metal working, heat treatment, powder metallurgy, metalcasting, and others (Abramov, 1998; Shah, Pandit, & Moholkar, 1999). However, a good control of solidification processes during ultrasonication has not been achieved so far, rendering very limited industrial application of ultrasound in metalcasting comparing to other above mentioned fields.

A better understanding of the solidification mechanisms influenced by the ultrasonic field and well-described correlations between physical mechanisms and processing parameters should certainly contribute to the materials processing society with wider application of this technology. Solidification under the influence of ultrasonic vibrations is a promising technology capable of providing products with much better properties compared to existing solidification technologies. Eskin (2001) recently showed a picture of a ten-ton ingot from A2324 aluminum alloy with completely refined grains. Earlier, he showed a scheme of the continuous casting process aided by ultrasonication (Eskin, 1994). On the other hand, results of Qian et al. (2009) indicate that it may be difficult to obtain grain refinement even in a small laboratory sample; uniformity of

refined grains is even harder to achieve. Glicksman (2011) even renders ultrasonic grain refinement as impractical. This illustrates the level of disagreement between researchers in this field, and that many unknowns still exist.

Besides its many positive effects on the structure development, improper application of high-intensity ultrasound during solidification can cause detrimental effects on the structure and result in completely defective part.

1.4. Purpose of the Study

The purpose of this study is to shed more light on the questions listed in Section 1.2. It has been accomplished by in-situ observation of solidification while ultrasound is applied. These observations are correlated with rough estimations calculated using accepted models for nucleation, cavitation, and propagation of sound in liquids.

In order to observe solidification in-situ, transparent materials have been used. Of the main concern in this study are processes of nucleation and dendrite fragmentation, so the morphology of the solid phase is of no importance here. Hence it is actually not essential to study transparent metal analogs. For that reason water will be the main medium to study, mostly because of its well-known physical properties. In addition to water, succinonitrile (SCN) and aqueous solution of ammonium chloride will be used. Since both of them solidify analogously to metals, there might be some phenomena observed during ultrasonication that could apply to metals.

1.5. Assumptions

There are many assumptions in this work. The main assumption is that the results presented here faithfully represent physical processes they are describing, and those physical processes will occur with great probability under the same or similar conditions in an environment different, in dimensional scale, in materials used, and other aspects, from the experimental setup in this study. In other words, conclusions made here are assumed to be universal enough so inductive conclusion can be made.

Errors in measurements, mostly temperature, are considered to be too small to influence conclusions based on their readings. Theoretical background used to explain observations is assumed to be sound enough.

There are many theoretical models used in this study, and all of them are based on a large number of assumptions and simplifications. It would be redundant and tedious to pool all the assumptions in this section, so they will be defined throughout the text where appropriate. The most common are those of continuity and isotropy of the medium which is modeled. As some examples, bubbles are assumed to consist of ideal gas and the pressure is constant throughout the bubble; surface tension has the value of the bulk and is constant; disturbances through a fluid propagate with the velocity that is the sum of the velocity of sound in that fluid and the velocity of the fluid itself; and so on.

The assumption of the author's good enough understanding of all the physical processes mentioned in this work, and omitted yet pertinent to this study, is implied.

1.6. Limitations

The main limitation in this research is that nucleation is actually very hard, if possible at all,[4] to detect. Only nuclei that have grown to the large enough size can be detected. Hence many observation and estimations will be indirectly linked to nucleation.

Another limitation represents temperature measurement, since thermocouples disturb temperature field around them (Beck, 1968) and also conduct heat along their leads (Singh & Dybbs, 1976; Satyamurthu, Marwah, Venkatramani, & Rohatgi, 1979). This limitation is minimized by performing the main part of experiment, ultrasonication, when temperature filed in the sample has stabilized, so errors are expected to be a fraction of a degree. In experiments with spontaneous (thermal) nucleation, cooling rate was very slow so, again, expected errors are minimal.

---

[4] Neutron scattering seems to be the most promising method for this purpose, although it is not free from its own problems and limitations.

Initial density of gas bubbles was found to be the main source of variations in experiments, although experiments very repeatable. For example, cavitation and nucleation of solid phase can vary depending on prior degassing of the liquid. It was found that if water had been heavily degassed before ultrasonication, higher acoustic intensity was needed to induce cavitation and nucleation of ice. This limitation was minimized by preparing each liquid sample using the same routine.

1.7. Delimitations

All the assumptions and limitations stated above can be combined in delimitations. Some of the main delimitations are:

1. No special measures were undertaken for controllable degassing of the liquid phase, or to control the density of gas bubbles. The only measure of precaution was to use identical procedure to measure the volume and pour the liquid in the test tube, so it was assumed that different samples are aerated similarly.
2. Only elementary shape of container is used, and that is a test tube. No attempts were made to perform ultrasonication in containers with more complex shape.
3. Solidification processes are observed in a small volume, 14.1 to 16.2 mm in diameter and around 90 mm in length.
4. Only one power input was used, 120 W.
5. Effects of ultrasound on metals are not studied in this work. Only transparent liquids are studied.
6. Experiments in this work were not designed by any method of the design of experiments for statistical analysis.
7. Effects of vibrations of the container walls are neglected. It has been observed that it is vibrations in the liquid that make the influence on the solidification process.

CHAPTER 2. LITERATURE OVERVIEW

The aim of this work is to shed more light on the influence of the ultrasonic field on the microstructure of solidifying materials. Having that in mind, this chapter is organized according to the following logic. First, basics of cavitation phenomena and basic equations which describe cavitation will be reviewed. Since cavitation models are not limited to a specific cause of cavitation, the author found justifiable to analyze this topic first. After the most important cavitation models are presented, a brief overview of the theory of propagation of acoustic waves in fluids will be given, but with attention focused on physical parameters learned to be important for existence of cavitation and ultrasound. After short analysis of the theory of nucleation and crystal growth, we have basic building blocks for the present study. The last section of this chapter is devoted to the complex interplay of these elementary blocks: to the influence of vibrations and cavitation imposed to the liquid on the way the microstructure will form. That section should serve as a statement of current state-of-the-art.

2.1. Acoustic Cavitation

2.1.1. Introduction

As illustrated in Figure 2.1, a liquid, which is in its initial state 1, can turn into vapor either if its temperature is increased above the boiling point or if its pressure is decreased below the value of the vapor pressure p_V. The latter case, evaporation of the liquid phase in the region of localized pressure drop, is called cavitation.

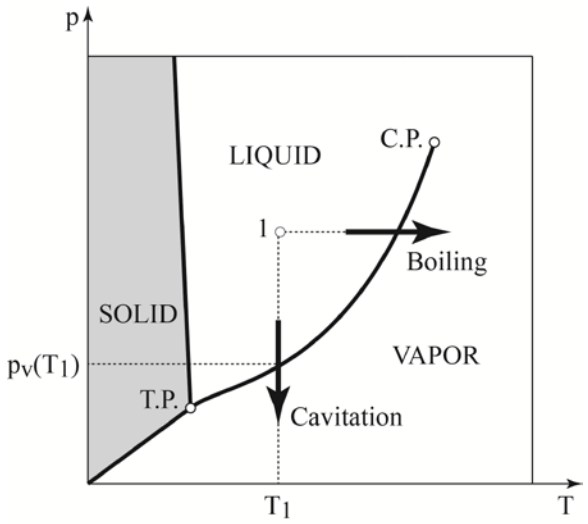

Figure 2.1. A sketch of the phase diagram for water. The liquid and vapor phases are separated between the triple point (T.P.) and the critical point (C.P.). Reproduced from Franc and Michel (2004).

2.1.2. Cavitation Nuclei, Their Stability, and Cavitation Inception

A cavity can nucleate in the liquid, or more favorably, grow from existing nucleus, which is usually a gas bubble. In analogy with solidification theory, the former case can be termed as homogeneous and the latter as heterogeneous cavity nucleation.

Normally, the pressure in the bulk of the liquid, p_∞, is higher than its vapor pressure, p_V. In Figure 2.2 that would be somewhere on the line AB if the liquid is at temperature T_1. In order to trigger cavitation, the pressure in the bulk of liquid, p_∞, has to drop locally to the value of vapor pressure or below ($p_\infty < p_V$), which would be somewhere on the line BE in Figure 2.2.

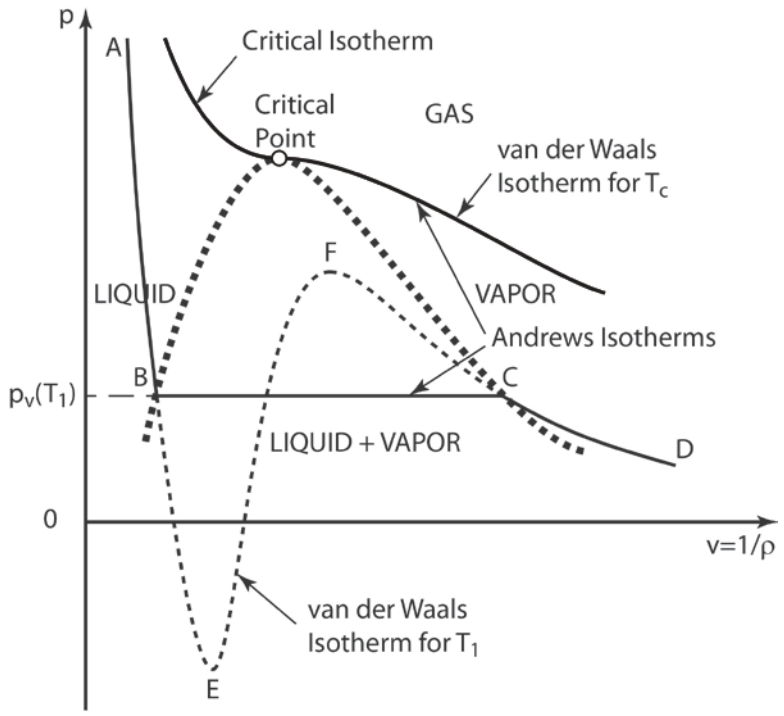

Figure 2.2. Phase diagram shown in the pressure – specific volume coordinates. Experimental (Andrews) and theoretical (van der Waals) isotherms are shown. Thick dotted curve are liquid and vapor binodal curves. The sketch is based on illustrations in the books by Fermi (1956), Brennen (1995), and Franc and Michel (2004).

As theoretically predicted by van der Waals model (curve ABEFCD in Figure 2.2), vaporization (cavity inception) can happen not before the pressure reaches some magnitude which is lower than p_V. Since the vapor pressure is relatively low, e.g. 2.3 kPa for water, the liquid actually has to be exposed to tension before its rupture. Hence, the liquid can theoretically withstand negative pressure, in other words tension, before it breaks, which is indeed observed in practice. Matter of fact, the BE part of the isotherm can be achieved in practice (Brennen, 1995).

On the other hand, if there are appropriate nuclei in just formed low-pressure region that can be activated at pressure p_V, cavitation could commence at point B, or much closer to it, and the liquid in that zone will continue to follow line BC – in other words the liquid will evaporate and increase its specific volume in order to keep constant vapor pressure.

By a simple calculation (Brennen, 1995; Frenkel, 1955), one can estimate theoretical pressure for the liquid rupture as $p_T = -K\left(\Delta V / V_0\right)$. Based on that, the latent heat is $\Delta H_V = \left|p_T\right| \Delta V / 12$, and the critical temperature $T_{CP} = \Delta H_V / k_B$. Here K is the bulk modulus (assumed 10^{10} – 10^{11} Pa), k_B is Boltzmann's constant, and $\Delta V / V_0 \approx 1/3$ is estimated change of volume at the moment of rupture. Equilibrium distance between molecules was assumed as 10^{-10} m. This calculation gives a quite good estimations of the orders of magnitude of the latent heat of vaporization, ΔH_V, and the critical temperature, T_{CP}, using theoretically predicted negative pressure (tension) at rupture, p_T. However, the predicted tension p_T itself is far from what is observed in experiments. Obtained negative pressure p_T of the order of 10^9 Pa (Frenkel, 1955), or $3 \cdot 10^9$ to $3 \cdot 10^{10}$ Pa (Brennen, 1995), is several orders of magnitude higher than practically observed values. Briggs (1949) measured 223±5 atmospheres for water at 25°C, which is around $2.26 \cdot 10^7$ Pa. With refined experiment with water, he measured limiting negative pressure of water at temperatures 0 to 50 °C (Briggs, 1950). The minimal value of around $2 \cdot 10^6$ Pa was obtained at 0°C and maximal, $2.77 \cdot 10^7$ Pa, at 10°C. This is the highest negative pressure reported in the literature for water (Leighton, 1994). For example, Willard (1953) generated cavitation using ultrasonic vibrations, and estimated tensions to be 20 atmospheres (roughly $2 \cdot 10^6$ Pa) or less for most cavitation bursts, certainly not exceeding 70 atmospheres.

The explanation for so large discrepancy between theoretically estimated and practically observed tensile strength of liquids is that the liquid ruptures at the sites of its "weakness", much sooner than the maximal tension is reached. These weak spots are cavitation nuclei. Both deviation from theoretical predictions and large variations in published experimental results for the tensile strength of liquids are addressed to the differences in the density of cavitation nuclei due to great sensitivity to experimental preparation (Franc & Michel, 2004). Willard (1953) notes that "initiation phase may start whenever a sufficiently weak nucleus enters the high intensity core of the sonic field". He observed much stronger cavitation in aerated than in degassed water.

Theoretical analysis of homogeneous nucleation of a cavity given in the literature, for example by Lubetkin (2004), is very similar to the treatment given for solidification. The difference is that work done in compressing the gas bubble has to be taken into account. Since this work can be neglected in case of the nucleation of solids, expressions for the critical radius and nucleation rate are different for bubbles and solids (Chalmers, 1964).[5] A reason why this topic is not discussed in this section is that the cavitation inception practically observed is in a quite big discrepancy with this theory, since the presence of gas bubbles in the liquid decreases critical negative pressure p_T by a two-fold action. The first effect is smaller energy required to create a cavity with the critical radius if there already exists an embryo with some initial radius. The other effect might be that the mixture of a gas with vapor decreases surface tension at the cavity surface. Massoudi and King (1974) showed that interfacial surface tension of water decreases with increased pressure of gases in contact with it.

Large discrepancy between theoretical and experimental tensile strengths of liquids can be resolved by postulating the existence of nuclei (Cha, 1981). This idea is very old, but maybe among the first ones to bring this problem to attention are Harvey et al. (1944a; 1944b), and probably the first to quantify conditions for the cavitation inception is F.G. Blake in 1949.[6] However, existing theories strongly reject the hypothesis of small stable bubbles. Eriksson and Ljunggren (2004) give an overview of rigorous thermodynamic models and conclude that a bubble can be stable only as a thermodynamically closed system. A thermodynamically closed system excludes any mass exchange across the boundary by its definition, so the stability of bubbles is implied.

---

[5] The nucleation of the solid phase is briefly discussed in Section 2.3.

[6] Blake, F. (1949). *The Onset of Cavitation in Liquids.* Boston: Acoustical Reserch Laboratory, Harvard University. The original work by Blake is not available to the author of this text. Fortunately, it is frequently cited so one can get some insight in it.

Stability of a gaseous cavitation nucleus or a bubble in general, is a very interesting topic. There are a few approaches in treatment of this problem, the main being thermodynamic, fluid dynamics, and diffusion approaches.

Based on experimental measurements and thermodynamic calculations, Mori et al. (1977) concluded that a bubble can stable only in sufficiently small volume of liquid. Based also on thermodynamic analysis, Cha (1981) obtained a relationship between the bubble radius and surrounding pressure where a bubble is stable. However, concentration of the system simulated is only of the order of 10^{-10} gram-moles. This is roughly $1.8 \cdot 10^{-15}$ m^3 for water, which is equivalent to a droplet of 7.5 μm in diameter. That means the system analyzed by Cha is actually even smaller than in the work by Mori et al., who used a bubble of about 0.2 mm in diameter. Same result can be obtained using diffusion approach. Namely, the bubble will dissolve partially in a very small amount of liquid and supersaturate it with gas up to the point when concentrations in the liquid and at the bubble-liquid interface become the same. Then, what has left of the bubble will remain stable. Of course, only a minute amount of liquid can be supersaturated with the gas from a bubble without its complete dissolution.

In a classic work of Epstein and Plesset (1950; 1951), bubble stability was analyzed considering diffusion along the surface of a stationary bubble in the stationary liquid under quasi-static approximation. Their model predicts that a bubble with 1 μm radius will dissolve in a fraction of a second, depending on the gas concentration in liquid. Other diffusion models show similar dissolution times. Since large bubbles with longer dissolution times go out of the liquid due to buoyancy, and micron-sized bubbles which could remain in the liquid are predicted to dissolve very quickly, it turns out that no bubble can exist in the bulk of the liquid.

It is evident from everyday life that bubbles can be very stable in a liquid. We all can observe air bubbles existing for hours or days on the walls of a glass filled with tap water, even bubbles smaller than one millimeter. Yount et al. (1984) recorded the existence of bubbles from 1 μm in diameter down to nanometer range in water and gelatin using the light end electron microscopy, while Johnson and Cooke (1981) produced stable bubbles in seawater. Similarly, Liebermann (1957) finds that air bubbles

smaller than 1 μm can persist in water indefinitely and it is not easy to eliminate them. Moreover, it is reported that micro and nanoscale bubbles can survive even ultrasonically generated pressure field (Borkent, Dammer, Schoenherr, Vancso, & Lohse, 2007; Mastikhin & Newling, 2008).

Since surface tension is usually recognized as the most detrimental factor to the lifetime of bubbles, majority of the theories which try to prolong predicted bubble life find some compensation for the Young- Laplace pressure. Throughout the years many conjectures about the existence of some kind of protective layer at the bubble-liquid boundary have emerged, for example a gas-impermeable organic layer (Fox & Herzfeld, 1954), some kind of surface-active molecules which become impermeable for the gas when highly compressed (Yount, Gilary, & Hoffman, 1984), or contaminant films which provide low contact angles and stability of air bubbles on hydrophobic surfaces (Ducker, 2009; Das, Snoeijer, & Lohse, 2010). Above mentioned Liebermann (1957) and Johnson and Cooke (1981) also reported what they believed is a layer at the surface of persistent bubbles. Yet, no consensus exists among experts about what this surfactant might be.

There are still ongoing efforts to explain existence of bubbles in the bulk of liquid phase without influence of some extraneous material. For example, Kloek et al. (2001) combined Epstein-Plesset diffusion model with interfacial rheology, and calculated that bubble dissolution can be stopped if either the interface or bulk are completely elastic. Recently, Corti et al. (2011) proposed that nanosized bubbles and droplets actually have negative surface tension, and that provides their stability. They performed thermodynamic analysis without taking bulk properties into account. On contrary, bulk properties are almost exclusively used in theoretical models.

There are two explanations for the existence of stable bubbles that are most accepted.[7] One is already mentioned existence of some surfactants around bubbles. The

---

[7] One might consider stability, or prolonged life, of bubbles containing multiple gases, where some of the component gases are insoluble in the liquid phase, or have very low solubility. Examples of dissolution curves in these cases can be found in the literature (Greene & Gaffney, 1959; Weinberg & Subramanian, 1980; Yung, De Witt, Brockwell, McQuillen, & Chai, 1988).

other explanation is that gas bubbles are attached to the container walls or hydrophobic particles dispersed in the liquid, probably suggested first by Harvey et al. (1944a; 1944b; 1947).

Rough substrate surfaces suitable for heterogeneous nucleation are usually represented with two elementary shapes: a depression or protrusion with conical or spherical shape. Wilt (1986) analyzed spontaneous bubble nucleation in supersaturated solution of CO_2 in water, and obtained that nucleation is not likely to occur on projections, both conical and spherical. According to Cole (1974), large wetting angle between the liquid and wall, and small apex angle of the conical pit or smaller radius of a spherical well favor bubble nucleation. This means that the smaller the crevice the more effective nucleation site it is. Wilt (1986) obtained similar results. His numerical calculations showed only conical crevice is favorable for bubble nucleation if the wetting angle is between 94 and 130° in appropriate combination with the apex angle, so the nucleus is concave or only slightly convex. A detailed derivation of pre-exponential factor for the nucleation in crevices can be found in the article by Cole (1974).

A popular topic in the last two decades has been the stability of nanoscale sized bubbles and pancakes observed on hydrophobic surfaces. On one side there are experimental observations of their existence, while on the other side there is strong denial by the mainstream theories. Only models which suggest stabilization of bubbles by surfactants and solid particles seem to avoid serious criticism. However, no one ever managed to extract any substance which might serve as a stabilizing surfactant. Moreover, taking into account some average density of bubbles found in liquids [see for example O'Hern et al. (1988), Brennen (1995)], the author of this work believes that amount of this stabilizing substance should be too large to go undetected with modern equipment.

Lack of a model for stable bubbles (cavitation nuclei) seems to deprive the cavitation theory from having a rigorous initial condition. This was overcome to some extent by Blake, who defined the limiting quasi-static ambient pressure and the critical radius beyond which a bubble can become a cavity. This threshold pressure and radius have many interpretations; two of them are straightforwardly presented and are adopted

here. The one is by Noltingk and Neppiras (1950; Neppiras & Noltingk, 1951), used also by Young (1989), and the other is by Brennen (1995). The Blake critical radius can be defined as (Brennen, 1995)

$$r_B = \sqrt{\frac{9\kappa m_b T_b R_{gas}}{8\pi\gamma}} \qquad \text{Eq. 2.1}$$

and the peak negative acoustic pressure, the Blake threshold pressure (Brennen, 1995):

$$p_B = p_V - \frac{4\gamma}{3}\sqrt{\frac{8\pi\gamma}{9\kappa m_b T_b R_{gas}}} \qquad \text{Eq. 2.2}$$

Here, κ, m_b, T_b, R_{gas}, γ, and p_V are the polytropic index, the mass of gas in the bubble, temperature in the bubble, the gas constant, surface tension, and the vapor pressure, respectively. Bubble radii $r_b > r_B$ and pressures around a bubble $p_\infty < p_{\infty 0} - p_B$ create conditions favorable for the cavitation inception.

Noltingk and Neppiras (1950; Neppiras & Noltingk, 1951) noted that the initial radius of a bubble which is the cavity nuclei, r_{b0}, plays an important role, and is connected with the amplitude of applied pressure p_A, the base liquid pressure $p_{\infty 0}$, and the driving frequency f. Pressure $p_A - p_{\infty 0}$ has upper and lower limits beyond which no cavitation can commence. The lower limit which allows cavitation is approximately estimated as (Neppiras & Noltingk, 1951)

$$p_A - p_{\infty 0} > \frac{8}{9}\sqrt{\frac{3\gamma^3}{2r_{b0}^3\left(p_A + \frac{2\gamma}{r_{b0}}\right)}} \qquad \text{Eq. 2.3}$$

The frequency range which produces cavitation has the upper and lower limits for the given initial bubble radius. The lower limit is not so sharp and depends on the influx of gases and vapor in the bubble, and is hard to define precisely. The upper limit is quite sharp, and it is the resonant frequency. The relation between the bubble radius and its resonant frequency is (Noltingk & Neppiras, 1950; Neppiras & Noltingk, 1951; Young, 1989):

$$\rho_L r_{b0}^2 \left(2\pi f_r\right)^2 = 3\kappa\left(p_\infty + \frac{2\gamma}{r_{b0}}\right) - \frac{2\gamma}{r_{b0}} \qquad \text{Eq. 2.4}$$

This relation is shown in Figure 2.3; the analysis of Noltingk and Neppiras can be summarized as: cavitation does not occur if the combination of the radius and driving frequency is above the curve. As noted by Noltingk and Neppiras, oscillations of bubbles become more and more sinusoidal as the frequency increases above the resonant value. Hence the curve in Figure 2.3 represents the maximal driving frequency for the given radius, or vice versa, the maximal radius for the given frequency, which still produces cavitation. This separation between cavitating and non-cavitating regime should be taken as tentative, since even relatively small sinusoidal oscillations can be called stable cavitation (Leighton, 1994), although very weak.

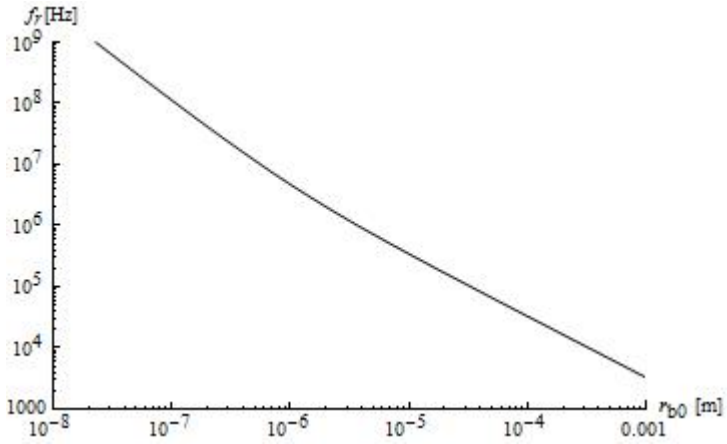

Figure 2.3. Resonant frequency as a function of the bubble radius, given for air bubbles in water.

There is also the lower threshold in r_{b0} below which a cavity cannot change its size significantly, so it undergoes oscillations without cavitation. The upper limit of the nucleus size is given in Eq. 2.4, while the lower limit can be inferred from Neppiras and Noltingk (1951):

$$r_{b0}^3 + 2\gamma r_{b0}^2 > \frac{8\gamma^3}{3\left(p_A - p_{\infty 0}\right)} \qquad \text{Eq. 2.5}$$

According to Noltingk and Neppiras, cavitation will be triggered on a non-wetted solid particle only if the initial particle radius is $r_{b0} > 2\gamma / \left(p_A - p_{\infty 0} \right)$.

It should be noted that Eq. 2.3 through Eq. 2.5 are only rough approximations due to the assumptions in the model. Since cavitation nuclei have randomly distributed values of r_{b0}, Noltingk and Neppiras conclude that theoretically calculated pressure fields have little practical significance in determining cavitation behavior; that should validate approximations given above. The Blake thresholds, Eq. 2.1 and Eq. 2.2, can also be treated as rough approximations.

It is accepted that when the pressure in liquid around a bubble is lower than the Blake threshold, p_B, the bubble will start to grow, denoting the inception of cavitation. From that point on, behavior of the cavity is described by bubble dynamics.

2.1.3. Bubble Dynamics

This section contains only a condensed overview of the most important results on bubble dynamics that will be used in this work.

Although not the first to address the problem of the collapse of a cavity, Rayleigh's paper (1917) is considered a cornerstone for later contributions. His model describes a cavity formed momentarily in an infinite amount of liquid with constant pressure p_∞. The pressure distribution, the velocity of the cavity boundary and the time of collapse are given for the cavity modeled as an empty volume (annihilated liquid with $p_b = 0$). A brief analysis of a cavity filled with a non-condensable gas at some pressure p_g with no vapor in it (so $p_b = p_g$), but only the velocity of the boundary was solved. The boundary conditions are summarized in Figure 2.4. Although Rayleigh analyzed cavity in its true sense, it will be regarded as a special case of a bubble, namely an empty bubble. Hence the physical properties that characterize such a cavity will have subscript "b".

The total work done in the system is consisted of the work done by pressure p_∞ during the volume change and of the work of compression of the gas inside the bubble.

Equaling this total work with the kinetic energy of the motion, Rayleigh obtained the velocity of the boundary as

$$u_b^2 = \frac{2p_\infty}{3\rho_L}\left(\frac{r_{b0}^3}{r^3}-1\right) - \frac{2p_b}{\rho_L}\frac{r_{b0}^3}{r^3}\ln\frac{r_{b0}}{r} \qquad \text{Eq. 2.6}$$

The second term on the right-hand side will vanish for an empty cavity ($p_b = 0$), so

$$u_b^2 = \frac{2p_\infty}{3\rho_L}\left(\frac{r_{b0}^3}{r^3}-1\right) \qquad \text{Eq. 2.7}$$

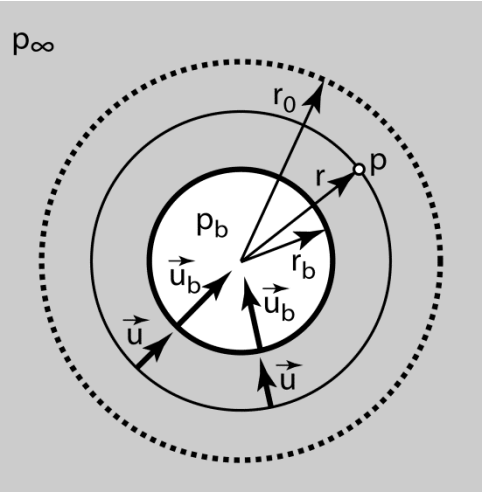

Figure 2.4. Boundary conditions set by Rayleigh (1917). The system is isothermal and consists of a cavity surrounded by an infinite amount of liquid. The collapsing cavity with the momentary radius r_b had initial radius r_{b0}. The pressure in the bulk of liquid is p_∞ and in the cavity $p_b = const$. At the boundary ($r = r_b$), the pressure is p_b. The liquid element at the distance r from the center of the cavity has pressure p and velocity u.

It is obvious from Eq. 2.7 that the velocity of the wall of an empty cavity increases indefinitely as the bubble radius r approaches zero. This is illustrated in Figure 2.5 with curve $p_b = 0$. To prevent that, Rayleigh introduces a gas into the cavity as a damper. From Eq. 2.6 he concludes that, for any positive pressure p_b the cavity radius r_b never diminishes since the velocity of the cavity wall reaches zero before complete

collapse. This is shown in Figure 2.5 for magnitudes of p_b above and below the surrounding pressure of the liquid p_∞.

Using Eq. 2.7, the collapse time and pressure distribution for an empty cavity is

$$\tau = \int_0^{r_{b0}} \frac{dr_b}{r_b} = 0.91468\, r_{b0}\sqrt{\frac{\rho_L}{p_\infty}} \qquad \text{Eq. 2.8}$$

For example, the collapse time of an empty cavity with $r_0 \approx 10$ μm in water would be of the order of 10^{-7} to 10^{-6} s. According to Franc and Michel (2004) this is a very good estimation for wide range of bubble diameters, from the range of micrometer to one meter.

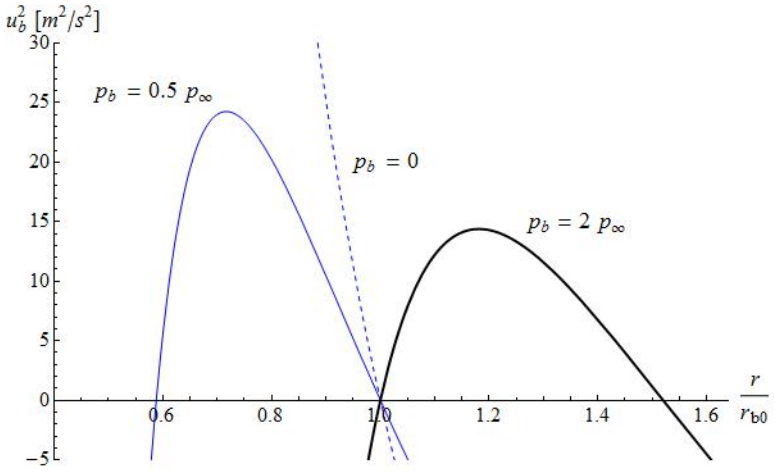

Figure 2.5. Plot of Eq. 2.6 for $p_b = 0.5 p_\infty$ and $p_b = 2 p_\infty$, and a special case of empty cavity with $p_b = 0$ (Eq. 2.7). Usual values for water density (ρ_L = 1000 kg/m^3) and atmospheric pressure (p_∞ =101325 Pa) are taken, and hydrostatic pressure is neglected.

Rayleigh also calculates the pressure distribution around the empty cavity. He starts with "the general equation of pressure", which is the Euler's equation of motion with neglected body forces (or Bernoulli's equation):

$$\frac{1}{\rho_L}\frac{dp}{dr} = -\frac{Du}{Dt} = -\frac{\partial u}{\partial t} - u\frac{\partial u}{\partial r} \qquad \text{Eq. 2.9}$$

The pressure distribution in the liquid around the cavity is:

$$\frac{p}{p_\infty} = \frac{r_b}{3r}\left(\frac{r_{b0}^3}{r_b^3} - 4\right) - \frac{r_b^4}{3r^4}\left(\frac{r_{b0}^3}{r_b^3} - 1\right) + 1 \qquad \text{Eq. 2.10}$$

This function is plotted in Figure 2.6. As can be seen, the pressure near the cavity boundary rises as the cavity decreases in size. Rayleigh calculates that the pressure in the liquid peaks to 1260 p_∞ when $r_b = r_{b0} / 20$.

It would be interesting to estimate the radial coordinate where the pressure maximum occurs. That can be easily found from Eq. 2.10:

$$r_{p\max} = r_b \sqrt[3]{4\frac{r_{b0}^3 - r_b^3}{r_{b0}^3 - 4r_b^3}} \qquad \text{Eq. 2.11}$$

If this is the maximum the second derivative has to be negative, so

$$r_{p\max} < r_b \sqrt[3]{10\frac{r_{b0}^3 - r_b^3}{r_{b0}^3 - 4r_b^3}} \qquad \text{Eq. 2.12}$$

Since Eq. 2.11 automatically satisfies inequality in Eq. 2.12, this proves that $r_{p\max}$ calculated in Eq. 2.11 represents indeed the location where the maximum pressure occurs in the liquid. The special case is when $r_b = r_{b0}$, which is the location of the global minimum for the function p / p_∞, hence there is no maximum in that case. It can be noted (Figure 2.5) that according to this model, a single cavity upsets the pressure in the whole liquid and its initial value $p_{\infty 0}$ is approached only asymptotically far from the cavity. This is due to the assumption of incompressibility.

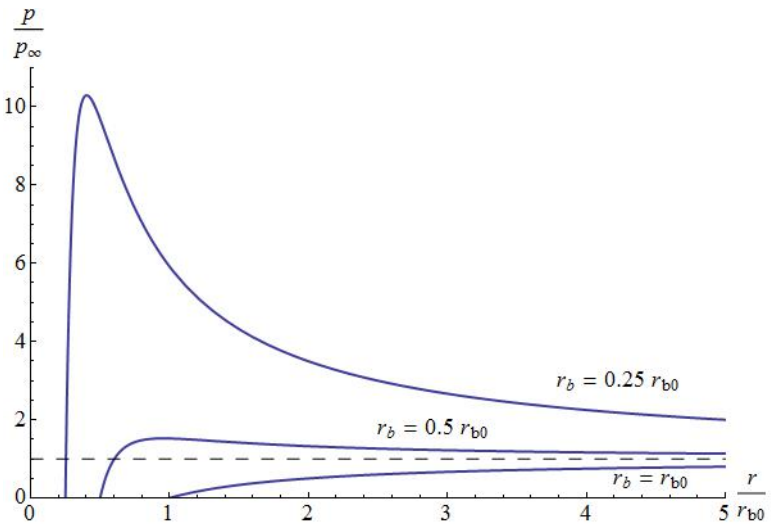

Figure 2.6. A pressure distribution in the liquid as the empty cavity collapses. Three instances are given: at the onset of collapse when $r_b = r_{b0}$, when the cavity radius is half the initial value ($r_b = r_{b0}/2$), and when $r_b = r_{b0}/4$. They are obtained from Eq. 2.10. The pressure at the cavity boundary is zero at all times, which is assumed boundary condition. Initial pressure in the liquid is dashed horizontal line at $p/p_\infty = 1$.

The next significant contribution was given by Plesset (1949), who extended Rayleigh's model introducing the vapor pressure in the cavity, variable pressure of the fluid, and adding surface tension. Plesset actually applies classic potential flow theory to this problem. Cavity is assumed as a point sink or source, depending on whether it grows or shrinks. Due to spherical symmetry and incompressibility, there is no vorticity.

To describe the motion of the cavity, Plesset most likely uses the same form as Rayleigh's Eq. 2.9, which applies for the stagnant liquid, and extends it adding a term with "static pressure at a distance from the bubble", $p_\infty(t)$. The pressure $p_\infty(t)$ can serve as a variable driving pressure of the acoustic field. In a straightforward fashion, he obtained:

$$\frac{p(r_C) - p_\infty(t)}{\rho_L} = \frac{3}{2}\left(\frac{\partial r_C}{\partial t}\right)^2 + r_C\frac{\partial^2 r_C}{\partial t^2} = \frac{3}{2}\dot{r}_C^2 + r_C\ddot{r}_C \qquad \text{Eq. 2.13}$$

Plesset claim that the Rayleigh's model is a special case of this equation when $p_\infty(t) - p(r_b) = const$, meaning that p_∞ does not vary with time. In this case the Rayleigh's model should look like:

$$\frac{p(r_b) - p_\infty}{\rho_L} = \frac{3}{2}\dot{r}_b^2 + r_b\ddot{r}_b \qquad \text{Eq. 2.14}$$

This can be confirmed by using $u / u_b = \left(r_b / r\right)^2$ in Eq. 2.10 and integrating with appropriate limits (pressure from $p(r_b)$ to p_∞ and coordinate from r_b to ∞). It is interesting to note that Plesset, in a review article 28 years later (Plesset & Prosperetti, 1977), states that Rayleigh proved Eq. 2.14. This is probably an act of homage to Rayleigh, since Rayleigh actually never integrated Eq. 2.10 to obtain Eq. 2.14.

Plesset also includes surface tension of the form of Eq. 2.13, so the final model suggested by Plesset (1949) is

$$p_V - p_\infty(t) - \frac{2\gamma}{r_b} = \rho_L\left(\frac{3}{2}\dot{r}_b^2 + r_b\ddot{r}_b\right) \qquad \text{Eq. 2.15}$$

This is the simplest form of the famous Rayleigh-Plesset equation, although many authors give the same name to equations augmented with terms which represent adiabatic gas and viscosity.

While Rayleigh and Plesset analyzed dynamics of a cavity in general, Noltingk and Neppiras (1950; Neppiras & Noltingk, 1951) presented a theoretical analysis pertinent to ultrasonically induced cavitation, giving theoretical predictions for important features which describe cavitation, like velocities, pressures, and radii at different phases of the cavity lifecycle. Assumed were incompressible liquid and the gas content constant throughout the cavity. They are more specific than Plesset in defining the variable pressure filed. They assume that applied ultrasonic pressure wave in the liquid is periodic and have sinusoidal character: $p_\infty(t) = \left(p_{\infty 0} - p_A \sin \omega t\right)$, where $p_{\infty 0}$ is static pressure (usually taken as atmospheric pressure), p_A the pressure amplitude of applied ultrasonic wave, time is denoted t, and $f = \omega / \left(2\pi\right)$ is the frequency.

Noltingk and Neppiras (1950) follow Rayleigh's procedure in derivations. By equaling the total work done inside the cavity with the kinetic energy of motion of the boundary they obtained the equation of motion:

$$p_A \sin \omega t - p_{\infty 0} + p_V + \left(p_{\infty 0} + \frac{2\gamma}{r_{b0}} - p_V \right) \left(\frac{r_{b0}}{r_b} \right)^{3\kappa} = \frac{2\gamma}{r_b} + \frac{3}{2} \rho_L \dot{r}_b^2 + \rho_L r_b \ddot{r}_b \qquad \text{Eq. 2.16}$$

In their original work, Noltingk and Neppiras neglected the vapor pressure p_V. It is obvious this equation has the same form as Plesset's Eq. 2.15. The only difference is in how pressure terms are defined. Eq. 2.16 holds for a cavity that forms on existing gas nuclei with the radius r_0. For a cavity formed at a solid particle not wetted by the liquid, they assume there is no gas inside the cavity, so the previous equation is abbreviated by the work done by the gas inside the cavity:

$$p_A \sin \omega t - p_{\infty 0} + p_V = \frac{2\gamma}{r_b} + \frac{3}{2} \rho_L \dot{r}_b^2 + \rho_L r_b \ddot{r}_b \qquad \text{Eq. 2.17}$$

Equation of motion Eq. 2.16 can be used to calculate maximal cavity radius and the corresponding time when that cavity size occurs.

Noltingk and Neppiras found that the maximal radius a bubble can achieve is inversely proportional to the frequency of oscillating pressure field, ω (or f). So they conclude that cavitation effects falls off with increased frequency, since increased ω decreases maximal radius a bubble can achieve. In other words, increased frequency should decrease the range of radii which can produce a cavity. Limiting frequencies above which there is no cavitation are estimated to be in the range of MHz.

The theory described so far, sublimed in Eq. 2.16, predicts that transient cavitation can commence only in a narrow window of ultrasonic parameters. This is illustrated in Figure 2.7 for an air bubble-water system with the initial bubble radius of 1 μm, driven by variable pressure with the amplitude $p_A = 2\,p_{\infty 0}$. According to the numerical example given at the end of Section 2.1.2, this condition should produce cavitation.

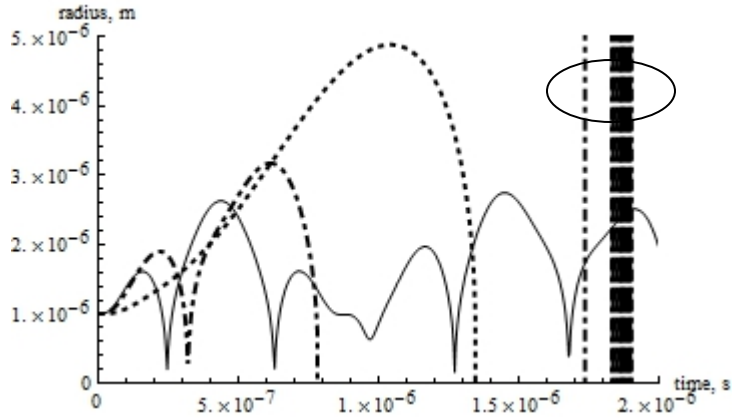

Figure 2.7. Temporal change of the radius of an air bubble in water under oscillatory pressure field with the amplitude $p_A = 2\,p_{\infty 0}$ and frequency 0.5 MHz (thick dotted line) 2.7 MHz (thick dash-dotted line) and 4 MHz (thin solid line). Assumed constants are r_{b0} =1 μm, $p_{\infty 0}$ =101325 Pa, p_V = 2300 Pa, ρ_L = 1000 kg/m^3, γ = 0.072 N/m, κ = 1 (isothermal process). Circled are examples of numerical instability when the solution for the bubble radius emerges back from negative values, which does not have physical sense, and takes high positive values and/or becomes to oscillate between positive and nagetive values.

The lowest frequency in this example for transient cavitation, i.e. when a bubble becomes a collapsing cavity, was found to be around 0.5 MHz, and the highest somewhat below 3 MHz. As shown in Figure 2.7, after one rebound at 2.7 MHz the cavity "disappears" on its second collapse (Eq. 2.4 estimates the upper limit of 1.32 MHz).[8] With the slight increase in the frequency, rebounds continue without the complete collapse, which is usually termed as stable cavitation. As shown in Figure 2.7, a 1 μm bubble undergoes complex oscillations when driven by 4 MHz oscillating pressure. As the driving frequency gets higher above the transient cavitation regime, oscillations of the bubble become smaller and steadier. This is shown in Figure 2.8, where bubble oscillations are nonlinear but with relatively small amplitudes, around 8% of the initial radius. However, this can still regarded as stable cavitation.

---

[8] When said that the bubble disappeares, its radius actually takes negative values in Figure 2.7. Later, the radius springs back in the range of positive values (circled in Figure 2.7).

At frequencies below the range which produces cavitation, bubbles are expected to grow according to Eq. 2.16. The bubble growth is slower as frequencies get lower. Exposed to 20 kHz frequency, a 1 μm bubble will grow (Figure 2.8) until it is carried away from the liquid by buoyancy. Hence, degassing by the application of ultrasonic field might not be a result of cavitation, but the bubble growth. However, this theory is not complete enough to render these predictions valid.

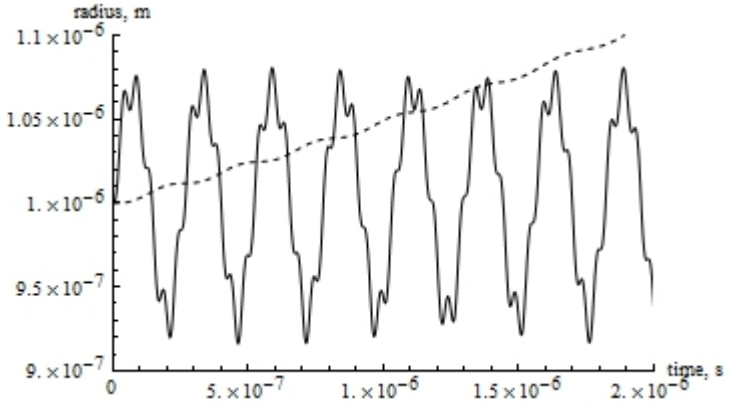

Figure 2.8. Temporal change of the radius of an air bubble in water under oscillatory pressure field with the amplitude $p_A = 2\,p_{\infty 0}$ and frequencies 20 kHz (dotted line) and 20 MHz (solid line). Used values are r_{b0} =1 μm, $p_{\infty 0}$ =101325 Pa, p_V = 2300 Pa, ρ_L = 1000 kg/m^3, γ = 0.072 N/m, κ = 1.

Poritsky[9] contributed further to the theory set by Rayleigh and then Plesset by adding viscosity in the analysis. Eq. 2.16 in the final form is (Brennen, 1995):

[9] Poritsky, H. (1952). The collapse or growth of a spherical bubble or cavity in a viscous fluid. In E. Stemberg (Ed.), *Proceedings of the First U.S. National Conference in Applied Mathematics, June 11-16, 1951, Illinois Institute of Technology, Chicago, IL* (pp. 813-821). New York: ASME. This work is also unavailable to the author of this text. As Blake's work, this one is also widely cited.

$$p_A \sin \omega t - p_{\infty 0} + p_V + \left(p_{\infty 0} + \frac{2\gamma}{r_{b0}} - p_V \right) \left(\frac{r_{b0}}{r_b} \right)^3 = \frac{3}{2} \rho_L \dot{r}_b^2 + \rho_L r_b \ddot{r}_b + 4\mu \frac{\dot{r}_b}{r_b} + \frac{2\gamma}{r_b} \qquad \text{Eq. 2.18}$$

where μ is dynamic viscosity. In the literature, this is called RPNNP equation, an acronym of Rayleigh-Plesset-Noltingk-Neppiras-Poritsky, or more frequently just Rayleigh-Plesset equation.

It is obvious that addition of viscosity should damp oscillations to some extent, and that can be seen comparing Figure 2.8 and Figure 2.9. The growth rate of the bubble driven by driving pressure varying with 20 kHz is higher after initially slower start.

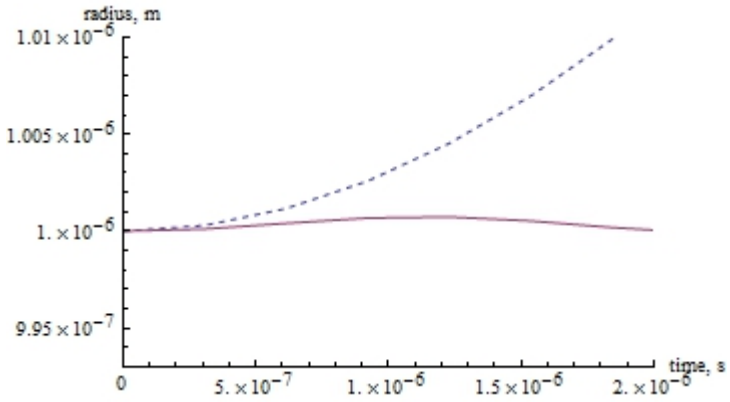

Figure 2.9. Temporal change of the radius of an air bubble in water under oscillatory pressure field with the amplitude $p_A = 2p_{\infty 0}$ and frequencies 20 kHz (dotted line) and 20 MHz (solid line). Used values are r_{b0}=1 μm, $p_{\infty 0}$=101325 Pa, p_V = 2300 Pa, ρ_L = 1000 kg/m^3, γ = 0.072 N/m, μ = 10^{-3} Ns/m^2, κ = 1.

Results shown in Figure 2.7 through Figure 2.9 are made under the isothermal assumption. With adiabatic assumption (κ = 1.4) and viscosity, it is harder to find cavitating regime. Even more, a bubble shows smooth oscillations, Figure 2.10, while in isothermal conditions and with neglected viscosity the bubble cavitated or underwent nonlinear oscillations (Figure 2.7). It is also obvious that the negative amplitude of oscillations is smaller due to higher compression effects under adiabatic conditions.

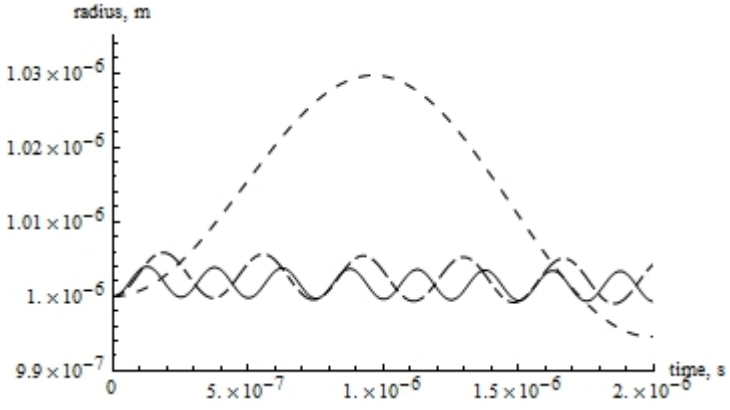

Figure 2.10. Bubble motion under the same conditions as in Figure 2.7, except $\kappa = 1.4$ in this case, meaning adiabatic process, and $\mu = 10^{-3}$ Ns/m^2 instead of no viscosity. The bubble is driven with frequencies 0.5 MHz (thick dotted line) 2.7 MHz (thick dash-dotted line) and 4 MHz (thin solid line).

Oscillations shown so far can be complex but they are not damped, or at least amplitudes decrease very slowly. This is largely due to the assumption of incompressibility of the liquid. Trilling (1952) derived equations for the velocity and pressure field during the collapse and rebound of a spherical gas bubble, with the assumption that disturbances are transmitted through the liquid with the speed of sound in the infinity, c_∞, limiting validity of the model to velocities smaller than the speed of sound, $u < c_\infty$. Gilmore (1952) performed similar derivation, but using the Kirkwood-Bethe approximation[10] that changes in the fluid[11] propagate with a velocity which is the sum of the fluid velocity and the speed of sound, $u + c_\infty$. The Kirkwood-Bethe hypothesis broadens significantly the range of velocities for which the model is still valid. In a

---

[10] Kirkwood, J. G., & Bethe, H. A. (1942). *The Pressure Wave Produced by an Underwater Explosion.* Report No. 588. Office of Scientific Research and Development. A comprehensive summary of this work was given in the book by Cole (1948).

[11] $r\phi$ and kinematic enthalpy $r\left(h + u^2/2\right)$ in this particular case.

straightforwardly presented derivation procedure, Gilmore (1952) obtained the equation of the bubble wall motion:

$$\left(1-\frac{\dot{r}_b}{c_b}\right)r_b\ddot{r}_b+\frac{3}{2}\left(1-\frac{\dot{r}_b}{3c_b}\right)\dot{r}_b^2=\left(1-\frac{\dot{r}_b}{c_b}\right)\frac{r_b\dot{h}_b}{c_b}+\left(1+\frac{\dot{r}_b}{c_b}\right)h_b \qquad \text{Eq. 2.19}$$

where c_b is the speed of sound in the liquid at the bubble interface and h_b is the enthalpy difference between at the bubble boundary and in the bulk. For adiabatic compression in general, it is $h(p)=\int_{p_\infty}^{p} dp/\rho$. More details on this assumption can be found in the book by Cole (1948).

Gilmore derived Eq. 2.19 assuming constant bulk pressure, p_∞. It is interesting that viscosity and compressibility are included in the model only through the boundary conditions. All these effects are grouped in h_b. Akulichev (1971) gave an elegant derivation of Eq. 2.19, crediting Kirkwood and Bethe for this model. He defined h_b differently to accommodate variable acoustic pressure at infinity, p_∞. Using the Tait equation of state for the liquid

$$\frac{p+B}{p_\infty+B}=\left(\frac{\rho_L}{\rho_{L\infty}}\right)^n \qquad \text{Eq. 2.20}$$

he obtained

$$h_b=\frac{n}{n-1}\frac{\left(p_\infty+B\right)^{1/n}}{\rho_L}\left\{\left[\left(p_\infty+\frac{2\gamma}{r_{b0}}\right)\left(\frac{r_{b0}}{r_b}\right)^{3\kappa}-\frac{2\gamma}{r_b}+B\right]^{\frac{n-1}{n}}-\left[p_{\infty 0}-p_A\sin\left(2\pi ft\right)+B\right]^{\frac{n-1}{n}}\right\} \qquad \text{Eq. 2.21}$$

where B and n in Eq. 2.20 are constants. For water $B=3000\,atm\approx 3\cdot 10^8\,Pa$ and $n=7$. p and ρ_L are local pressure and density in the liquid, while $p_{\infty 0}=p_{atm}$ and $\rho_{L\infty}$ are the values in the undisturbed liquid, and assumed driving pressure at infinity $p_\infty=p_{\infty 0}-p_A\sin\left(2\pi ft\right)$. Eq. 2.21 lacks viscosity term. The speed of sound at the bubble boundary is determined as (Akulichev, 1971):

$$c_b = \sqrt{c_\infty^2 + (n-1)h_b} \qquad \text{Eq. 2.22}$$

The motion of the bubble is found by solving Eq. 2.19 together with Eq. 2.21 and Eq. 2.22. As an illustration, Figure 2.11 shows the motion of air bubbles with two initial radii, 1 μm and 10 μm, in water driven by the pressure amplitude $p_A = 1.6\,p_\infty$ and frequency 20 kHz. A bubble with 1 μm initial radius expands 40 times before it collapses violently, while a 10 μm bubble expands its size around 10 times. It is characteristic that bubbles rebound after the first collapse and undergo damped oscillations around their initial radius. These rebounds are stronger and last longer as the bubble size increases. As shown in Figure 2.11, rebounds of a 10 μm bubble last up to the next cycle. All these differences are due to the different amount of gas which serves as a cushion on the first collapse and as an oscillating mass during rebounds.

There are other models which describe motion of bubbles. One of the most successful is the model of Keller and coworkers derived initially for underwater explosions (Keller & Kolodner, 1956), expanded later for planar, cylindrical and spherical bubbles (Epstein & Keller, 1972), and for spherical bubbles in an acoustic field (Keller & Miksis, 1980). In order to stress resemblance with Eq. 2.19, we use the form of Keller's equation given by Prosperetti and Lezzi (1986; Brennen, 1995; Brenner, Hilgenfeldt, & Lohse, 2002) augmented with the two last terms on the right hand side (Brenner, Hilgenfeldt, & Lohse, 2002):

$$\left(1-\frac{\dot r_b}{c_\infty}\right) r_b \ddot r_b + \frac{3}{2}\left(1-\frac{\dot r_b}{3c_\infty}\right)\dot r_b^2 = \left(1+\frac{\dot r_b}{c_\infty}\right)\frac{1}{\rho_L}\left[p_b - p_\infty - p\left(t+\frac{r_b}{c_\infty}\right)\right] + \frac{r_b}{\rho_L c_\infty}\dot p_b - \frac{4\mu}{\rho_L}\frac{\dot r_b}{r_b} - \frac{2\gamma}{\rho_L r_b} \qquad \text{Eq. 2.23}$$

Here, $p\left(t + r_b / c_\infty\right)$ is the variable part of the pressure at the cavity center as if there was no cavity; in that case it would have been just $p(t)$. Keller and coworkers represented the velocity potential of irrotational flow with the wave equation, not with Laplace equation commonly used for incompressible liquids, and combined it with the momentum equation of incompressible liquid.

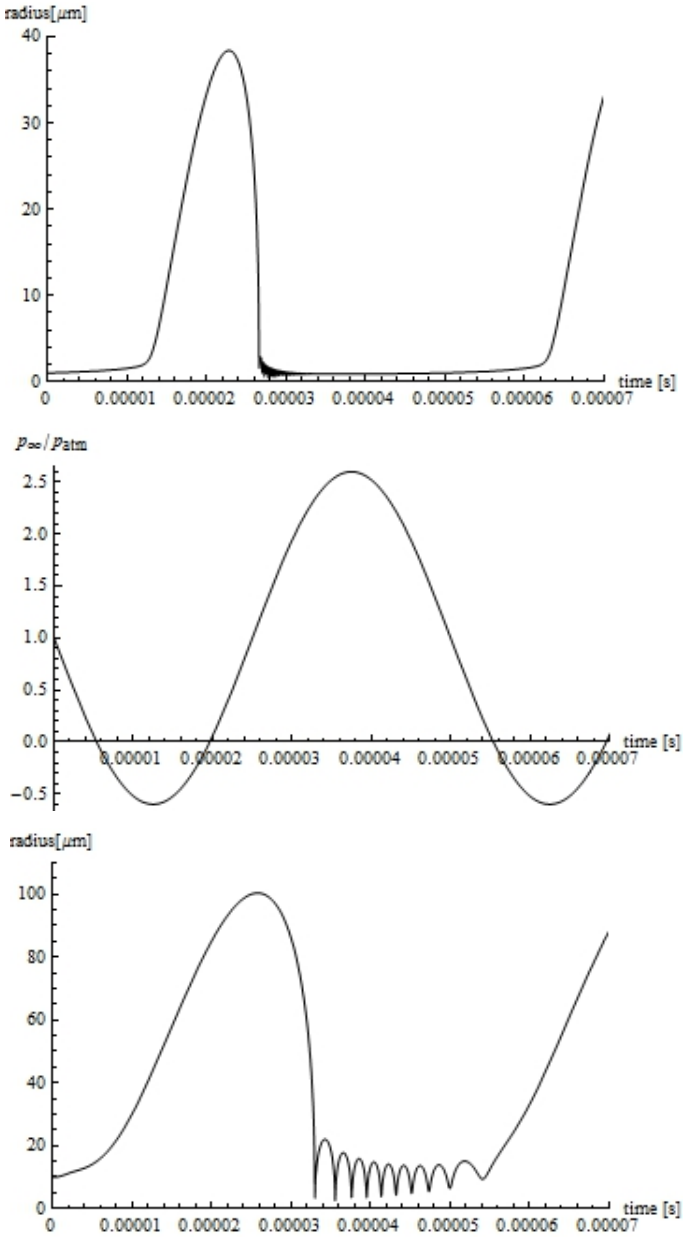

Figure 2.11. Solution of the Gilmore model, Eq. 2.19, Eq. 2.21, and Eq. 2.22, for initial bubble radius a) 1 μm, and c) 10 μm. The middle graph (b) shows variation in the surrounding pressure, p_∞, consisting of the atmospheric pressure p_{atm} and superimposed sinusoidal oscillating pressure with the amplitude $p_A = 1.6\,p_\infty$ and frequency $f = 20\,kHz$.

Maybe the most complete model of the bubble collapse was given by Fujikawa and Akamatsu (1980). Beside surface tension, viscosity, and compressibility, they also

included evaporation and condensation of the liquid phase, and thermal conduction between the bubble and liquid. However, their results are fairly similar to those obtained by simpler models, and their model did not include driving pressure. Also, models given by Keller and coworkers agree quite well with experimental measurements. Using photometry, Sirotyuk (1971) obtained a good fit in the region of the initial bubble expansion and collapse (large increase in radius in Figure 2.11). However, measurement resolution was not good enough to capture bubble rebounds. Using the light scattering technique in a single bubble sonoluminescence experiment, Matula (1999) obtained a very good fit with the Keller-Miksis model for isothermal, both for the initial expansion and collapse, and subsequent rebounds. It should be noted that the measurement technique required the data to be calibrated with the theoretical curve for the maximal and minimal bubble radius.

Some estimations of the velocity and pressure field around collapsing bubble have been given in Eq. 2.6 through Eq. 2.11. However, it would be interesting to obtain estimations based on more complex models. Hickling and Plesset (1964), and Ivany and Hammit (1965) used the model of Gilmore (1952) to obtain the velocity and pressure filed in the liquid phase upon the bubble rebound. According to these results, pressures in order of 10^4 to 10^5 atmospheres appear, but only within the volume of the initial bubble size during the bubble rebound. In both of these works, calculations were performed for a bubble from its maximal radius, with predicted initial pressure in the bubble at that moment. The collapse was assumed to happen at the constant surround pressure; no periodic pressure was taken into account.

Calculation of the pressure field is deferred to the results section, where the nucleation rate caused by increased pressure is estimated. In that procedure, the Gilmore model will be used, despite some arguments that Keller-Miksis model is more accurate (Prosperetti & Lezzi, 1986; Lezzi & Prosperetti, 1987). On the other hand, a “remarkable accuracy” of the Gilmore model has also been mentioned (Hickling & Plesset, Collapse and Rebound of a Spherical Bubble in Water, 1964; Prosperetti & Lezzi, 1986). As discussed by Prosperetti and Lezzi (1986), the use of the enthalpy seems to be more accurate in determining the pressure wave than the use of pressure which depends on

velocity. In this work, estimated pressure filed is of primary interest. As mentioned, the enthalpy h_b in the Gilmore model can be defined differently than in Eq. 2.21 to include more effects into the model. For example, h_b could be calculated similarly to Lezzi and Prosperetti (1987), or Gilmore (1952), pages 20 and 21.

There is a number of published works which discusses accuracy of different models of the bubble collapse, and propose certain modifications to them. In this work there is no much use of seeking high accuracy for two obvious reasons. Firstly, the size distribution of nuclei is unknown. Besides that, the collapse of a bubble is not an isolated event, but a chain reaction; the collapse of one bubble releases pressure/shock waves which in turn trigger collapses of surrounding bubbles.

2.2. Propagation of Ultrasound in Liquids

Propagation of sound waves in liquids is a very broad and complex field. Of interest in this research are mainly acoustic intensity, losses of acoustic energy in the liquid, acoustic pressure, and acoustic streaming. Although the last two mentioned phenomena are second-order effects, they are briefly mentioned here because dendrite dispersion has been mentioned in the literature as one of mechanisms for grain refinement.

In this chapter is given a very rudimentary literature overview, mostly because the majority of the theory of sound beams is developed with the assumption that the sound wavelength is much shorter than the sound beam diameter ($\lambda << r_B$). Unfortunately, the situation in this work is opposite – the sonotrode radius is only a fraction of the wavelength of applied ultrasound, so the applicability of the theory is at least questionable in this case. However, attention will be paid to those features which could be used for qualitative estimations in case of relatively long wavelengths. For example, a very shallow cavitation zone is obtained with the experimental setup described in Section 3, and that is qualitatively predicted with equations given in the section that follows (Section 2.2.1).

Advanced topics, like propagation and dispersion of sound in a liquid containing bubbles and solid particles, or other topics would be beyond the scope of this work.

2.2.1. Acoustic Intensity and Energy Losses

Acoustic intensity is a vector field defined as

$$\vec{I}\left(\vec{r},t\right)=p_a\left(\vec{r},t\right)\vec{v}\left(\vec{r},t\right)=\left[\,p\left(\vec{r},t\right)-p_0\,\right]\vec{v}\left(\vec{r},t\right) \qquad \text{Eq. 2.24}$$

Here, $p_a\left(\vec{r},t\right)$, $p\left(\vec{r},t\right)$, and $\vec{v}\left(\vec{r},t\right)$ are, respectively, acoustic pressure, total pressure, and velocity which depend on the coordinate, $\vec{r}$, and time, t; p_0 is equilibrium pressure in the liquid without the sound field. Since acoustic intensity is defined as the acoustic energy flux, the temporal average of heat generated in the unit volume can be defined as (Nyborg, 1981):

$$\left\langle q_V\right\rangle=-\vec{\nabla}\cdot\left\langle\vec{I}\right\rangle \qquad \text{Eq. 2.25}$$

where $\left\langle\cdot\right\rangle$ denotes the time average. The importance of acoustic intensity is obvious, since pressure, velocity, temperature, and some equation of state are commonly used to completely define the liquid phase.

Due to the experimental setup used in this work (cf. Section 3.1), it will suffice to know acoustic intensity produced by a piston. Readily available in the literature is acoustic intensity along the axis of a plane piston (Kinsler & Frey, 1950; Beyer, 1974):

$$\begin{aligned} I_p &= \frac{\left\langle\left[\mathrm{Re}\left(p_a\right)\right]^2\right\rangle}{\rho_0 c}=2\rho_0 c\dot{\xi}_0^2\sin^2\left[\frac{\pi}{\lambda}\left(\sqrt{z^2+r_B^2}-z\right)\right] \\ &= I_{\max}\sin^2\left[\frac{\pi}{\lambda}\left(\sqrt{z^2+r_B^2}-z\right)\right] \end{aligned} \qquad \text{Eq. 2.26}$$

where $\mathrm{Re}\left(p_a\right)$ is the real part of acoustic pressure, ρ_0 and c are, respectively, the density and the speed of sound in the liquid phase, ξ_0 is the displacement of the piston, λ the wavelength, r_B radius of the piston (beam), and z is the axial distance from the piston surface.

Eq. 2.26 is obtained when the velocity in Eq. 2.24 is substituted with the relation $p / v = \rho_0 c$ (Beissner, 1982). For that reason, following Beissner (1982), it is given a subscript "p". Similarly, another alternate expression for acoustic intensity can be expressed with the velocity as the only variable, and one gets a different quantity. Acoustic intensity with both the pressure and velocity as variables is (Beissner, 1982):

$$I = \frac{I_{\max}}{2}\left(1+\frac{z}{\sqrt{z^2+r_B^2}}\right)\sin^2\left[\frac{\pi}{\lambda}\left(\sqrt{z^2+r_B^2}-z\right)\right] \qquad \text{Eq. 2.27}$$

There are expressions for a simply supported cylinder or a cylinder clamped at its edges (Dekker, Piziali, & Dong, 1974; Greenspan, 1979), and they give higher intensity along the axis. In this work we will use Eq. 2.26 and Eq. 2.27, derived for a planar piston, with constant velocity across the surface, oscillating in an infinite rigid baffle. These equations are plotted in Figure 2.12 when the wavelength is one fourth of the piston radius. It can be seen that both definitions approach the same values in the far field. Characteristic for both equations is that the number of peaks equals r_p / λ ratio and the last peak appears at the distance $z = r_P^2 / \lambda$, which is the length of the near field.

Considering Eq. 2.24 and Eq. 2.25, acoustic intensity can be determined by measuring pressure, velocity, or temperature in the liquid. Pressure measurement is the most common and the most direct method.

In experiments in this work the sound beam radius is only a fraction of the ultrasound wavelength, but it seems that Eq. 2.26 (hence Eq. 2.27) is used for the on-axis intensity for wide range of frequencies, so acoustic intensity will be used in our case qualitative estimation of the near field length, which is a zone where cavitation primarily occurs. An approximation of acoustic pressure in the far field and for low frequencies ($kr_B << 1$) is (Beyer, 1974):

$$p_a = i\,2\pi f\, r_B^2 \rho_0 \dot{\xi}_0^2 \frac{\exp\left[i\left(2\pi f\, t - \vec{k}\cdot\vec{r}\right)\right]}{2r}\frac{2J_1\left(kr_B \sin\Theta\right)}{kr_B \sin\Theta} \qquad \text{Eq. 2.28}$$

where $k = \omega / c = 2\pi f / c$ is the wave number, $\vec{k}$ being parallel to $\vec{v}$, f oscillation frequency, $\vec{r}$ is the position of a point relative to the center of the piston, Θ is the angle

the point makes with the beam axis, and J_1 is the first-order Bessel function of the first kind.

The total acoustic energy density is defined as:

$$E = I / c \qquad \text{Eq. 2.29}$$

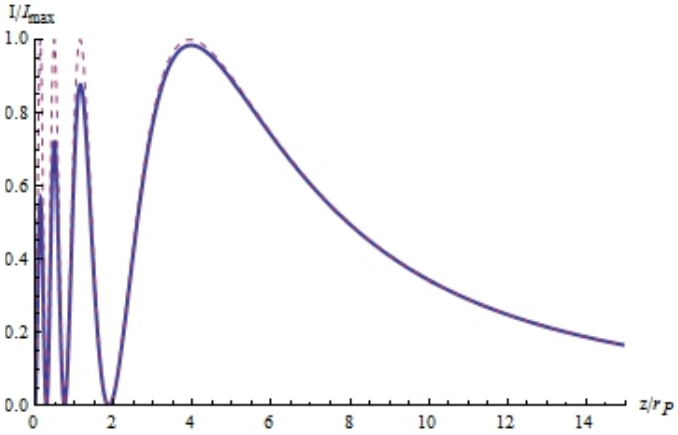

Figure 2.12. Variation of intensity along the axis of a planar piston oscillating in an infinite rigid baffle, defined with Eq. 2.26 (dashed line) and Eq. 2.27 (solid line), with $r_P = 4\lambda$. The intensity is normalized with $I_{\max}$, and the axial distance is normalized with the piston radius, r_P .

2.2.2. Acoustic Streaming

Acoustic streaming, a fluid flow caused by propagation of sound, arises from attenuation of sound waves (Nyborg, 1981; Westervelt, 1953; Lighthill, 1978).

Acoustic streaming is described as any problem in fluid dynamics by solving a set of equations which describe the conditions for continuity, balance of momentum, and some equation of state. In these equations are inserted pressure, velocity, density, and the speed of sound, expressed as perturbations up to the second-order:

$$p = p_0 + p_1 + p_2 + ...$$

$$u = u_0 + u_1 + u_2 + ...$$

$$\rho = \rho_0 + \rho_1 + \rho_2 + ...$$

$$c = c_0 + c_1 + c_2 + ...$$

Other properties can be expressed is the same way.

Eckart (1948) obtained a solution for the flow in the direction of the sound beam with the radius r_B in a tube with the radius r_W, which was presented in the integrated from by Beyer (1974):

$$u_2 = G\left[\frac{1}{2}\left(1-\frac{r^2}{r_B^2}\right)-\left(1-\frac{r_B^2}{2r_W^2}\right)\left(1-\frac{r^2}{r_W^2}\right)-\ln\frac{r_B}{r_W}\right],\ 0<r<r_B \qquad \text{Eq. 2.30a}$$

for the velocity distribution within the sound beam and

$$u_2 = -G\left[\left(1-\frac{r_B^2}{2r_W^2}\right)\left(1-\frac{r^2}{r_W^2}\right)+\ln\frac{r_B}{r_W}\right],\ r_B<r<r_W \qquad \text{Eq. 2.30b}$$

for the distribution between the beam and the container wall, where

$$G = \frac{(4/3)\mu+\mu'}{c_0}\left(\frac{\pi f u_0 r_B}{c_0}\right)^2 \qquad \text{Eq. 2.30c}$$

When the sound beam fills the tube ($r_B = r_W$), $u_2 = 0$.

A useful to correlation the velocity on the beam axis and acoustic intensity is (Liewbermann, 1949):

$$u_{2a} = I\frac{4\pi^2 f^2 r_B^2}{\rho_0 c_0^4}\left[\frac{1}{2}\left(\frac{r_B^2}{r_W^2}-1\right)-\ln\frac{r_B}{r_W}\right]\left(2+\frac{\mu'}{\mu}\right) \qquad \text{Eq. 2.31}$$

2.2.3. Radiation Pressure

Radiation pressure is also a second-order effect in acoustics, so it will be only briefly mentioned here. There has been some disagreement in the literature about radiation pressure (Beyer, 1978; Chu & Apfel, 1982; 1984; Nyborg & Rooney, 1984; Beissner, 1986; Lee & Wang, 1993), because it is usually a subtle phenomenon so it depends a lot on how it is defined.

There are two different definitions of radiation pressure. Radiation pressure acting on a target in a confined medium is defined as Rayleigh radiation pressure, and as Langevin radiation pressure if the medium is not laterally confined (Chu & Apfel, 1982). In other words, Langevin radiation pressure depends only on acoustic waves, while Rayleigh radiation pressure depends on both the waves and spatial constraints (Lee &

Wang, 1993). Imagine a cylinder with a target at its one end. If the other end is closed with an oscillating piston, the target will feel Rayleigh radiation pressure. If the piston is smaller than the cylinder, we talk about Langevin radiation force exerted on the target.

Rayleigh radiation pressure exerted on a target is (Beyer, 1974; Chu & Apfel, 1982)

$$\langle p_R - p_0 \rangle = \frac{1}{2}\left(1 + \frac{B}{2A}\right)\langle E \rangle \qquad \text{Eq. 2.32}$$

where B/A is a measure of the nonlinearity in a medium.[12]

Even if the sound beam completely fills the tube, a target smaller than the diameter of the sound beam (dendrites in our case) will feel Langevin radiation pressure. For unbounded beam, Langevin radiation pressure is

$$\langle p_L - p_0 \rangle \approx \langle E \rangle \qquad \text{Eq. 2.33}$$

A correction for a confined space was given by Chu and Apfel (1982):

$$\langle p_L - p_0 \rangle = \langle E \rangle + \rho_0 C$$

$$C = -\left\langle \rho_0 c_0^2 \left(\frac{1}{\rho_L} - \frac{1}{\rho_0}\right) - \frac{1}{2}\left(\rho^2 \frac{d\left(\rho c^2\right)}{d\rho}\right)_0 \left(\frac{1}{\rho_L} - \frac{1}{\rho_0}\right)^2 + \frac{v_L^2}{2} \right\rangle \qquad \text{Eq. 2.34}$$

where the subscript L means the quantity is in Lagrangian coordinates, while the subscript zero (0) has the same meaning as in Section 2.2.2.

These relations were derived for a large target, meaning that the radiation force is significant only on the frontal side, while the action on lateral and back sides does not make significant effects. For two and three dimensional cases, like when the radiation force is acting on dendrite branches, radiation pressure should be a member of the radiation stress tensor (Brillouin, 1964; Beissner, 1984):

$$\sigma_{ij} = -\langle p \rangle \delta_{ij} - \rho \langle v_i v_j \rangle \qquad \text{Eq. 2.35}$$

---

[12] A and B are, respectively, coefficients of the linear and quadratic terms of Taylor series when the pressure change is expressed as a function of the density change. B/A depends on temperature and pressure, and values for some liquids are given by Beyer (1974). For distilled water $B/A = 4.2$ at 0 ºC, 5.0 at 20 ºC, and so on.

In this symmetric tensor, δ_{ij} is the Kronecker delta, $p = p_a + p_0$, while v_i and v_j are velocity components.

Acoustic streaming and radiation pressure are connected – the stronger the streaming the lower the radiation pressure.

2.3. Nucleation and Crystal Growth

The classical nucleation theory was largely popularized by the work of Turnbull in the late 1940's and early 1950's (Fisher, Hollomon, & Turnbull, 1948; Turnbull & Fisher, 1949; Fisher, Hollomon, & Turnbull, 1949; Turnbull, 1950a; Turnbull, 1950b). In the period from 1948 to 1956 Turnbull authored and coauthored 27 publications on nucleation. A brief historical overview of contributions before Turnbull was given by Cahn (1987); most of them are also referenced in papers of Turnbull and coworkers. One can find numerous overviews of the classical nucleation theory, in more or less detail, for example in books by Frenkel (1955), one of developers of the theory, Chalmers (1964), Flemings (1974), Kurz and Fisher (1998), Stefanescu (2009), then in papers by Hollomon and Turnbull (1953), Melia (1965), Binsbergen (1973), Russell (1980), Glicksman and Sellek (1987), Anisimov (2003), Hecht et al. (2004), to name a few. The exposition of this topic will be limited only to the effects of pressure and supercooling on nucleation, which is of primary interest in this work.

As mentioned in Section 2.1.2, the work of the pressure on the solid particle is neglected in the nucleation theory. As will be shown later, only supercooling participates in expressions for nucleation rate. Hence the effect of pressure can be taken into account only indirectly through the supercooling, since applied pressure changes the melting temperature. This topic will be mentioned first.

2.3.1. Effect of Pressure on the Equilibrium Melting Point

The relation between applied pressure and the change in the equilibrium melting temperature of a pure substance is given by the Clapeyron equation (Flemings, 1974)

$$\frac{T_M - T_{M.p}}{p - p_{atm}} = -\frac{T_{M.1}\left(\bar{V}_S - \bar{V}_L\right)}{H_S - H_L} = -\frac{T_M\left(\bar{V}_S - \bar{V}_L\right)}{\Delta H_f} \qquad \text{Eq. 2.36}$$

where $T_{M.1}$ and $T_{M.p}$ are the equilibrium melting temperatures at atmospheric pressure p_{atm}, and some other pressure p, respectively. $\bar{V}$ and H are specific volumes (m^3/mol or m^3/kg) and enthalpies (J/mol or J/kg) of the solid and liquid phase, as indicated by subscripts S and L. ΔH_f is enthalpy (heat) of fusion, or latent heat. A very nice derivation of the Clapeyron equation can be found in the book by Fermi (1956).

For a binary alloy of components A and B the pressure dependence of the partition coefficient around pure A (alloy with a small amount of B) is

$$k_p^A = k^A\left[1 - \frac{\left(\bar{V}_S^B - \bar{V}_L^B\right)\left(p - p_{atm}\right)}{R_{gas}T_{M.1}^A}\right] \qquad \text{Eq. 2.37}$$

where k^A is the partition coefficient at atmospheric pressure, $\Delta\bar{V}^B = \bar{V}_S^B - \bar{V}_L^B$ is the change in partial molar volume during solidification of component B, and R_{gas} is the universal gas constant. The liquidus slope for diluted solution of B in A is (Flemings, 1974)

$$m_{L.p}^A = \frac{R_{gas}\left(T_{M.1}^A\right)^2\left(1 - k_p^A\right)}{\Delta H_f^A} \qquad \text{Eq. 2.38}$$

where ΔH_f^A is the heat of fusion of pure A.

Using Eq. 2.36, Eq. 2.37 and Eq. 2.38, one can construct a simplified phase diagram for diluted ideal and real solutions under the influence of pressure. This is illustrated in Figure 2.13. To describe the effects of pressure on diluted solutions of A in B one needs only to change superscripts in previous equations.

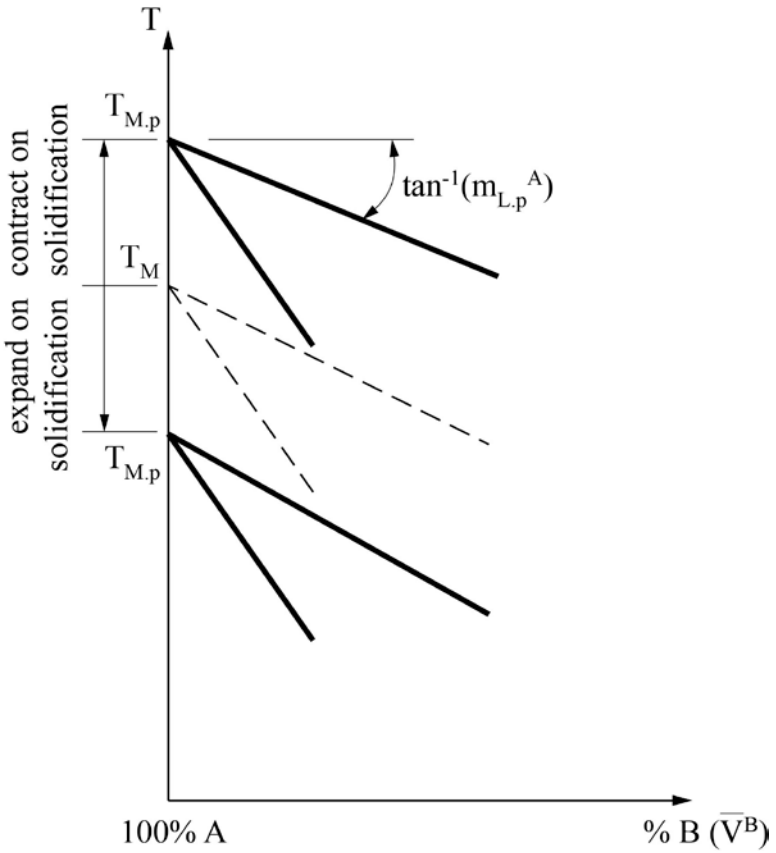

Figure 2.13. Effect of increased pressure, $p > p_{atm}$, on melting point of a pure substance A and liquidus and solidus temperatures of $A-B$ alloy.

Eq. 2.36 serves for illustrative purposes to qualitatively show effects of changes in pressure and density on the melting temperature. The type of the relationship used in practice was proposed by Simon and Glatzel (1929). One of the widely used forms of this equation, known as Simon equation, is (Babb, 1963)

$$\frac{p - p_{tp}}{a} = \left(\frac{T_{M.\mathrm{p}}}{T_{tp}} \right)^{c} - 1 \qquad \text{Eq. 2.39}$$

where p_{tp} and T_{tp} are pressure and temperature of the triple point, $T_{M.p}$ is the melting temperature at pressure p, while a and c are empirically determined constants. Pressure at the triple point is usually neglected in this equation (Babb, 1963). Babb (1963) gave a comprehensive summary of values for T_{tp}, a, and c from Eq. 2.39 for large number of

materials, or just gradients [bar/ ºC] for materials without constants a and c determined at that time. An example for a few materials is given in Table 2.1.

Table 2.1. *Values of T_{tp}, a, and c for some materials (Babb, 1963). Original article (Babb, 1963) gives values for large number of materials.*

Material	T_{tp} [K]	a [bar]	c	Δp_T [bar/ ºC]	Pressure range [kbar]
Al	933.3	–	–	156	≤ 18 (50)
Cu	1356.2	–	–	213	≤ 18
Fe	1805	1,070,000	1.76	–	≤ 80
Water I	273.15	-3952	9	–	≤ 2
Water III	251.2	620	60	–	2.115-3.5
Water V	256.2	4100	8.1	–	3.53-6.38
Water VI	273.32	7070	4.46	–	6.38-22.4
Water VII	354.8	12980	3.11	–	22.4-40
Succinonitrile	330.1	–	–	44.995	≤ 1

As noted by Flemings (1974), and inferred from the paper by Babb (1963), the equilibrium melting temperature of most liquid metals shifts only around 10^{-2} ºC per one atmosphere of applied pressure. Hence changes in the melting temperature become significant only when the pressure exceed 1000 atmospheres. Hence the pressure field developed around collapsing cavities is sufficient to change enough the equilibrium melting point of surrounding liquid phase.

2.3.2. Nucleation Rate

In classic nucleation theory, the rate of heterogeneous nucleation of stable nuclei at temperature T is estimated as

$$J_{het} = J_0 \exp\left(-\frac{\Delta G_d + \Delta G_{SL}^*}{k_B T} f(\Theta)\right) = J_0 \exp\left[-\frac{\Delta G_d}{k_B T} f(\Theta)\right] \exp\left[-\frac{16\pi}{3} \cdot \frac{\sigma_{SL}^3 T_{M.p}^2}{\Delta H_f^2 k_B T \left(T - T_{M.p}\right)^2} \bar{V}_S^2 f(\Theta)\right] \quad \text{Eq. 2.40}$$

where $f(\Theta)$ is the geometric factor in the spherical cap model, which depends on the "wetting" angle Θ between the growing solid phase and the material of a nucleation seed (Figure 2.14), is calculated

$$f(\Theta) = \frac{2 - 3\cos\Theta + \cos^3\Theta}{4} = \frac{(2 + \cos\Theta)(1 - \cos\Theta)^2}{4} \quad \text{Eq. 2.41}$$

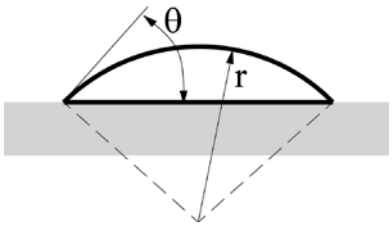

Figure 2.14. "Wetting" angle Θ of a crystal on the substrate in the spherical cap model.

It should be noted that the free energy barrier for heterogeneous nucleation is

$$\Delta G_{het}^* = \Delta G_{hom}^* f(\Theta) = \left(\Delta G_d + \Delta G_{SL}^*\right) f(\Theta) \quad \text{Eq. 2.42}$$

so the rate of homogeneous nucleation is calculated from Eq. 2.40 using $f(\Theta) = 1$, as $\Theta = 180°$ in that case. ΔG_d is energy required for interface diffusion, i.e. transfer of atoms through the solid/liquid interface. ΔG_{SL}^* is the maximum positive difference in free energy between solid and liquid phases, i.e. the maximum free energy necessary for nucleus formation, Figure 2.15, calculated as

$$\Delta G_{SL}^* = \frac{16\pi}{3} \frac{\sigma_{SL}^3}{\Delta G_V^2} \quad \text{Eq. 2.43}$$

$\Delta G_V = \Delta G / \bar{V}_S$ is the change in the Gibbs free energy for formation of the unit volume of solid phase, $\bar{V}_S$; σ_{SL} is the solid-liquid interface energy. The energy barrier ΔG^*_{SL} corresponds to the critical radius, Figure 2.15:

$$r^* = -2\frac{\sigma_{SL}}{\Delta G_V} \qquad \text{Eq. 2.44}$$

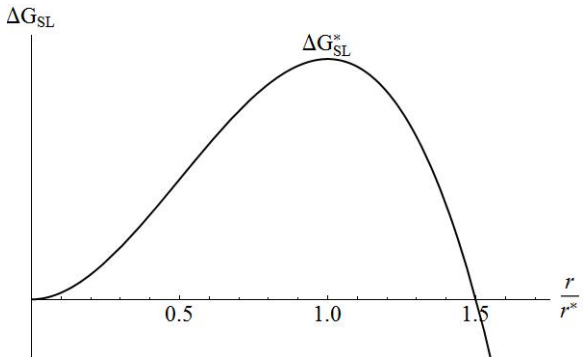

Figure 2.15. Variation of free energy of nucleation as a function of the radius of nuclei, where r^* is the critical radius.

For the substrate completely wetted with the liquid ($\Theta = 0°$) this model predicts no energy barrier for heterogeneous nucleation even at zero supercooling, i.e. $J_{het} = J_0$. Theoretically, the same applies to the existing nuclei from the same material as the liquid. In this case, however, there is no nucleation; instead, the crystal grows from the existing nucleus. The other extreme is when the liquid does not interact with the substrate ($\Theta = 180°$); then $f(\Theta) = 1$ and Eq. 2.40 describes homogeneous nucleation.

The pre-exponential factor is estimated as $J_0 = B_0 f_{atom}$, where $B_0 \approx 10^{29}\, m^{-3}$ is some rough average of the density of atoms, and the resonant frequency of atoms is roughly $f_{atom} \approx 10^{12}\, Hz$. The exponential term in Eq. 2.40 containing activation energy for transfer of atoms through the solid/liquid interface, ΔG_d, is estimated to be around 10^{-2} for small supercooling, so (Kurz & Fisher, 1998)

$$J_0 \exp\left[-\frac{\Delta G_d}{k_B T} f(\Theta)\right] \approx 10^{39}\, m^{-3} s^{-1} \qquad \text{Eq. 2.45}$$

Again, this approximation is not valid for large supercooling, which is believed to exist when cavities collapse. A good circumstance is that the nucleation rate is not sensitive to the pre-exponential factor, which can vary several orders of magnitude without significant change in the nucleation rate; hence estimation in Eq. 2.45 of the first two terms in Eq. 2.40 should not make a significant difference in the final result.

On the other hand, the nucleation rate is very sensitive to the second exponential term in Eq. 2.40 (Kurz & Fisher, 1998). That requires quite accurate values of the geometric factor $f(\Theta)$ and the interfacial energy σ_{SL} in order to estimate the nucleation rate within the order of magnitude. Now, the first problem is "the paucity of interfacial energy values" (Southin & Chadwick, 1978). The other problem is that acoustic cavitation changes the wetting angle Θ, a phenomenon termed emulsification (Abramov O. V., 1998). As this phenomenon is largely unpredictable and hard to capture quantitatively, the geometric factor $f(\Theta)$ alone can create errors in estimating the nucleation rate in the presence of cavitation.

While the driving force for nucleation of a pure material can be assumed as directly proportional to the supercooling, the driving force for alloys is proportional both to the supercooling and alloy composition (Cantor & Doherty, 1979; Thompson & Spaepen, 1983).

Following Thompson and Spaepen (1983), Eq. 2.40 can be used for an alloy with components A and B, and the initial composition $C_0 = C^A$ ($C^B = 1 - C^A$), respectively. Assuming formation of the phase with the highest difference in the Gibbs free energy,

$$\Delta G_V = \Delta\mu^A / \bar{V}_S = \Delta\mu^B / \bar{V}_S \qquad \text{Eq. 2.46}$$

where $\Delta\mu^A = \mu_L^A - \mu_S^A$ is the difference in chemical potential between the liquid and solid phase of the pure component A, and analogously for the component B, $\Delta\mu^B = \mu_L^B - \mu_S^B$. The average volume of the solid phase with the composition C_S^A is assumed as a simple mixture:

$$\bar{V}_S = C_S^A \bar{V}_S^A + \left(1 - C_S^A\right)\bar{V}_S^B \qquad \text{Eq. 2.47}$$

The change in chemical potential upon solidification of a component i, $i = A, B$, at temperature T is approximately

$$\Delta\mu^i = (T_L - T)\Delta S_f^i + R_{gas} T \ln\left(C_L^i / C_S^i\right) - R_{gas} T_L \ln\left(C_L^i / C_{S.eq}^i\right), \quad i = A, B \qquad \text{Eq. 2.48}$$

where T_L, C_L^i, and $C_{S.eq}^i$ are, respectively, the liquidus temperature, and concentrations of the component i in the liquid and solid phase; they are all taken from the equilibrium phase diagram. ΔS_f^i is the entropy of fusion of the component i. For the $A-B$ alloy

$$\Delta S_f = C_S^A \Delta S_f^A + \left(1 - C_S^A\right)\Delta S_f^B \qquad \text{Eq. 2.49}$$

The solid-liquid surface energy at temperature T is

$$\sigma_{SL} = \frac{\alpha_m \Delta S_f}{\left(N_A \bar{V}_S^2\right)^{1/3}} T \qquad \text{Eq. 2.50}$$

where N_A is the Avogardo's number, $\alpha_m = 0.86$ for f.c.c. and hc.p., and $\alpha_m = 0.71$ for b.c.c. lattice.

Eq. 2.46 through Eq. 2.50 describe a pure substance if the composition of only one phase is taken to be unity, while all other zero.

2.3.3. Crystal Growth

In this work we are interested mostly in the nucleation and the very early stage of the crystal growth. Theoretical expressions for the velocity of the crystal growth are derived mainly with the assumption of small supercooling. They are not suitable for large supercoolings expected to exist around collapsing bubbles during ultrasonically induced cavitation. Anyway, theoretical expressions for the velocity of the solid-liquid interface are not usually used; instead, empirically determined functions of the supercooling, ΔT, are used which have the following form:

$$V = c_1 \Delta T^{c_2} \qquad \text{Eq. 2.51}$$

Constants c_1 and c_2 are determined experimentally.

Supercooling above which the mechanism of crystal growth changes from the lateral step growth to the continuous growth is (Cahn, 1960; Cahn, Hilling, & Sears, 1964)

$$\Delta T^* = \pi \frac{\sigma_{SL} \bar{V}_S T_M}{\Delta H_f} \frac{\pi x^3 \exp(-\pi x)}{a_{HS}} \qquad \text{Eq. 2.52}$$

Here a_{HS} is the step height, and $x = \pi n / 2$, where n is the number of molecular layers which make transition region between the liquid and solid phases. The transitional crystal growth mechanism occurs in the interval of supercoolings:

$$\Delta T^* / \pi < \Delta T < \Delta T^* \qquad \text{Eq. 2.53}$$

One example of Eq. 2.51 for the growth velocity of ice crystals in supercooled water is (Pruppacher, 1967)

$$\begin{aligned} V &= 0.035(\Delta T)^{2.22} \quad for\ \Delta T < 9\,°C \\ V &= 2.5\Delta T \qquad\qquad for\ \Delta T > 9\,°C \end{aligned} \qquad \text{Eq. 2.54}$$

where V is in cm/s and ΔT is in ºC. Pruppacher determined that ice grows according to the lateral growth mechanism when ΔT from 0 to 3.25 ºC, according to the transitional lateral step mechanism when ΔT is from 3.25 to 9.0 ºC, and the continuous growth mechanism for ΔT larger than 9 ºC.

The solid-liquid interface of the growing crystal will become unstable, if the growth velocity is (Kurz & Fisher, 1998)

$$\frac{k G_L D_L}{m_L (1-k) C_0} < V < \frac{m_L (1-k) C_0 D_L}{k \Gamma_{SL}} \qquad \text{Eq. 2.55}$$

In this range of velocities the crystal will undergo cellular/dendritic growth.[13]

$\Gamma_{SL} = \sigma_{SL} T_M / (\rho_S \Delta H_f)$ is the Gibbs-Thomson coefficient, G_L is the temperature gradient at the liquid side of the solid-liquid interface, D_L is the coefficient of diffusion in the

---

[13] For large V, like in rapid solidification processes, the liquidus slope m_L and the partition coefficient k depend on V itself. So in the upper limit of Eq. 2.55, the limit of absolute stability, m_L and k should not be constant as in the lower limit (instability limit).

liquid phase, and the other parameters as defined above. C_0 is the initial alloy composition.

We will use in Section 5.4 the following expression for the dendrite tip radius (Kurz & Fisher, 1998): $r_{dendr} \approx \sqrt{4\pi^2\Gamma / \left(m_L G_C - G_L\right)}$, due to its simplicity, to illustrate the effect of supercooling on coarseness of ice dendrites. In this equation, G_C and G_L are effective concentration and temperature gradients. Applied to the growth of ice, this equation takes the form

$$r_{dendr} \approx \sqrt{-4\pi^2\Gamma / G} \qquad \text{Eq. 2.56}$$

so only negative temperature gradients will give real values for the radius. Positive values give imaginary radius of the dendrite, meaning there is no dendrite.

Stability of the solidification front in pure substances depends on G_L – dendrites will grow in supercooled liquid when G_L is negative, while the planar growth occurs when G_L is positive (Kurz & Fisher, 1998). This is in accordance with Eq. 2.56.

2.4. Effects of Ultrasonic Vibrations on Nucleation, Crystal Growth, and Grain Refinement

The extent to which the ultrasonic filed affects solidification certainly depends on many factors, the most important being the type of material and the geometry of processed part, cooling conditions. These complex interrelations are graphically summarized in Figure 2.16 (Abramov O. V., 1987). As can be seen from this figure, Abramov lists cavitation and acoustic streaming as the most important features of the ultrasonic filed on the solidification process.

According to Figure 2.16, the main results of applied ultrasonic field are grain refinement, degassing, increase of homogeneity, and dispersion of crystals. One should add to this list the acceleration of other rate processes, like thermal diffusion, dross removal, and also non-metallurgical effects, like surface cleaning, passivity, and so on (Heidemann, 1954).

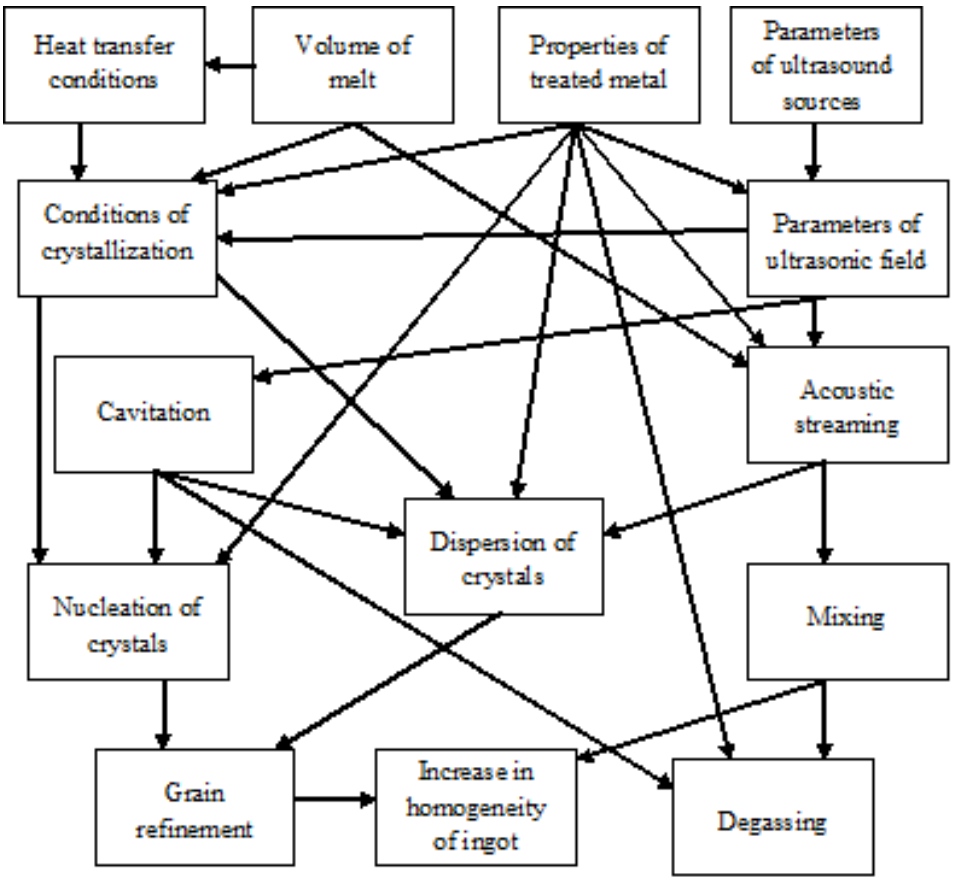

Figure 2.16. Effect of ultrasound on the crystallization process. Reproduced from Abramov (1987).

In his monograph, Kapustin (1963) gave an overview of experimental observations on the effects of ultrasound on solidification process. Observations were made mostly on transparent and/or organic materials, like thymol ($C_{10}H_{14}O$), salol ($C_{13}H_{10}O_3$), benzophenone ($C_{13}H_{10}O$), methanol (CH_3OH), o-chloronitrobenzene ($C_6H_4ClNO_2$), ammonium chloride (NH_4Cl), even milk. Some metals and alloys were also investigated: zinc, lead, duralumin, Wood's metal. Kapustin compiled results from the literature as well as his own work; many results are from his doctoral dissertation

from 1951, the topic of which is very much with this work. [14] The main conclusions drawn from this work can be summarized as follows:[15]

1. Ultrasonic field increases the number of nuclei by a twofold action: increased nucleation rate in the bulk of the liquid phase, and fragmentation of growing crystals.
2. Ultrasonic field produces large number of small nuclei which coalesce and become larger. Only after their growth and coalescence, these nuclei become visible. They originate ahead of the solidification front, and after they reach certain size by coalescence and growth, they get pushed to the solid-liquid interface. Kapustin observed that ultrasound affects creation of first crystallization centers near the limit of metastability. He did not explicitly mention that large pressure which develops during the bubble collapse could cause nucleation. On the other hand, he mentions the model of heterophase fluctuations developed by Frenkel (1955) from Gibbs' theory. By this model, the liquid already contains nuclei before both phases are in the thermodynamic equilibrium. Kapustin proposes that ultrasound redistributes those nuclei and changes the probability of spontaneous nucleation from them.
3. Crystals that break away from the solidification front become more fragmented, contributing to the further increase in the number of active nuclei.
4. Application of ultrasound completely suppresses formation of columnar structure.
5. In materials which produce eutectic phase at the end of solidification, ultrasonic field accelerates the start of eutectic solidification.
6. The intensity of ultrasonic field is a significant parameter. Materials that solidified when the intensity is low show both regions with unaffected crystal size as well as

---

[14] Kapustin, A. P. (1951). *An Experimental Study of the Effects of Ultrasonics on the Kinetics of Crystallization*. Dissertation.
Unfortunately, the dissertation is not accessible to the author of this work.

[15] Conclusions made by Kapustin are influenced by the experimental setup he used. In his experiments ultrasound was applied indirectly to a liquid that surrounds the container with the sample to be solidified.

regions with refined crystals. In general, there is a minimum level of acoustic intensity below which no significant changes occur. This is explained by the absence of cavitation; instead, only slight vibrations of the container walls exist. Also, there is an upper limit of the intensity beyond which there is no further increase in the solidification rate or grain refinement; in other words, saturation is reached. This was explained by the large amount of latent heat released during accelerated solidification.

7. Like with the intensity of ultrasound, frequency influences solidification rate and grain size only if within some range of magnitudes which is bounded with an upper and lower limit. Differently from the intensity, the frequency of ultrasound within these limits does not make much influence on both the microstructure and solidification rate. The cause is related with the frequency-dependent cavitation.
8. It is possible to obtain modified structure applying wide range of intensities and frequencies.
9. Solidification rate is increased by a large factor, more than 100, in materials which allow “considerable supercooling”, despite heating of the melt to some extent by the ultrasonic field.
10. Application of the ultrasonic field increases homogeneity of crystallized microstructure.
11. Zonal microstructures can be formed using the ultrasonic field. One method is to locate finer structure in antinodes and coarser in nodal planes; this is obviously related to standing waves. The other way is to apply ultrasound periodically.
12. Crystal seeds have to be used for many materials exposed to the ultrasonic field at moderate intensities, or when supercooling is small. Under high ultrasound intensities, crystallization rate increases enormously after introduction of seeds.
13. In the case of low supercooling, crystalline seed is highly dispersed and it is possible to obtain crystallization throughout the volume. Acoustic intensity then does not play a critical role. At medium intensities, crystallization occurs both at the walls and within the volume, the former rate being higher due to vibrations of the

walls (again, this observation is highly related to the experimental setup where ultrasonic vibrations are applied outside the container).

14. The time delay for nucleation on impurities decreases with the increase in the ultrasound intensity if the supercooling is large enough. For small degrees of supercooling the time delay can be increased with increased intensity, which is related with heating due to absorption of acoustic energy.
15. Weak ultrasonic fields produce larger grain size as compared with high intensities of the field.
16. It seems that ultrasonic field does not have much influence on solidification when supercooling is very large.
17. The shape of the container (mold) does not make big difference in the effects of the ultrasonic field on solidification.
18. The distance between the sonotrode[16] and the solidification front is important when the main direction of the propagation of ultrasound is parallel to the solidification front. The solidification rate increases as the sonotrode is brought closer to the solidification front.
19. Hydrostatic pressure is an important parameter, with the maximum reduction in grain size obtained near atmospheric pressure. It is interesting that hydrostatic pressures above 4 atmospheres did not affect grain size of thymol.
20. Another effect of the ultrasonic field is practically complete elimination of gas from the melt.

Many of these conclusions, largely based on the dissertation which dates back to 1951, still hold. Kapustin claimed that the main effects of grain refinement are due to increased nucleation rate and dispersion of crystals, which agrees with illustration in Figure 2.16. It seems that Kapustin gave advantage to heterophase fluctuations over the cavitation collapse as the reason for increased nucleation rate. For example, on page 41 of

---

[16] Sonotrode, horn, and radiator are terms which refer to the same ting – a rod that transmits vibrations to the processed material. The term sonotrode is obviously an acoustic analogy to electrode, and will be given slightly preference in this work.

the monograph it says “Ultrasound affects crystallization by producing many fresh nuclei from any seed that may be present in the supercooled liquid”.

Today, the adiabatic compression of the liquid phase during the collapse and rebound of cavities is mentioned as the sole reason for the acceleration of the nucleation rate. Experimental evidence of this phenomenon is now available. Ohsaka and Trinh (1998) captured the formation of an ice crystal at the spot of collapsing bubble. They introduced one bubble in a levitation cell (with standing ultrasonic field); in that way the camera could be focused on the bubble forced to oscillate in a non-sonoluminescencing mode.

Based on his calculations with Plesset (Hickling & Plesset, 1964), Hickling showed (1965a; 1965b; 1994) that adiabatically compressed liquid heats up, but the temperature developed in that way is below the freezing point of the liquid at such high pressures. He showed that supercooling in water can be of the order of 100 K.

Hunt and Jackson (1966a; 1966b) agreed that the nucleation happens during the collapse of a cavity, but opposed the theory that the nucleation happens when the liquid is compressed. Instead, they suggested that the nucleation occurs when the liquid is locally in tension. They base their assumption by calculating the temperature change around the cavity as an irreversible compression process. In that way the calculated liquid temperature at high pressures is actually above the equilibrium freezing point. They concluded that nucleation has to be initiated when the liquid is locally in tension; in other words nucleation is caused by the counterjet, not the outgoing shock wave. However, an irreversible compression has not been widely accepted so far. Instead, adiabatic compression is used exclusively to estimate the temperature and pressure field around collapsing bubble.

It remains accepted that the nucleation happens during the collapse of cavities. If these nuclei survive during the crystallization process keeping large enough size, they can effectively produce smaller grain size. These effects have been reported in published literature. According to Eskin (1994), the number of active nuclei in commercial aluminum ingots can be increased from more than 10^3 times in larger ingots (around 1 meter in diameter) up to 10^6 times in ingots with smaller diameters (around 60 mm).

Ultrasound which produces cavitation actually alters the shape of crystallization front, and the final roughness does not dependent on the roughness developed before ultrasound is applied (Abramov O. V., 1987). This is caused by detachment of growing crystals and their dispersion into the bulk of the melt, as mentioned in conclusion 3 from Kapustin's work. The number of these detached crystals which can serve as active nuclei adds to the number of active nuclei crated by cavitation to account for the total number of active sites for further crystal growth. Contrary to the cavitation regime, the ultrasonic field with intensities below the cavitation threshold smoothens the solidification front (Abramov O. V., 1987).

Presence of impurities can lower the cavitation threshold. Also, vibrations enhance activation of impurities, so they contribute to the increase in the number of active nuclei. For example, tin doped with Al_2O_3, SiO_2, and W produced fairly large grain size when solidified without ultrasonic field, meaning the impurities had not been activated. On the other hand, significant grain refinement was achieved when the ultrasonic field was applied during solidification (Abramov O. V., 1987). According to Eskin (1994), the majority of impurity particles in the melt are non-soluble and non-wetted particles smaller than 0.1 μm. Indeed, at most 1% of added commercial refiners are active (Greer, Bunn, Tronche, Evans, & Bristow, 2000). Since non-wetted, these particles contain some gas at the boundary between them and the liquid. As mentioned in Section 2.1.2, gas around impurities lowers significantly the cavitation threshold, serving as a cavitation nucleus. Hence an ultrasonic field, predominantly cavitation caused by it, helps emulsification of inactive particles.

Abramov (1987) also reported shorter delay time for the occurrence of first crystallization centers, which agrees with conclusion 14 from Kapustin's work.

Connecting with conclusions 1 and 2 above, one expects that increased temperature gradient in the liquid should decrease the amount of nuclei formed ahead of the crystallization front. Also, slower crystallization rate decreases the amount of fragmented crystals, as per conclusions 1 and 3. Smaller temperature gradient together with faster growth rate can be achieved only if the liquid is supercooled; this is in agreement with conclusion 9 which states that the degree of grain refinement increases in

liquids which allow larger supercooling. Also, it is known that that the tendency towards large grain size increases as the solidification interval increases. All these effects support conclusions of Abramov (1987) that the degree of grain refinement decreases when the temperature gradient increases, the crystallization rate decreases, and the difference between liquidus and solidus temperatures decreases.

Table 2.2 shows some examples of the change in mechanical properties of two aluminum alloys after final treatment if the raw material is produced under an ultrasonic field. The main effect is in the increase of ductility of as cast and heat treated parts. Samples produced by rolling show increased and more uniform ductility if they have non-dendritic structure. Besides that they also show more significant increase in tensile mechanical properties.

Table 2.2. *Influence of ultrasonic vibrations on final mechanical properties of aluminum alloys 7050 and 2324 (Eskin, 2001).*

Aluminum alloy	State	Ingot structure	Yield strength (MPa)	Tensile strength (MPa)	Relative elongation (%)	Relative contraction (%)	Fatigue limit (MPa)
7050	After heat treatment	Dendritic	405	461	5.6	10.1	
		Non-dendritic	400	463	8.8	30	
	Rolled plates	Dendritic		438-445	0.5-1.0		
		Non-dendritic		530-532	1.8-2.0		
2324		Dendritic		351-382	0.8-4.4		130
		Non-dendritic		390-395	4.4-4.8		150

The effect of ultrasound on mechanical properties of several types of steel is illustrated in Table 2.3. According to the data in table, the main benefit is again increased ductility. Two unalloyed carbon steels also exhibit significant increase in the tensile strength. Increased mechanical properties are preserved even in highly alloyed steels after

plastic deformation and heat treatment, despite the influence of alloying elements on the microstructure, and then strong effects of metal working and heat treatment on initial structure.

Table 2.3. *The effect of ultrasound on mechanical properties of several types of steels (Abramov O. V., 1987).*

Steel	State	Condition[a)]	Test temperature (ºC)	YS (MPa)	UTS (MPa)	Relative elongation (%)	Relative contraction (%)	Impact strength (MJm^{-2})
0.5% C	Cast	C	20		490	10	15	0.15
		US	20		630	18	28	0.28
1% C	Cast	C	20	400	489	2	5	
		US	20	410	850	3	9	
0.4%C, 1%Cr, 0.58%Ni	Cast	C	20	560	880	9	14	
		US	20	570	900	12	25	
0.4%C, 1%Cr, 5%Ni	Deformed and heat treated	C	20	2300	2380	4	40	0.38
		US	20	2430	2530	4	50	0.57
20%Cr, 20%Ni, 3%Mo	Cast	C	20		490	42	40	
		US	20		550	54	68	
		C	900		140	22	18	1.1
		US	900		170	28	26	1.7
18%Cr, 15%Ni, 3%B	Cast	C	900		180	3	0	
		US	900		240	11	14	
	Deformed	C	900		180	7	25	
		US	900		220	11	40	

[a)] C: control sample (without ultrasound); US: sample solidified in an ultrasonic field

The main benefit of the use of an ultrasonic field during solidification is that non-dendritic structure has increased ductility compared to dendritic structure solidified without ultrasound, which is suitable for subsequent hot working; non-dendritic structure persists in all processes of hot working (Eskin, 1998; 2001). Ultrasound effectively modifies brittle silicon phase in various Al-Si alloys, so it becomes much finer (Abramov

V. O., Abramov, Straumal, & Gust, 1997; Abramov V. , Abramov, Bulgakov, & Sommer, 1998; Jian, Xu, Meek, & Han, 2005; Jian, Meek, & Han, 2006; Zhang, Zhao, Cheng, Chen, & Dai, 2009; Yu, Feng, Li, & Gong, 2009). Refinement of the silicon phase certainly enhances ductility of these alloys. Besides improved morphology in A356 aluminum alloy, the ultimate tensile strength, yield strength, and elongation were 1.55, 1.95, and 1.10 times higher, respectively, if the material was solidified under an ultrasonic field (Zhang, Zhao, Cheng, Chen, & Dai, 2009). It was also shown that AlSi9Cu3(Fe) alloy solidified in an ultrasonic field has increased mechanical properties and decreased porosity, in addition to refined morphology (Puga, et al., 2013). Al-23Si alloy exhibits better strain hardening, more uniform distribution of microhardness, and better wear resistance if solidified in an ultrasonic field (Yu, Feng, Li, & Gong, 2009). Some examples of improved manufacturability of hot worked products of some aluminum alloys and their improved properties in a form of a final product are given by Eskin (1998; 2001).

Also reported are improved morphologies of some Mg alloys (Shepelev, et al., 2008; Qian, Ramirez, & Das, 2009; Qian, Ramirez, Das, & StJohn, 2010; Aghayani & Niroumand, 2011).

Another very important aspect of the application of ultrasound is very efficient degassing of the melt (Eskin, 1998; Xu, Jian, Meek, & Han, 2004; Xu, Han, & Meek, 2008), which is associated with reduced porosity.

The effects of fluid flow on dendrite detachment were studied by Paradies, Glicksman, and coworkers (Paradies, Kim, Glicksman, & Smith, 1993; Paradies, Smith, & Glicksman, 1997). According to them, the most probable mechanisms are constitutional remelting in the roots of primary dendrite arms and capillary pinching. Some other mechanisms might also be probable, but mechanical shearing does not seem to cause fragmentation and detachment of dendrites. These conclusions were based on solidification with forced or natural convection in the liquid phase, not ultrasound. However, shock waves produced by cavitation can provide mechanical means of fragmentation. Interestingly, only fragmentation of growing dendrites was mentioned by

Glicksman (2011) as the mechanism of grain refinement due to shock waves emitted by collapsing cavities; no nucleation was mentioned.

Also, Glicksman (2011) seems very skeptical about application of ultrasound in the real-world solidification processing (metalcasting) due to the cost of the equipment and difficulties in implementing the processing conditions uniformly over the casting. Indeed, Qian et al. (2009) obtained grain refinement of pure magnesium and AZ31 alloy only in the area adjacent to the face of the sonotrode, the grain size increasing progressively with the distance from it. The grain size also increased in the melt that is off the main direction of ultrasound propagation. Qian et al. did not obtain the chill effect from the surfaces of the radiator since grains were not refined around the cylindrical faces of the sonotrode. Based on their experimental findings, they suggested that fragmentation and detachment of growing dendrites are not likely to cause grain refinement. Instead, they propose cavitation induced nucleation as the main mechanism of grain refinement.

There is a very interesting experimental investigation on the influence of solute on on grain refinement when ultrasound is applied (Qian, Ramirez, Das, & StJohn, 2010). It was shown that the grain density increases linearly with the increase in the solute concentration. The type of solute is also important. Aluminum showed to be more efficient than zinc as a solute element in magnesium. Grain refinement of pure magnesium without solute was significantly less efficient, even by using intensity of 1700 W/cm^2, producing around 64 $grains/mm^3$. On the contrary, grain density of 5640 $grains/mm^3$ was produced in magnesium with 9% Al under the same conditions of ultrasonic irradiation.

Contrary to above mentioned difficulties to obtain uniform grain refinement even in small volume specimens, which is frequently found in the literature, and probably experienced by Glicksman himself, Eskin shows a picture of a ten-ton ingot from A2324 alloy with grain size successfully refined throughout the volume with ultrasonic treatment (Eskin, 2001).

Some attempts to quantify nucleation rate influenced by ultrasonication have been published recently. Inada and coworkers used experiments to derive probability of ice nucleation as a function of the supercooling and acoustic intensity (Inada, Zhang, Yabe,

& Kozawa, 2001), and the density of bubble nuclei (Zhang, Inada, Yabe, Lu, & Kozawa, 2001; Zhang, Inada, & Tezuka, Ultrasonic-Induced Nucleation of Ice in Water Containing Air Bubbles, 2003). The probability of ice formation increases with the supercooling, acoustic intensity, and the bubble density. These authors also measured the frequency distribution of the supercooling at which purfied water solidifies, and obtained the mean value of 11.6 ºC. Yu et al. measured supercooling of around 12.89 ºC in degassed and 12.37 ºC if wate was not degassed (Yu, Liu, & Wang, 2012).

Maybe the first attempt to correlate the nucleation rate with the pressure that develops around the collapsing bubble was done by Virone et al. (Virone, Kramer, van Rosmalen, Stoop, & Bakker, 2006). It is interesting that they calculated pressure distribution assuming initial velocity of the bubble wall to be 11200 m/s, instead of finding that velocity from buble dynamics. Saclier at al. (2010) calculated the density of ice nuclei as a function of the supercooling and pressure around collapsing bubble. Their approach was to combine the Gilmore model, nucleation rate from the classic nucleation theory, and the size distribution of the bubble nuclei measured by Zhang et al. (Zhang, Inada, Yabe, Lu, & Kozawa, 2001).

Nastac (2011) combined simulation results of the fluid flow in commercial software with his previously published numerical model for prediction of the solidification morphology (Nastac, 1999). The predicted structure shows grains with very uniform size that is at least one order of magnitude lower than the predicted grain size obtained without ultrasonication. However, only few practical details are given on the modeling in the commercial software and how the connection with the previous model was made.

According to the knowledge of the author of this work, no much research on sonocrystallization of transparent materials has been published after work of Kapustin (1963). However, there are a number of recent publications on solidification of transparent materials influenced by ultrasound.

Based on experiments with camphene ($C_{10}H_{16}$), Swallowe at al. (Swallowe, Fields, Rees, & Duckworth, 1989) suggested that if dendrites grow close enough to the ultrasonic source, fragmentation of dendrites by attached bubbles is the primary

mechanism of grain refinement. They also showed nucleation of new crystals by ultrasound. The same observations of dendrite fragmentation by bubbles were reported recently (Chow, Blindt, Chivers, & Povey, 2003; Chow, Blindt, Kamp, Grocutt, & Chivers, 2004; Shu, Sun, Mi, & Grant, 2012). Chow et al. (Chow, Blindt, Kamp, Grocutt, & Chivers, 2004) also showed melting of ice grains when ultrasound is applied. Melting started at the crystal boundaries.

When a liquid is ultrasonicated, smaller supercooling necessary for nucleation has been widely reported. For example, ultrasonicated aqueous sucrose solutions with various concentrations froze within 1 ºC from the equilibrium frezing point, while untreated solutions needed 3 to 4 ºC supercooling (Chow, Blindt, Chivers, & Povey, 2003). It is interesting that Yu et al. (Yu, Liu, & Wang, 2012) still needed close to 6 ºC supercooling to nucleate ice during ultrasonication. The relatively high value can be explained by the indirect application of ultrasound through the coolant. Anyway, this supercooling was lower than 12.437 to 12.89 ºC needed for spontaneous nucleation.

The incuabtion time for nucleation is shoter when the liquid is ultrasonicated. The median incubation time in ammonium sulphate was 150 minutes in untreated samples and 39 minutes in ultrasonicated samples (Virone, Kramer, van Rosmalen, Stoop, & Bakker, 2006). The authors did not find a correlation between the duration of ultrasonication the incubation time.

Initial bubble density plays an important role. It has been shown that the incubation time is shorter if water contains more air bubbles (Zhang, Inada, & Tezuka, 2003; Yu, Liu, & Wang, 2012). Also, the supercooling required for ice nucleation in ultrasonicated samples is higher when water is degassed (Yu, Liu, & Wang, 2012), the difference being 4 ºC on average.

It has been experimentally observed that the nucleation supercooling decreases with increased acoustic intensity (Chow, Blindt, Chivers, & Povey, 2003; Chow, Bloindt, Chivers, & Povey, 2005; Yu, Liu, & Wang, 2012).

CHAPTER 3. METHODOLOGY

The effects of the ultrasonic vibrations on solidification processes have been studied for decades and a large body of knowledge has been collected so far. Section 2.4 gives a glimpse of that, and summarizes thus far accepted explanations for grain refinement by ultrasonic vibrations. In order to verify currently accepted mechanisms of microstructure modifications and identify possible new phenomena, a simple experimental setup has been designed. Its description is given in this section. One option was to design a solidification chamber with small thickness, so the growing dendrites can be in focus of a microscopic objective. In that case the crystallizers would have had one dimension much smaller the other two, which is a common practice. However, solidification in this work was performed in a cylindrical volume, sacrificing ability to observe small details. This decision is justified by trying to keep the acoustic field in the liquid as simple as possible, and avoid any asymmetries. In this case we could keep one-dimensional approximation of the acoustic field.

3.1. Experimental Setup

It is a common practice to observe nucleation and solidification in transparent substances. If a material has the Jackson factor less than two ($\alpha < 2$), solidification front will be non-faceted (Jackson, 1958; Jackson & Hunt, 1965). Hence solidification of transparent materials with $\alpha < 2$ can serve as an analog to solidification of metals. In this study, however, we are interested in nucleation processes and fragmentation of dendrites, not the morphology of crystal growth, so we are not limited to metal analogs. In this research were used:

1. Water purified by reverse osmosis, steam distillation, and ozonation. Ice is known for its faceted crystals.
2. Ammonium chloride (Avantar Performance Materials, Inc., Center Valley, PA), with chemical formula NH_4Cl. Ammonium chloride forms non-faceted crystals. An aqueous solution with around 4.5 wt% ammonium chloride was sued. Saturation (liquidus) temperature of the 4.5 wt% solution should be between -3.65 and -3.51 ºC, if the eutectic temperature is taken to be, respectively, -16.0 (Liu & Hellawell, 1999) or -15.4 ºC (Tan, 2009). This solution was chosen to imitate mushy region with low mechanical properties, since it is expected to consist of dendrites and liquid at temperatures slightly below saturation. Experiments were also performed with the hypereutectic composition of 25 wt%, but they brought no new information. In fact this composition was not suitable for this study due to excessive "snowing" effect. This effect has been reported before (Jackson, Hunt, Uhlmann, & Seward, 1966; Tan, 2009).
3. Succinonitrile (Tokyo Kasei Kogyo Co., Ltd., Tokyo, Japan), or shortly SCN, with chemical formula $CN(CH_2)CN$. It was diluted with around 5 wt% water. Saturation temperature of this solution should be around +35.16 ºC, as determined graphically from the phase diagram (Zhang, Liu, & Han, 2008). However, freezing and melting experiments showed both precipitation and dissolution to occur at +25 ºC, which corresponds to around 7.6 wt% water in succinonitrile. The choice of using this solution was made for two reasons. Firstly, SCN is a "plastic crystal" (Glicksman, Schaefer, & Ayers, 1976), so its high ductility could be used to verify efficeincy of ultrasound in dendrite fragmentation. Second reason is to try to illustrate growth of phases stable at higher temperatures. Since the SCN-water solution has equilibrium monotectic composition at approximately 9.3 wt%, it is expected that the final structure at room temperature consists of the mixture of the solid phase and the water-rich liquid. It was conjectured that the amount of liquid will change after ultrasonification.

Freezing was performed in a simple crystallizer illustrated in Figure 3.1. Five of its walls are made from Plexiglas (1), while the top wall is made from aluminum. The test tube (2) is immersed in the crystallizer through the hole in the top wall. Sealing is provided by using screws (3) and plate (4) to press the test tube against O-rings (5). In the test tube with liquid are immersed sonotrode (6) and/or thermocouples. Screws (3) also served for axial alignment of the test tube with vertically positioned sonotrode. Circulation of the heat transfer fluid was achieved by connecting inlet (7) and outlet (8) ports with the circulator Thermo Haake DC 10.

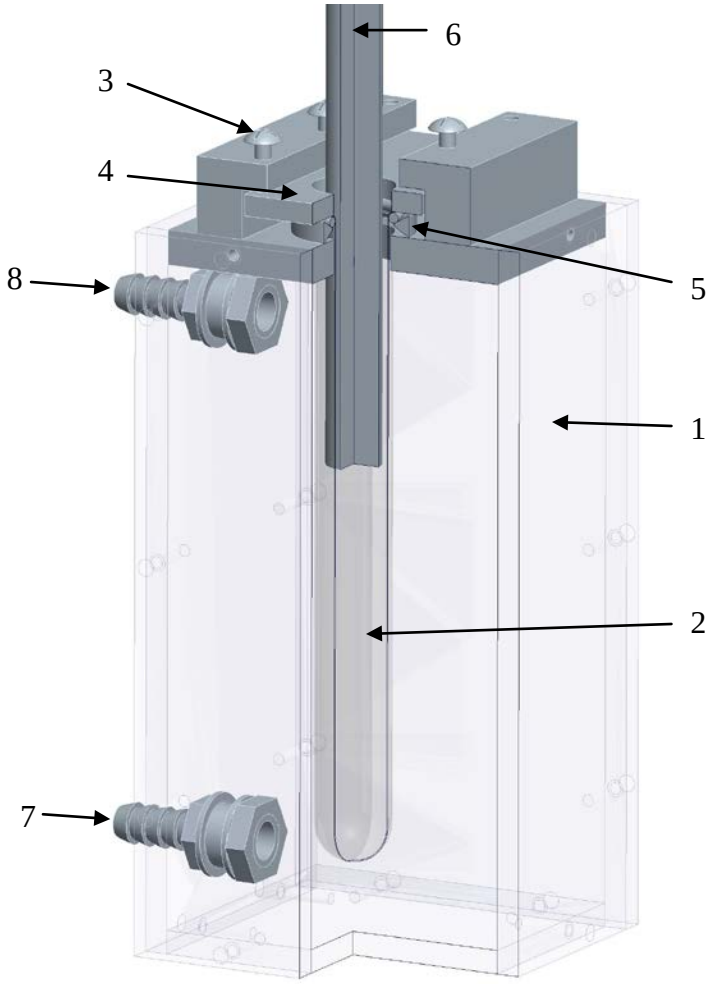

Figure 3.1. Sketch of the crystallizer used in experiments, where (1) are Plexiglas walls, (2) test tube, (3) screws, (4) fixing plate, (5) rubber O-rings, (6) sonotrode, (7) inlet, (8) outlet.

The temperature of the heat transfer fluid is controlled with the combination of the thermal bath Thermo Haake K 15 and the circulator Thermo Haake DC 10 (Figure 3.2). Operating range of this combination is from -20 °C to +100 °C. Without the crystallizer connected to the circulator, the temperature variation is kept within ±0.1 °C throughout the bath.

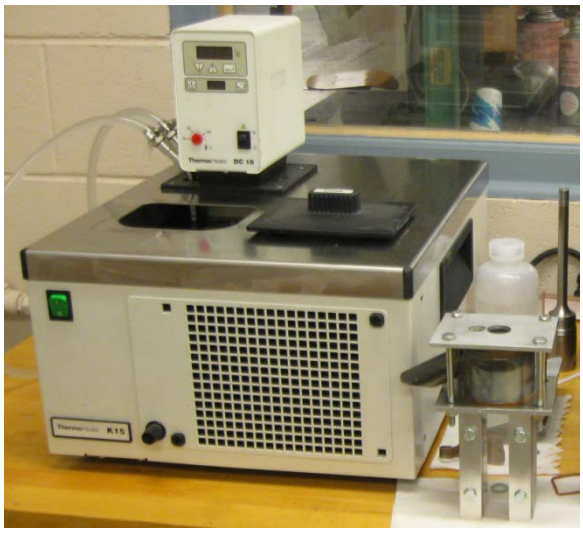

Figure 3.2. Thermal bath Thermo Haake K15 with circulator Thermo Haake DC 10.

The heat transfer fluid used was Dynalene HC-50 (Dynalene, Inc., Whitehill, PA). This is a transparent, aqueous-based liquid which operates in the temperature range from -50 °C (-58 °F) to 218 °C (428 °F). Its boiling point is 118 °C (244 °F).

A combination of the wave generator and RF amplifier, shown in Figure 3.3, was used to provide input signal to the ultrasonic transducer. The wave generator is capable of creating various types of signals, from sine to square, step, continuous and intermittent signals. The maximal power of the RF amplifier is 150 W, and the frequency range from 10 kHz to 100 MHz.

Electric signal was converted to mechanical vibrations in piezoelectric transducer (converter) Sonics CV154 (Sonics & Materials, Inc, Newtown, CT). Its nominal oscillating frequency is 20 ±0.5 kHz. Its resonant frequency was experimentally verified by observing cavitation in water. Cavitation was observed when the converter was driven

with frequencies in the range between 19.07 and 20.12 kHz. Cavitation was the strongest for frequencies 19.63 to 19.69 kHz.

Figure 3.3. Agilent 33120A function/arbitrary waveform generator (top), and RF amplifier Applier Research 150A100B (down).

Three types of sonotrodes were used, all made from Ti6Al4V:

1. Commercial sonotrode S&M 1102 (Sonics & Materials, Inc., Newtown, CT). This is an exponential sonotrode, which means that the transition between the larger diameter, 1.5” (38.1 mm), and smaller diameter, 1/2” (12.7 mm), follows the exponential rule. It was mounted directly on the transducer. This sonotrode was used in initial experimental stages, to allow large enough gap between test tube walls, so thin thermocouple wires could be placed in the liquid for in situ temperature recording. The resonant frequency of the sonotrode and transducer in a stack is 23.28 kHz, and this frequency was used in experiments.
2. The “acoustic streaming sonotrode”, or shortly the AS sonotrode, with main dimensions shown Figure 3.4, was designed to produce mainly acoustic streaming in the liquid, and diminish effects of radiation pressure.
3. The “radiation pressure sonotrode”, or shortly the RP sonotrode, with main dimensions of which is shown in Figure 3.5. It was designed so its radius is around

0.4 mm smaller than the inner diameter of the test tube. This design was intended to maximize effects of radiation pressure and minimize acoustic streaming. The difference in dimensions of the sonotrode and test tube was chosen for practical reasons, firstly to allow elimination of entrapped gas, and to prevent contact of the sonotrode with the test tube. With smaller gap, it is hard to remove entrapped air. Entrapped air could not be removed below this sonotrode when succinonitrile was used.

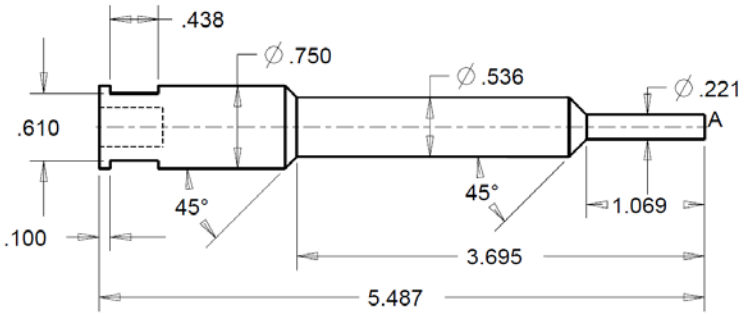

Figure 3.4. Main dimensions (in inches) of the "acoustic streaming sonotrode", designed to produce mainly acoustic streaming in the liquid. Sketch is not to scale.

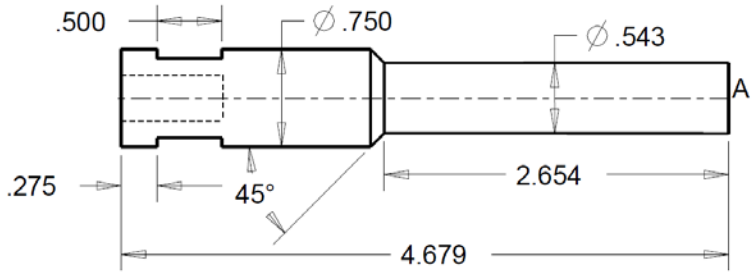

Figure 3.5. Main dimensions (in inches) of the "radiation pressure sonotrode", designed to produce mainly radiation pressure in the liquid. Sketch is not to scale.

As discussed in Sections 2.2.2 and 2.2.3, radiation pressure is maximal and acoustic streaming theoretically absent if the liquid volume is closed with the oscillating piston; also, acoustic streaming is predominant if the diameter of the sound beam is

smaller than the diameter of the container. The two sonotrodes were made based on this consideration.

In case of both AS and RP sonotrodes, the ultrasonic stack consisted of the transducer, adaptor Sonics Vibra-cell 630-0207 (Sonics & Materials, Inc., Newtown, CT), and the sonotrode. The adaptor was used to bridge the difference in diameters between the transducer (1.5”) and the sonotrode (3/4”).

The AS and RP sonotrodes were designed to meet two requirements, 1) that the whole stack has resonant frequency of exactly 20 kHz, and 2) that the sonotrode oscillates longitudinally at that frequency.[17]

The main assumption here was that the converter and the adaptor together have longitudinal oscillations, and if one adds a sonotrode with longitudinal oscillations at appropriate lower frequency, the whole stack will resonate longitudinally when driven at 20 kHz. That proved in practice. The resulting geometries are shown in Figure 3.4 and Figure 3.5, while corresponding resonant frequencies 12517 Hz (Figure 3.6) and 12041 Hz (Figure 3.7). The ultrasonic stack with the acoustic streaming sonotrode oscillated at exactly 20,000 Hz, while with the radiation pressure oscillated at 20,000 to 20,030 Hz, the latter frequency giving better results in most cases.

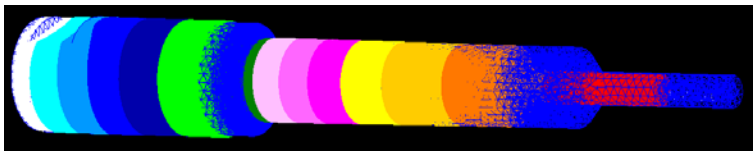

Figure 3.6. The shape mode of the 8th harmonic, with the frequency 12517 Hz, for the sonotrode shown in Figure 3.4.

[17] Longitudinal oscillations are beneficial for several reasons. First, all theoretical calculations assume this kind of motion. Secondly, lateral oscillations can cause mechanical problems to sonotrodes with small tips or larger reductions of the diameter. In one instance, a sonotrode with just one step, from Ø0.75” to Ø0.25”, cracked after about one minute of transversal oscillations at higher power inputs.

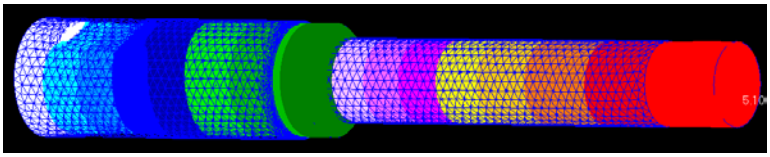

Figure 3.7. The shape mode of the 8th harmonic, with the frequency of 12041 Hz, for the sonotrode shown in Figure 3.5.

Two types of test tubes were used, Pyrex with around ID 0.61" (15.494 mm) and OD 0.699" (17.755 mm), and Kimax with around 0.558" (14.173 mm) ID and 0.638" (16.205 mm) OD. Kimax test tubes were used with AS and RP sonotrodes, while Pyrex was used in experiments when the S&M 1102 sonotrode and thermocouples were used.

All thermocouples used were T type (copper-constantan), which provides highest accuracy around 0 ºC (32 ºF).

1. Miniature needle probe, model 117-181, with the accuracy 0.2 ºC, time constant less than 1 s in liquids, and less than 5 s for full reading. This thermocouple was used to measure temperature inside the cooling bath.
2. Surface probe, model MT-D, with the accuracy 0.1 ºC, the time constant 0.025 s in liquid, and 0.125 s full reading. Temperature reading is more accurate if as much of the thermocouple length is oriented along the isotherm, minimizing the error caused by heat conduction along the thermocouple leads (Singh & Dybbs, 1976; Satyamurthu, Marwah, Venkatramani, & Rohatgi, 1979). For that reason, this type of thermocouple with curved tip (Figure 3.8) was chosen to provide greater accuracy of the temperature measurement in the test tube, especially near the liquid surface.
3. Tissue implantable thermocouple, model IT-1E, with the accuracy 0.1 ºC, time constant 0.005 s in liquid, and 0.025 s full reading. These thermocouples were chosen because of their small diameter (0.0025" or 0.64 mm), so they can be immersed in the liquid with the S&M 1102 sonotrode.

The needle thermocouple was used to measure temperature inside the cooling bath and compare it with the temperature reading on the circulator's display. The other two models were used to measure temperature inside the test tube.

National Instruments FieldPoint data acquisition system was used for temperature measurements, with the eight-channel thermocouple module FP TC-120 and the network interface module FP-1000. The user interface and data acquisition were programmed in LabVIEW (National Instruments Corporation, Austin, TX). Although thermocouples have very small time constant, 0.88 Hz update rate of FP TC-120 module (National Instruments, 2012) is a bottleneck in the rate of data collection, leading to choppy appearance of temperature curves. Recorded data sometimes shows changes in temperature faster than every 1.136 s, which would correspond to the update rate.

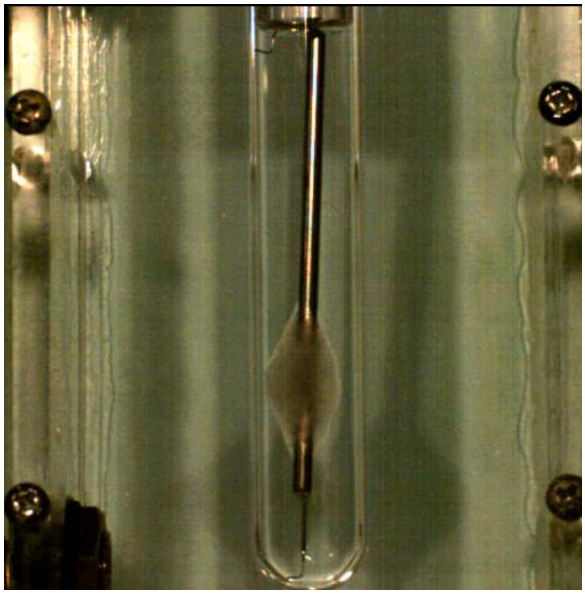

Figure 3.8. A test tube with two MT-D thermocouples for measurement of surface temperature, one immersed to the bottom of the test tube, and the other with only tip immersed near the surface. Initial nucleation occurred at the thermocouple.

Solidification in crystallizers was recorded with the high-speed camera Photron FASTCAM-ultima 1024 (Photron Ltd., Japan). Recording speed was either 500 or 1000 frames per second.

The whole setup is shown in Figure 3.9. Vertical position of the sonotrode was provided by leveling the frame on which it was positioned. Axial alignment of the test tube and the sonotrode was achieved by adjusting screws shown in Figure 3.1.

The greatest problem with the experiment was to adjust lights and obtain acceptable image quality. The best results, although still not satisfactory, were obtained with the setup in Figure 3.9. Two light sources were located at the same side as the camera in a way that minimizes shadows and glare from other objects. A screen covered with blue paper served to diffuse and reflect light to the camera.

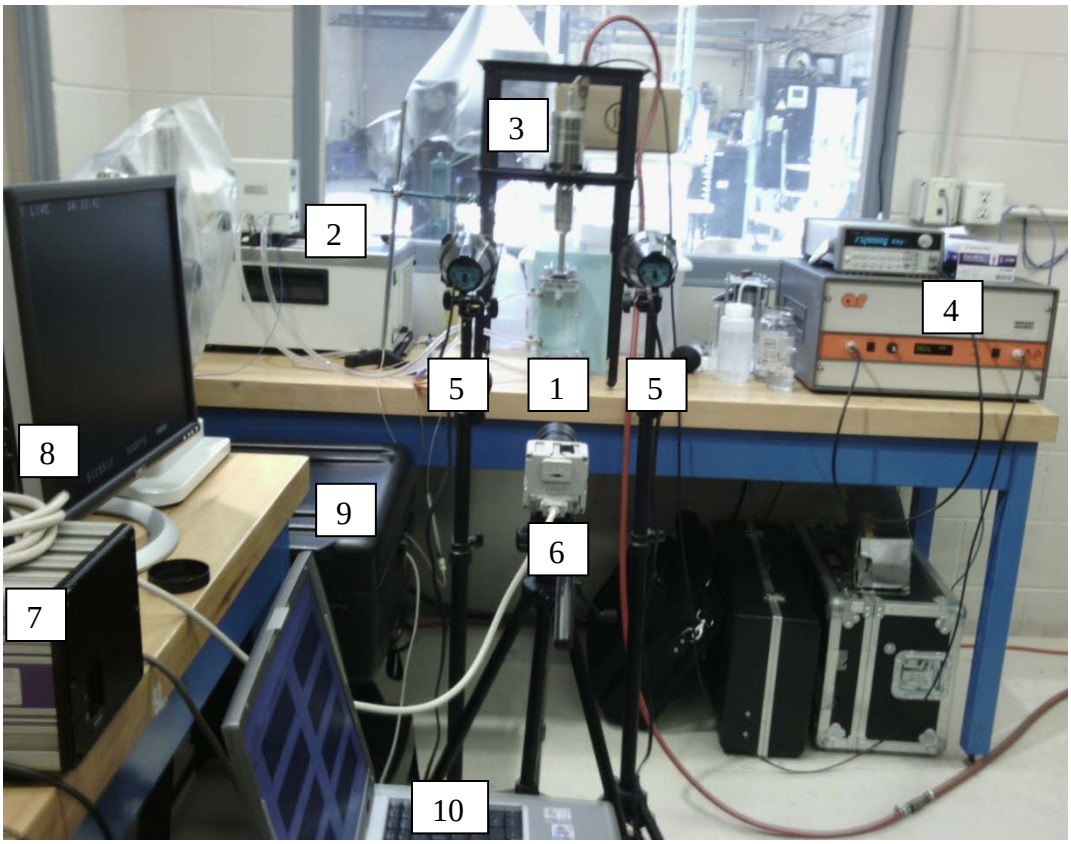

Figure 3.9. A complete experimental setup consisting of the (1) crystallizer with screen; (2) thermal bath with crystallizer; (3) ultrasonic stack, in this case transducer and S&M 1102 sonotrode, positioned on the frame; (4) wave generator with RF amplifier; (5) two 600 W lights; (6) high-speed camera; (7) processor of the high-speed camera; (8) monitor; (9) data acquisition system; (10) computer.

3.2. Types of Experiments Performed

Several groups of experiments were performed:

1. Thermal (spontaneous) solidification, without applied ultrasound. These experiments were aimed to determine the supercooling needed for nucleation, as well as calibration purposes. Temperature inside the test tube was measured with surface thermocouples placed near the bottom and near the free surface of the liquid. Accuracy of small-diameter thermocouples was tested by placing their tip near the tip of the surface thermocouple, as illustrated in Figure 3.10a. Temperature of the thermal bath was measured in the same time with the needle thermocouple. These measurements were used later to estimate the temperature in the liquid based on the temperature measured inside the thermal bath.
2. Solidification triggered by ultrasound, with or without temperature measured by small-diameter thermocouples immersed in the liquid. Thermocouples were used to measure the temperature in the liquid before ultrasound was started and during solidification. Measurements below immersed sonotrode and at the bottom of the test tube showed the influence of the sonotrode on the temperature field in the liquid. In some experiments, in order to minimize disturbance of the sound field but still get temperature readings, only one thermocouple was placed below the sonotrode, as shown in Figure 3.10b. Only S&M 1102 sonotrode and water were used in these experiments. Thermal bath was set to three temperatures: -2, -5, and -10 ºC. This group of experiments was performed in two ways:
   a) Water was cooled first without the sonotrode, with surface probes (MT-D) measuring temperature at the bottom and near the water surface. In all experiments one small-diameter thermocouple was placed near the water surface, and in some experiments another IT-1E was also added near the bottom of the test tube. After the whole system without the sonotrode had reached and spent certain time at desired temperature, MT-D thermocouples were pulled out leaving small-diameter thermocouple(s) in, and the sonotrode was set in place. In most of experiments ultrasound was started after temperature readings had stabilized. In a

few experiments ultrasound was started while readings showed temperature above 0 ºC near the water surface.

b) The sonotrode was immersed in water and cooled together. All three liquids (water, ammonium chloride, and succinonitrile) were used in these experiments. In some experiments one small-diameter thermocouple was always placed below the sonotrode, and sometimes another was added near the bottom of the test tube.

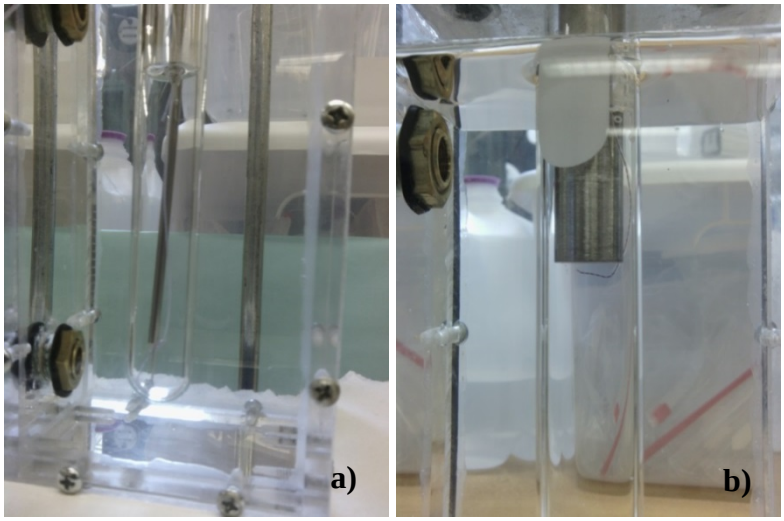

Figure 3.10. (a) Surface and small-diameter thermocouples in the test tube filled with water. Around the test tube circulates heat transfer liquid.
(b)S&M 1102 sonotrode with the tip of the small-diameter thermocouple placed beneath.

3. Fragmentation of dendrites by bubbles. In these experiments, bubbles were let to be entrapped below the sonotrode tip. After thermal (spontaneous) nucleation, ultrasound was started while dendrites still grow. Ultrasonic field was set to be slightly below cavitation threshold, but strong enough to propel the bubble downwards and also cause pulsations of the bubble. Only aqueous solution of ammonium chloride was used, since ice grows in water at too fast rate to allow timely start of ultrasound.
4. Influence of radiation pressure and acoustic streaming on the fragmentation of dendrites. RP and S&M 1102 sonotrodes were used in these experiments. This group

of experiments served to verify conjecture whether radiation pressure may contribute to dendrite fragmentation, and to what extent.

Table 3.1 summarizes the most frequently used experimental conditions:

- Parameters of applied ultrasound: frequency, f, and amplitude, A, of the pre-amplified input signal; shape of the signal was sinusoidal in all experiments; power of amplified signal, P, was set to 120 W in all cases (80% of maximal 150 W). As already mentioned, frequency was dictated by the resonant frequency of the ultrasonic stack. Amplitude was chosen so the sonotrode creates pressure that is above the cavitation threshold (see Section 4.1).
- Volume of treated liquid was 15 mL. In a few experiments on thermal nucleation 20 mL of water was used.

Table 3.1. *Parameters that are usually used in experiments.*

Supercooling [ºC]	f [kHz]	A [mVpp]	signal	P [W]	Duration of continuous signal [s]	Pulsed signal	
						Frequency [Hz]	Duty [%]
< 2	23.28[a]	300[d] 600[e]	sine	120	0.1, 0.2, 0.5, 1, 2	5, 10	5, 25, 50
4-5	20.00[b]						
9-10	20.03[c]						

[a] For ultrasonic stack with S&M 1120 sonotrode.
[b] For ultrasonic stack with “acoustic streaming” sonotrode.
[c] For ultrasonic stack with “radiation pressure” sonotrode.
[d] Purified water, succinonitrile.
[e] Aqueous solution of ammonium chloride, 4.5 wt%.

Given above is just a review of parameters common to all experiments. For experimental results given in the next chapter, additional experimental details will be given where needed.

CHAPTER 4. OVERVIEW OF EXPERIMENTAL RESULTS

This section gives an overview of selected results which will serve to support discussion in the following chapter.

4.1. Threshold of "Effective Cavitation"

A term "effective cavitation" was coined to describe cavitation capable of nucleating a solid phase at small supercooling. Frequency and power were kept fixed as per Table 3.1, while the amplitude of pre-amplified signal, A, was varied. This cavitation threshold was determined by visual inspection in the liquid, based on two arbitrarily declared conditions. The first criterion for determining the "effective cavitation threshold" was to always be able to observe cavitation in a 100 mL volume of the liquid at room temperature. The second condition was to practically always nucleate a solid phase in previously not degassed liquid by ultrasonication that lasts 0.1 second at small supercooling (1 to 2 ºC). The so created solid phase should become visible during ultrasonication or shortly after. The interval of amplitudes was called a transition interval if the second condition could not be always satisfied.

Cavitation thresholds determined in this way are very arbitrary, first because its definition is arbitrary and then because large variations in the second requirement, nucleation at small supercooling, were experienced. The differences are most likely due to different initial conditions of the liquid, mostly the level of aeration. For example, in one occasion ice could be spotted in water at amplitude 200 mVpp.[18] However, in two

[18] Vpp is the unit which reads "Volt peak to peak". It is the voltage measured from the maximum negative to the maximum positive value of the wave, which is sinusoidal in

other experiments ice could not be nucleated even at 600 mVpp and 900 mVpp, after water had been previously ultrasonicated with 600 mVpp at +2 ºC for around one minute.

For purified water, the "effective cavitation" threshold was decided to be 300 mVpp, while the transition interval was determined to be between 260 and 300 mVpp. At lower amplitudes ice could barely be noticed, and only in some runs. When the amplitude was increased from values below 100 mVpp, observable cavitation started at $A = 150 - 160\,\mathrm{mVpp}$. On the other hand, if ultrasonication was started at 300 mVpp, cavitation could be sustained when the amplitude was decreased down to levels somewhat below 150 mVpp.

In a 100 mL of succinonitrile with 5 wt% water solution, a weak cavitation could be started at 200 mVpp, but it ceased quickly. Strong, but not sustained cavitation appeared with 250 mVpp of amplitude. With 300 mVpp, a stable cavitation was produced. Precipitation of solid phase was greatly enhanced with the same amplitude of pre-amplified signal. It was decided that the threshold of "effective cavitation" in succinonitrile is 300 mVpp, with no transition interval.

"Effective cavitation" thresholds in aqueous solutions of ammonium chloride (4.5 and 25 wt%) were much harder to determine. In a 100 mL volume, sustained cavitation was observed at 200 mVpp amplitude, but the solid phase was formed with relatively large delay. As shown later in Figure 4.15, only few flakes formed in the 4.5 wt% solution 6 seconds after ultrasound with 600 mVpp had been applied for 0.1 second. Significant amount was formed with continually applied bursts (Figure 4.17). It is interesting that, after initial precipitates spontaneously formed at supercoolings up to about 2.5 ºC in the 25 wt% solution, no new visible precipitates formed by ultrasonication. However, significant number of new precipitates formed when supercooling was around 4.5 ºC, but with a long delay. Following the two previous examples, 600 mVpp was determined as the amplitude which nucleates solid phase in ammonium chloride.

---

our case. If the wave is symmetric around the zero value, Vpp is twice the voltage amplitude.

4.2. Thermal Nucleation (without Ultrasound)

In our experiments, freezing temperature depended slightly on the number of thermocouples immersed in the water, although they were thoroughly cleaned before each use. With two surface probes immersed, the temperature at which freezing occurred varied from -11.043 to -14.125 ºC at the bottom, and from -10.7 to -13.938 ºC near free surface of the liquid. The maximal temperature difference in the liquid column was 0.343 ºC, and the minimal was 0.063 ºC. A typical example of cooling curves is shown in Figure 4.1. With one thermocouple immersed, measured temperature when ice formed was somewhat lower, -15.4 ºC, Figure 4.2. Freezing of this sample is shown in Figure 4.3. 15 mL of purified water was used in all experiments. In most cases the volume froze within 0.34 to 0.44 seconds, depending on the location of the nucleation site. The two times measured outside this range were 0.568 and 0.656 seconds.

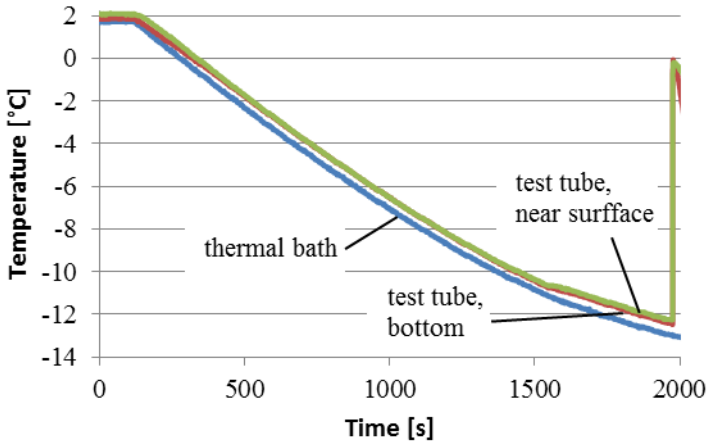

Figure 4.1. Cooling curves for purified water. Setup for this experimental run is shown in Figure 3.8. Measured temperature just before recalescence was -12.475 ºC at the bottom of the test tube and -12.257 ºC near the water surface.

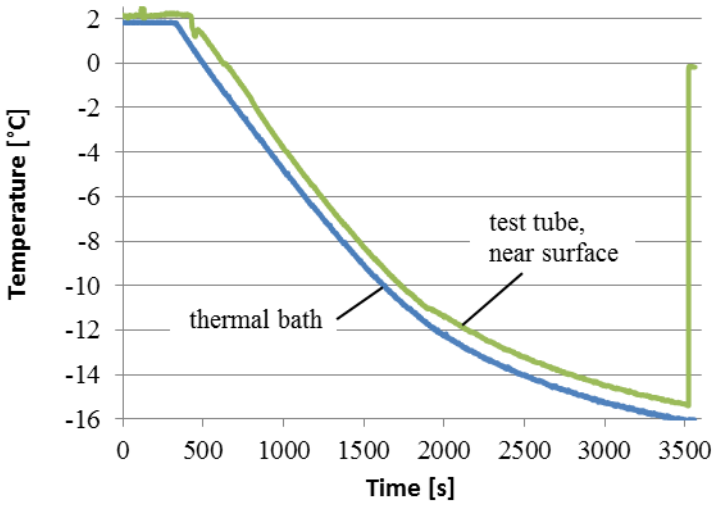

Figure 4.2. Cooling curve with one thermocouple immersed close to the free surface. Measured temperature before recalescence was -15.401 ºC. Temperature inside the thermal bath was 0.716 ºC lower.

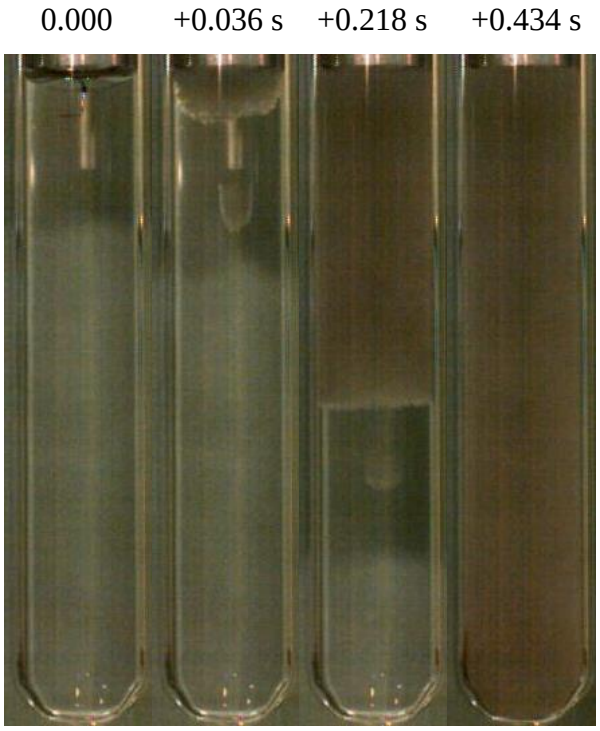

Figure 4.3. Some sequences of spontaneous freezing of the sample with the cooling curve shown in Figure 4.2. The first frame from left is the moment when ice nucleated at the contact between the thermocouple and water surface. Time elapsed after that moment is given above each frame.

Although the heat transfer fluid circulated through relatively long plastic tubes between the thermal bath and the crystallizer (Figure 3.9), the maximal temperature differences between the thermal bath and water in the test tube was 0.872 ºC (measured near the surface of the water column in the test tube) and 0.529 ºC (measured at the bottom of the test tube).

With two thermocouples immersed, nucleation occurred mostly at the wall of the thermocouple immersed down to the bottom of the test tube, interestingly never in the bottom 1/4 of the water column where the temperature was lowest. Figure 3.8 shows about the lowest point where ice was observed. With one thermocouple immersed, nucleation usually started at the thermocouple, near the surface of the water column. In the experimental run which temperature measurement is shown in Figure 4.2, nucleation started at the water surface in the cusp formed by surface tension between water, thermocouple wall, and air. Without thermocouples, ice nucleated at the walls of the test tube, and was not observed in the lower part of the test tube.

A cooling curve obtained for the solution of 4.5 wt% ammonium chloride in water is shown in Figure 4.4. Variation of measured temperature at freezing was smaller than for water, and it was between -9.2 and -9.4 ºC. Temperature measured at recalescence was between -3.79 and -3.759 ºC. Melting temperature of this solution should be between -3.65 and -3.51 ºC, as mentioned in Section 3.1. As with water, nucleation most frequently occurred at the thermocouple. Without immersed thermocouple, the solution nucleated also at the test tube walls, and never in the lower part of the test tube.

In previous examples recalescence was very pronounced, increasing temperature of the sample up to the melting (saturation) temperature. In the solution of 5 wt% (or 7.5 wt%) water in succinonitrile (SCN) almost no recalescence could be observed (Figure 4.5). Even if some increase in temperature happened, it was when some amount of precipitates has already been formed around the thermocouple. The same was observed with the hypereutectic solution of ammonium chloride, not reported in this work.

It was observed that, given enough time, some amount of precipitates will form at no supercooling. Melting of the large portion of the SCN-water solution was observed around +25 ºC, while precipitation occurred at approximately the same temperature. One

of example is shown in Figure 4.6, when the temperature difference between melting and precipitation was 0.5 °C. This behavior is obviously due to the effects of segregation and impurities.

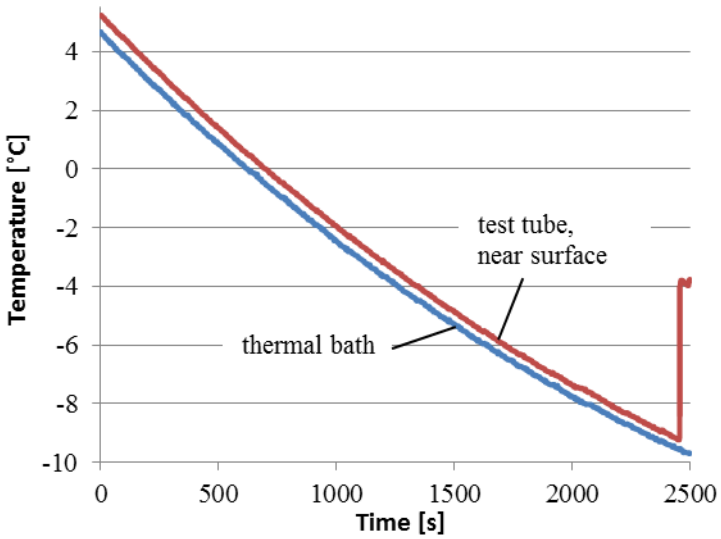

Figure 4.4. Cooling curve for 4.5 wt% aqueous solution of ammonium chloride. At freezing, temperature 23 mm below the surface of solution is -9.237 ºC, and at recalescence -3.79 ºC.

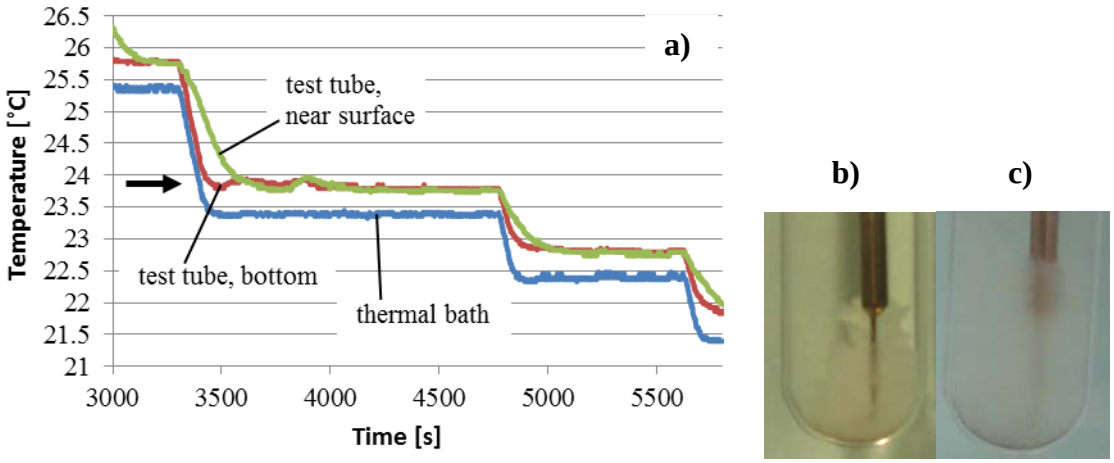

Figure 4.5. Temperature measured during stepwise cooling from 40 °C. Precipitation started during cooling to approximately 24 °C (marked with arrow). Images b) and c) were taken 14 minutes apart during holding at temperature marked with arrow, illustrating very slow growth rate.

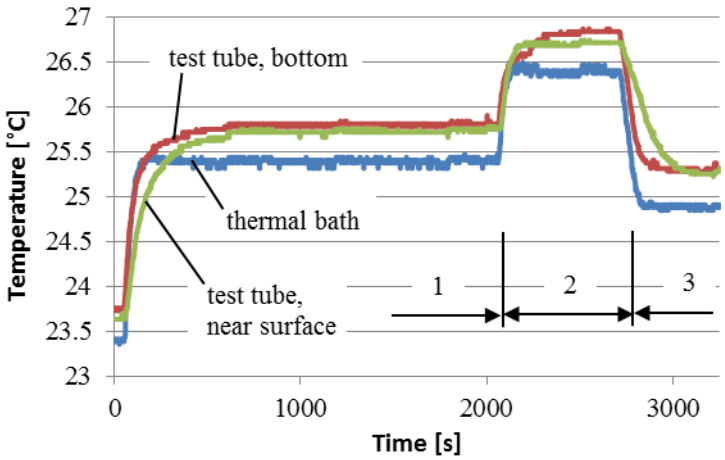

Figure 4.6. Measured temperature in the SCN-water solution. At the beginning the sample was completely solidified, then in stage "1" majority of the sample melted, and completely melted as soon as stage "2" is reached. Precipitation started at the onset of stage "3".

4.3. Nucleation Triggered by Ultrasound

4.3.1. Supercooling Smaller Than 2 ºC

Figure 4.7 and Figure 4.8 illustrate experimental procedure 2a described in Section 3.2.

As can be concluded from these two figures, temperature was monitored with three thermocouples for the first 2600 seconds. After that, two MT-D thermocouples were taken out and at around 2750 s the sonotrode was inserted. First peak in Figure 4.8 at around 2750 s is a response to warmer sonotrode that was just inserted. The second temperature peak of around +0.44 ºC appeared around the moment when ultrasound was started. The peak lasted for 0.8 seconds, which is in excellent agreement with the duration of ultrasonic pulse (1 second), especially taking into account that the data acquisition system updates measurements every 1.136 seconds.

As shown in Figure 4.9, results were not much different when the sonotrode is cooled together with water in the test tube. The only differences are that the cooling rate is a little slower and temperature below the sonotrode does not oscillate as much during

holding at constant temperature. However, measurements show recalescence up to the same level, this time +0.35 ºC. The peak lasted for 2.1 second, again closely matching duration of ultrasonification.

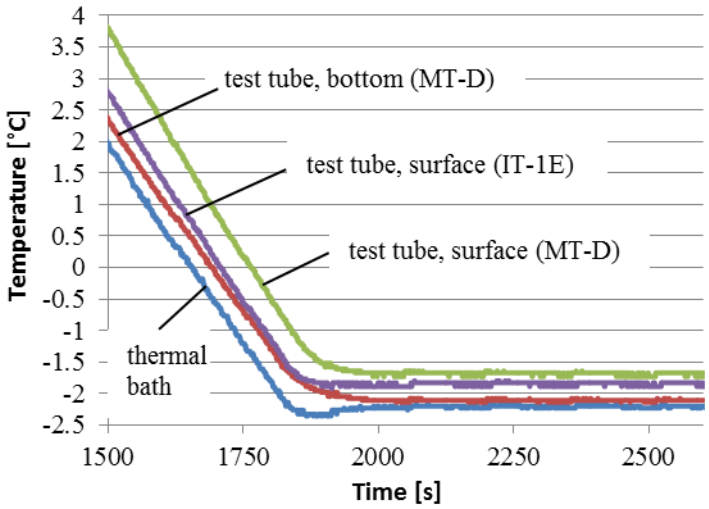

Figure 4.7. Cooling curves for purified water, where MT-D denoted the surface probe and IT-1E is the small-diameter thermocouple (see Section 3.1 for description). Initial temperature in the cooling bath was 23.45 ºC.

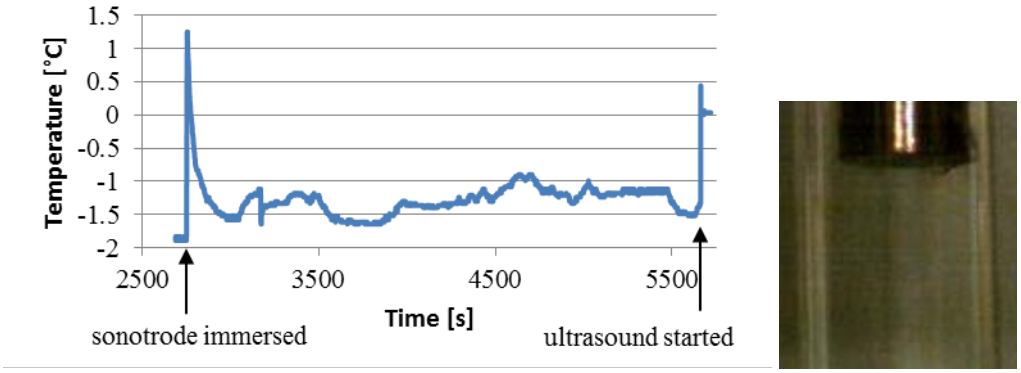

Figure 4.8. Left: Temperature measured below the sonotrode after it was inserted. Ultrasound: $A = 300\,\text{mVPP}$, duration 1 second. Right: Small-diameter thermocouple IT-1E, captured at the moment of the onset of cavitation.

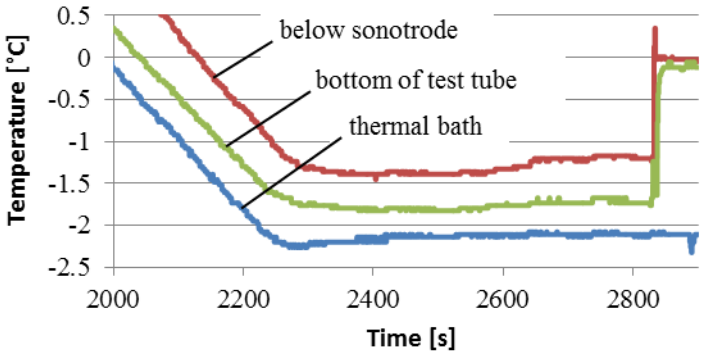

Figure 4.9. Cooling curves for purified water when the sonotrode is immersed in the water at room temperature and cooled together. Temperatures in the test tube were measured only with the small-diameter thermocouples. Initial temperature in the thermal bath was +22.3 ºC. Ultrasound: $A = 300\,\text{mVPP}$, duration 2 seconds.

Figure 4.10 shows temperature measurements during the experimental run when the sonotrode was immersed in already cooled water, as in the run shown in Figure 4.7 and Figure 4.8. The important difference here is much higher temperature jump after the sonotrode was immersed in the water. The first, smaller peak is comparable to that in Figure 4.8, but the peaks that follow are much higher. Before ultrasound was started, measured temeprature below the sonotrode oscillated between +0.07 and +0.132 ºC. After ultrasound had started, which lasted for 1 second, measured temperature dropped to -0.21 ºC for exactly 1 second. This example is presented here mainly for the purpose of discussion in the next chapter on the possibility of nucleation at temperatures above melting point.

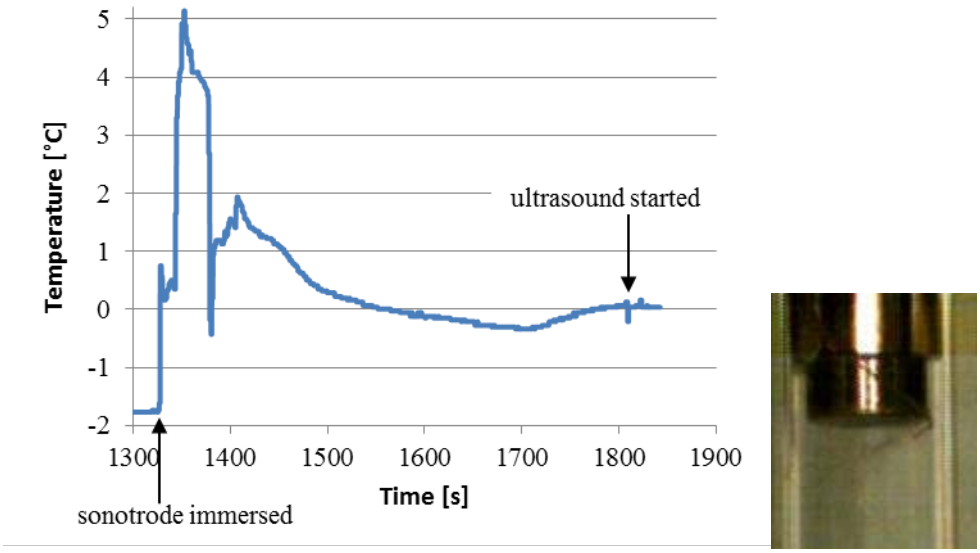

Figure 4.10. Left: Temperature measured below the sonotrode after it was inserted. Ultrasound: $A = 300\,\text{mVpp}$, duration 1 second. Initial temperature in the thermal bath was around +9.35 ºC. Right: Small-diameter thermocouple IT-1E, captured at the moment of the onset of cavitation.

As long as the temeprature field was stabilized before ultrasonification, results were independent on the cooling conditions before the sonotrode was immersed. In the previous example the starting temperature was lower (+9.35 ºC) and holding at final supercooling was shorter (around 300s), so the sonotrode was inserted sooner, around 1328 s after the experiment had started. In another example, starting temperature was close to runs in the first two examples, and holding time at final supercooling was quite significant (Figure 4.11a). Although the temperature below the sonotrode was higher (+0.568 ºC) than in the example in Figure 4.10 (+0.132 ºC), measured temperature was also -0.21 ºC during 1.1 second after ultrasound had started (Figure 4.11b). Again, time of the temeprature change matches excellently duration of ultrasonification.

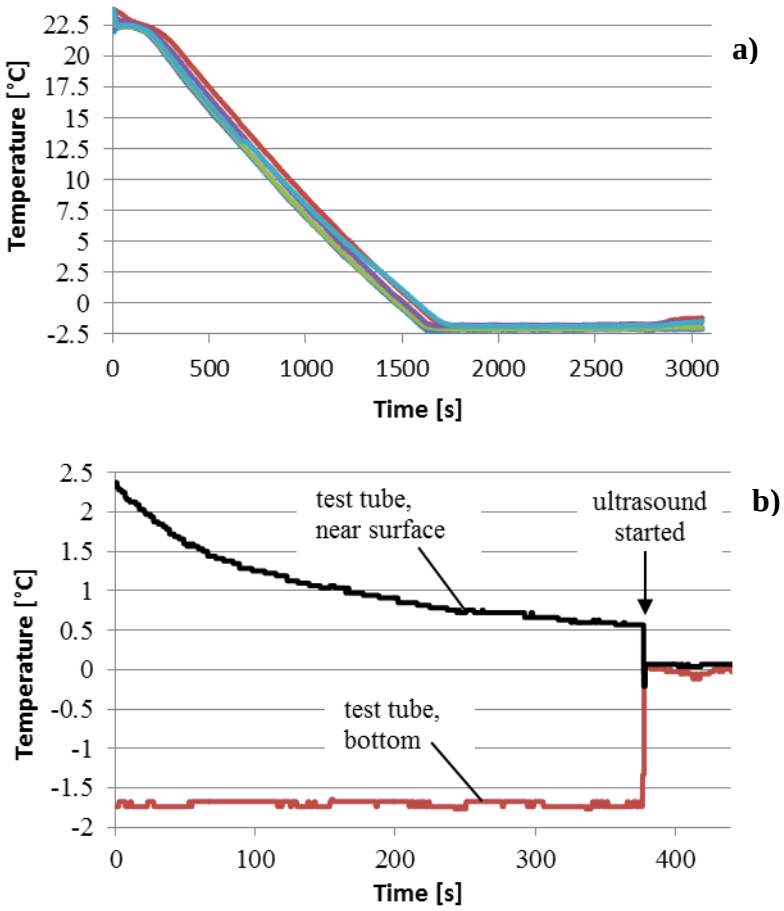

Figure 4.11. (a) Cooling curve for water preconditioning before the sonotrode was inserted. Initial temperature inside the thermal bath was +22.11 °C. (b) Part of the cooling curves after the sonotrode was inserted and at the moment ultrasound was activated for 1 second ($A = 300\,\mathrm{mVpp}$). Note that the abscissa starts from zero; this is because the thermocouple reading was restarted after preconditioning.

A somewhat more control over the temperature below the sonotrode was achieved in the following experiment. In order to eliminate formation of dew at the walls of the crystallizer, a small heater with a fan was used to blow warm air. Air stream was directed towards the sonotrode, while the portion of the thermocouple outside the crystallizer was shielded from the air stream with a sheet of paper. Water in the test tube and the immersed sonotrode were cooled down to around +2 °C and waited until measured

temepratures stabilized. After that the temperature in the thermal bath was set to -2 °C, and waited again for temepratures to stabilize (Figure 4.12a).

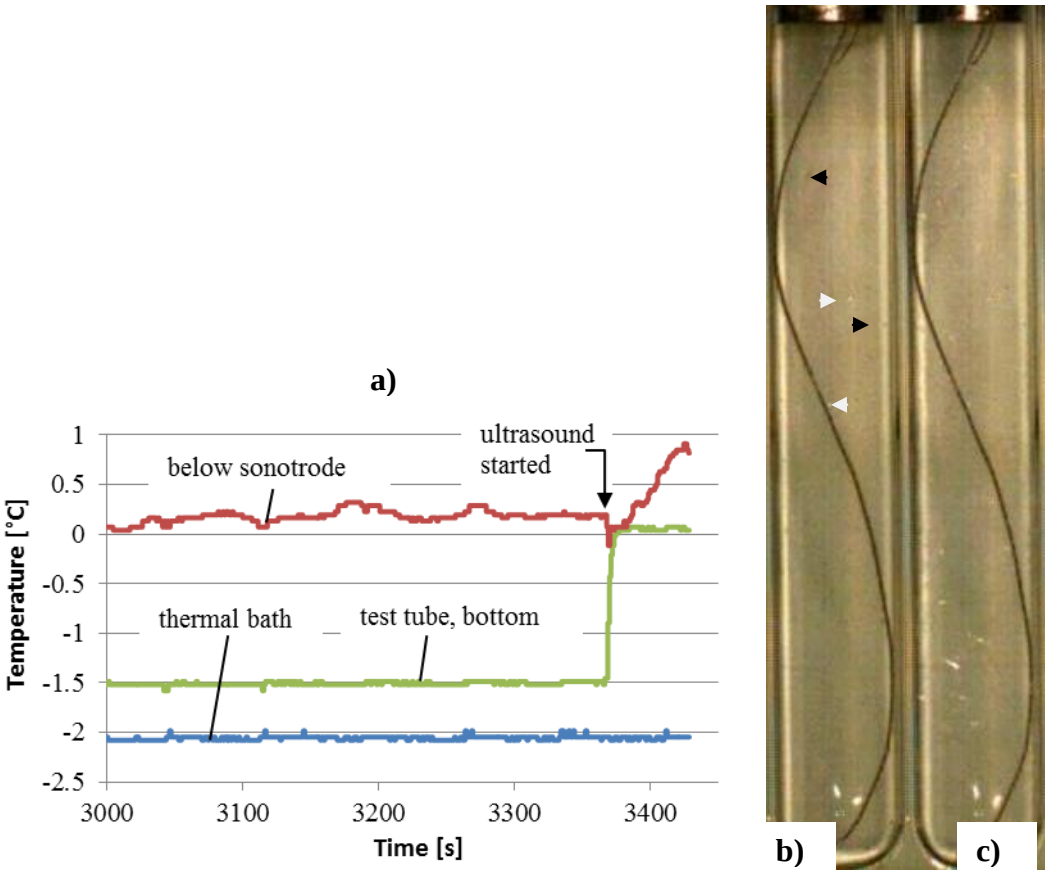

Figure 4.12. (a) Part of cooling curves around the moment when ultrasound was started. The duration of the ultrasound pulse ($A = 300\,\text{mVpp}$) was 0.1 second. (b) A capture 0.067 s after the cavitation onset with visible cavitation cloud. At that moment first crystals (marked with white triangles) were observed. They were created by bubbles (two of them marked with black triangles) hitting the test tube wall. (c) A capture taken 5.73 s after the onset of cavitation, when small crystals are visible in the upper part, and larger crystals floating up from the bottom part of the test tube.

Temperature recording in Figure 4.12a started when temperature in the thermal bath was +1.884 ºC, at the test tube bottom +2.249 ºC, and below the sonotrode +5.019 ºC. Measured temeprature below the sonotrode was +0.195 ºC before ultrasound started, and then dropped to -0.117 ºC for 1.2 seconds before returning back to around zero. The

temperature increase that started some 10 seconds after ultrasound was applied could be attributed to combination of recalescence and heat that comes from the sonotrode.

When the test tube was positioned higher in the crystallizer, the temperature below the sonotrode increased due to larger surface area exposed to the stream of hot air. In the setup shown in Figure 4.13b and Figure 4.13c, the sonotrode tip was postioned around the free surface of the heat transfer fluid. Temperature measured next to the sonotrode was +6 °C, and then the thermocouple was lowered down until measured temperature was slightly around 0 °C. As shown in Figure 4.13b and Figure 4.13c, no significant amount of ice was nucleated by a short pulse (0.1 seconds).

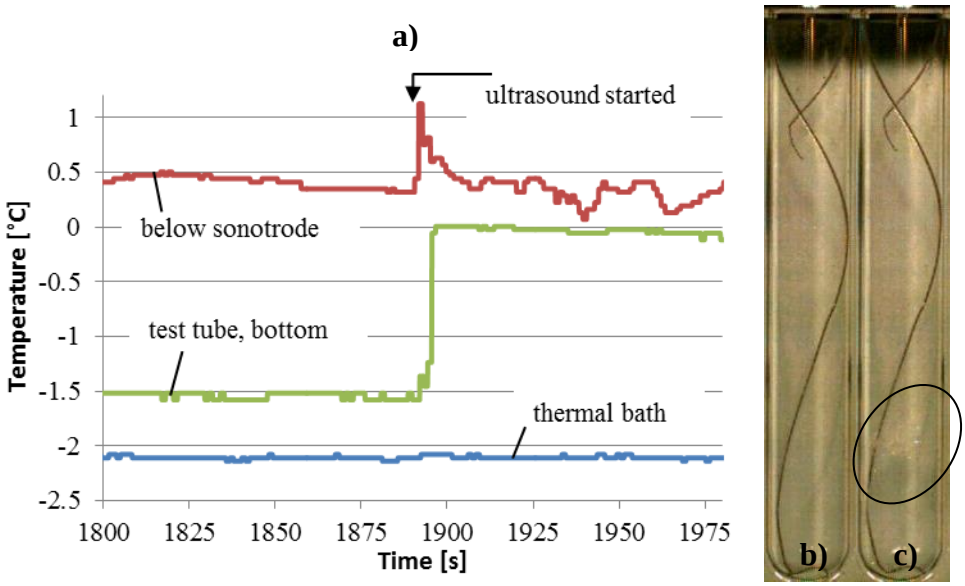

Figure 4.13. (a) Temperature change around the moment when ultrasound was applied ($A = 300\,\text{mVpp}$, duration 0.1 s). (b) A capture 0.1 s after the cavitation onset with visible fringes of the bubble cloud. (c) 5.77 seconds after the cavitation onset the only significant amount of ice, originated at the very bottom of the test tube, is captured as it rises slowly (encircled).

Results of an experiment with a usual setup[19] and short duration of ultrasound (0.2 s) are shown in Figure 4.14. As can be seen, small amount of ice was formed in this experiment. A stronger ultrasonic field, this time with halved duration 0.1 s, created few large crystals in ammonium chloride solution (Figure 4.15).

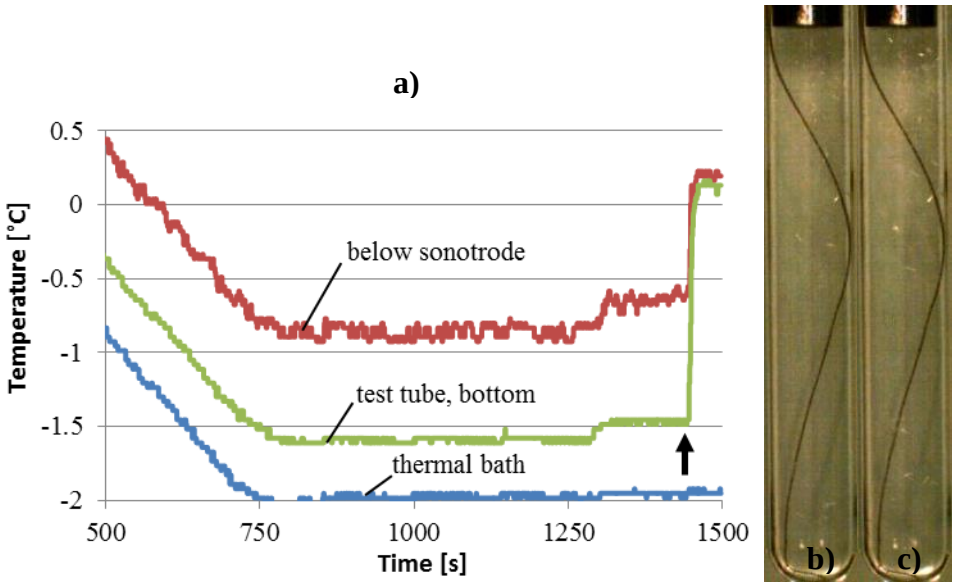

Figure 4.14. (a) Cooling curves with starting temperature in the thermal bath +1.94 ºC. Arrow indicates moment when ultrasound ($A = 300\,\text{mVpp}$, duration 0.2 s) was applied. (b) 4.33 seconds after the onset of cavitation few crystals could be observed, although ice crystals were first observed after around 0.44 s. (c) Situation 5.83 seconds after ultrasound was applied.

Figure 4.15. Solid formed from 4.5 wt% ammonium chloride, 5.88 seconds after the start of ultrasonication with the amplitude $A = 600\,\text{mVpp}$ and duration 0.1 s. The temperature in the bath was set to -5.0 ºC, so estimated supercooling was 1 ºC. The sample had been held around 1 hour at set temperature before ultrasound was applied.

[19] Most frequently, the test tube was inserted in the crystallizer as much as possible, like in Figure 3.1, and the sonotrode was immersed in the test tube from the start of cooling.

Figure 4.16 shows some characteristic sequences of how ice formed at small supercooling if the samples were ultrasonificated for long enough time, but not too long to cause remelting. The time lag between the onset of cavitation and when first ice crystals were large enough to be visible was between 0.155 and 0.46 seconds. After additional period of time the rate at which solid particles form increases. For the experiment in Figure 4.16 a through Figure 4.16 d, ice become visible after 0.35 s, but it seems that more ice become visible between 0.5 and 0.57 seconds after the cavitation onset (Figure 4.16 a and Figure 4.16 b) than during the first 0.15 seconds. After ultrasound stopped (Figure 4.16c and Figure 4.16f), less dense ice floats up and conolidates, and ice coming from the bootom part of the test tube becomes more visible (Figure 4.16d and Figure 4.16f).

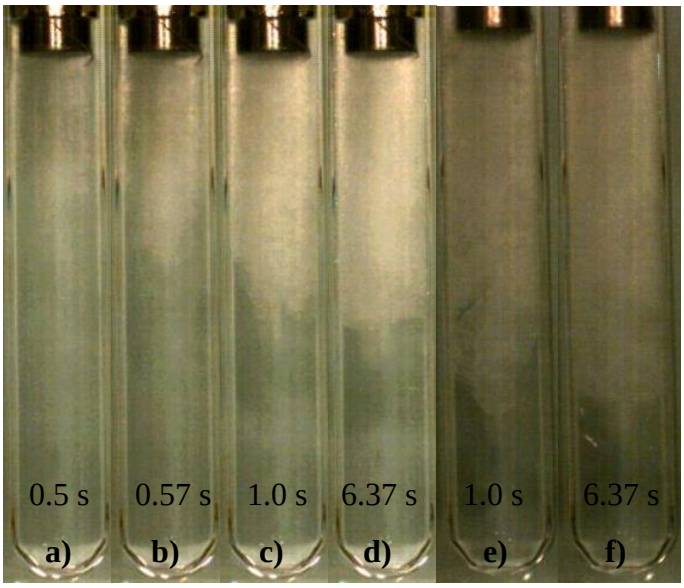

Figure 4.16. Formation of ice in experiments shown in Figure 4.10 [a) through d)], and Figure 4.7 and Figure 4.8 [e) and f)]. Time marked on each frame shows elapsed time after cavitation had commenced. Frames with 1.0 second time show the moment when ultrasound has turned off and cavitation zone will disappear within 2 or 3 thousands of a second.

It is worth noting that in this group of experiments with small supercooling, in case of water and aqueous ammonium chloride solution, the whole volume inside the test tube could not solidify during ultrasonification, whether continuous or intermittent

ultrasound was applied. Figure 4.16d, Figure 4.16f, and Figure 4.17e illustrate how far solid crystallites could reach. Trials to fill the tube with solid particles led to significant remelting and coarsening. An example for water is given in Figure 4.18. With longer duty cycle (Figure 4.18a through Figure 4.18c) a very fine ice was created in the first 20 cysles or so, and then remelting started competing with the formation of ice. As shown in Figure 4.18c, all the ice was almost remelted by the end of 55^{th} cycle. With shorter duty cycle (Figure 4.18d through Figure 4.18f) small amount of ice is being created during each burst with no noticeable remelting.

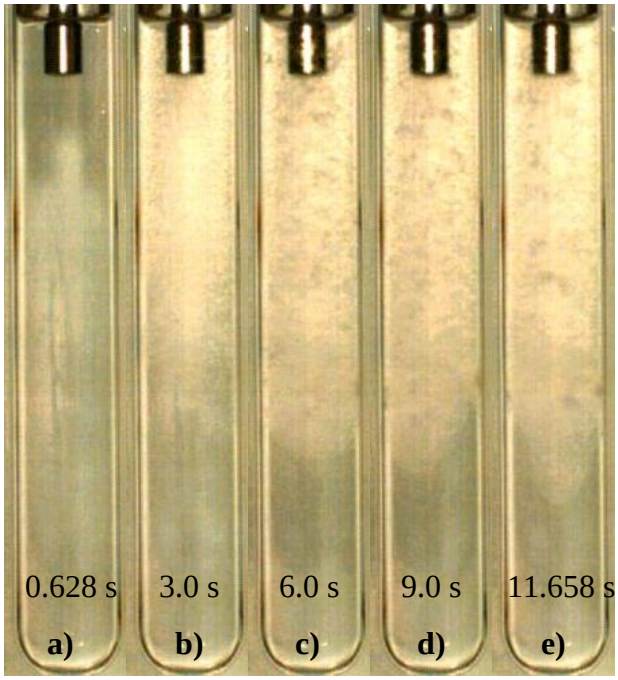

Figure 4.17. High-speed images of freezing of 4.5 wt% aqueous solution of ammonium chloride, with the number of seconds in each frame indicating the time elapsed form the moment when ultrasound started. Thermal bath was set to -5 ºC (supercooling around 1 ºC or more). Ultrasound ($A = 600\,\text{mVpp}$) was applied in bursts, with 5 bursts per second and 50% duty cycle.

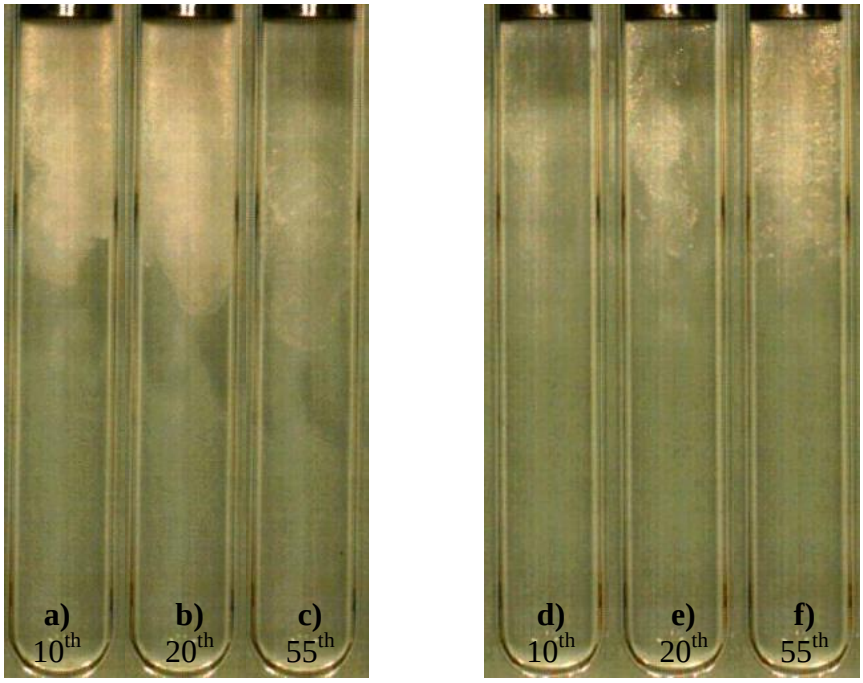

Figure 4.18. Samples of purified water irradiated with ultrasound ($A = 600\,\text{mVpp}$) in bursts with 10 Hz frequency, and the duty cycle of 50% (a-c), and 5% (d-f). Images were taken at the end of 10^{th}, 20^{th} and 55^{th} burst for both samples.

Differently from solidification of water and 4.5 wt% ammonium chloride, succinonitrile was observed to slowly sink down upon solidification, although its relative density is 0.99. That allowed test tube to be completely filled with the solid phase. As shown in Figure 4.19, except some pockets in the lower part, almost the whole test tube was filled with the solid phase.

Excessive ultrasonification has different effect on SCN than on water. As shown in Figure 4.19, solid particles collected at the bottom of the test tube. Although a large portion had been remelted, lack of buoyancy prevented complete remelting like that observed in water (Figure 4.18 a-c).

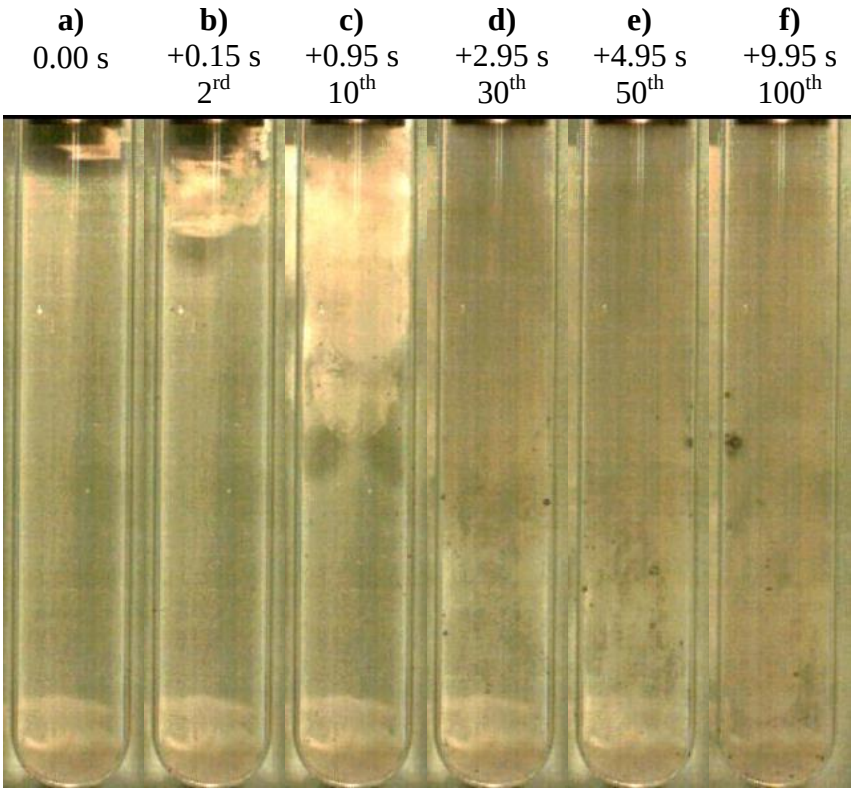

Figure 4.19. A sequence of precipitation in the SCN-water solution during ultrasonication. Above each frame are indicated time elapsed from the onset of the first cavitation burst and the cycle at end of which the image was taken. Ultrasonification was performed in bursts (10 Hz, 50% duty cycle) with $A = 300\,\text{mVpp}$. Temperature of the cooling bath was set to +24.0 ºC, so according to Figure 4.5 starting temperature inside the test tube was around +23.75 ºC. Numerous bubbles are visible in frames d) through f).

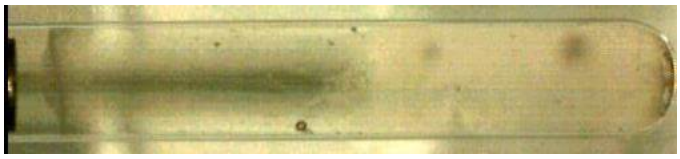

Figure 4.20. A slurry collected in the bottom part of the test tube after approximately 11.4 seconds of ultrasonication with continuous sinusoidal signal of the amplitude $A = 600\,\text{mVpp}$. Initial temperature of the SCN-water solution was around 23.5 to 24 ºC. Many bubbles are visible in the test tube, as well as cavitation cloud below the sonotrode.

The effect of the type of axial ascillatory motion the sonotrode was checked by visualy comparing the amount of ice produced in purified water when the sonotrode was driven with two waveforms of the input signal, sinusoidal and square. Judging by Figure 4.21, it seems that there is no significant difference between the two waveforms.

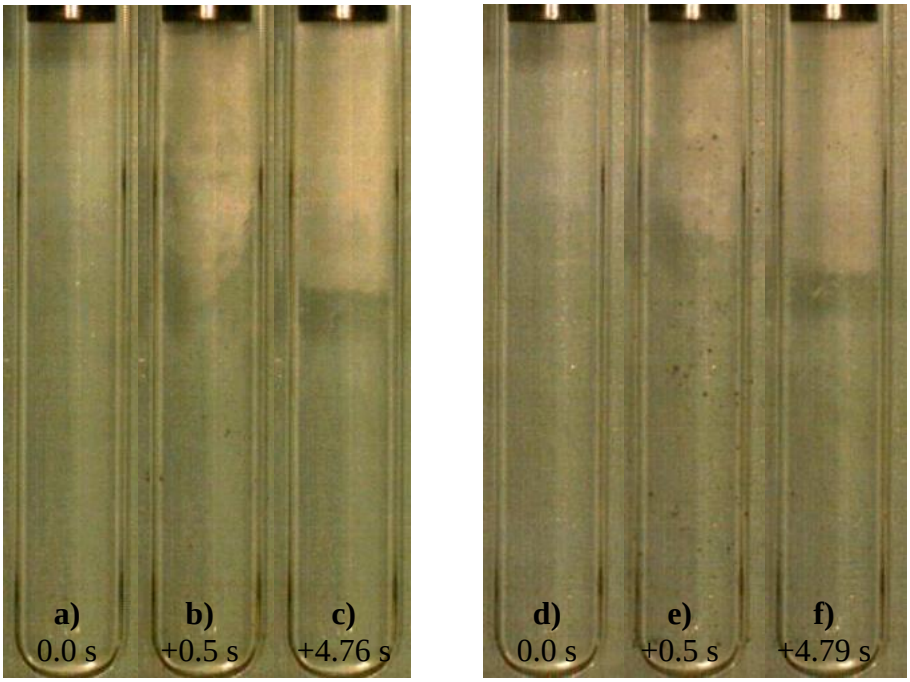

Figure 4.21. Samples of purified water ultrasonicated for 0.5 seconds ($A = 300\,\text{mVpp}$). The waveform was sinusoidal (a-c) and square with 50% duty cycle (d-f). Frames b) and e) are captured at the moment when ultrasonication stopped; in both cases still visible cavitation clouds disappeared after 6/1000 seconds. Dark dots in frame e) are not bubbles – they are particles of dirt in the heat transfer fluid that entered the crystallizer.

4.3.2. Supercooling between 2 and 5 ºC

Figure 4.22 shows solidifcation caused by a short pulse of ultrasound (0.01 seconds, or 233 oscillations). It is important to note that the tip of one thermocouple is in contact with the sonotrode, and that gave larger difference in temperature readings of the thermocouples. Despite relatively low density of nuclei created by a short ulrasonic pulse, it is evident that dendrites grown in the zone below the sonotrode are much finer that very coarse thermal dendrites beneath them, which can be seen comparing Figure 4.22c and Figure 4.22d.

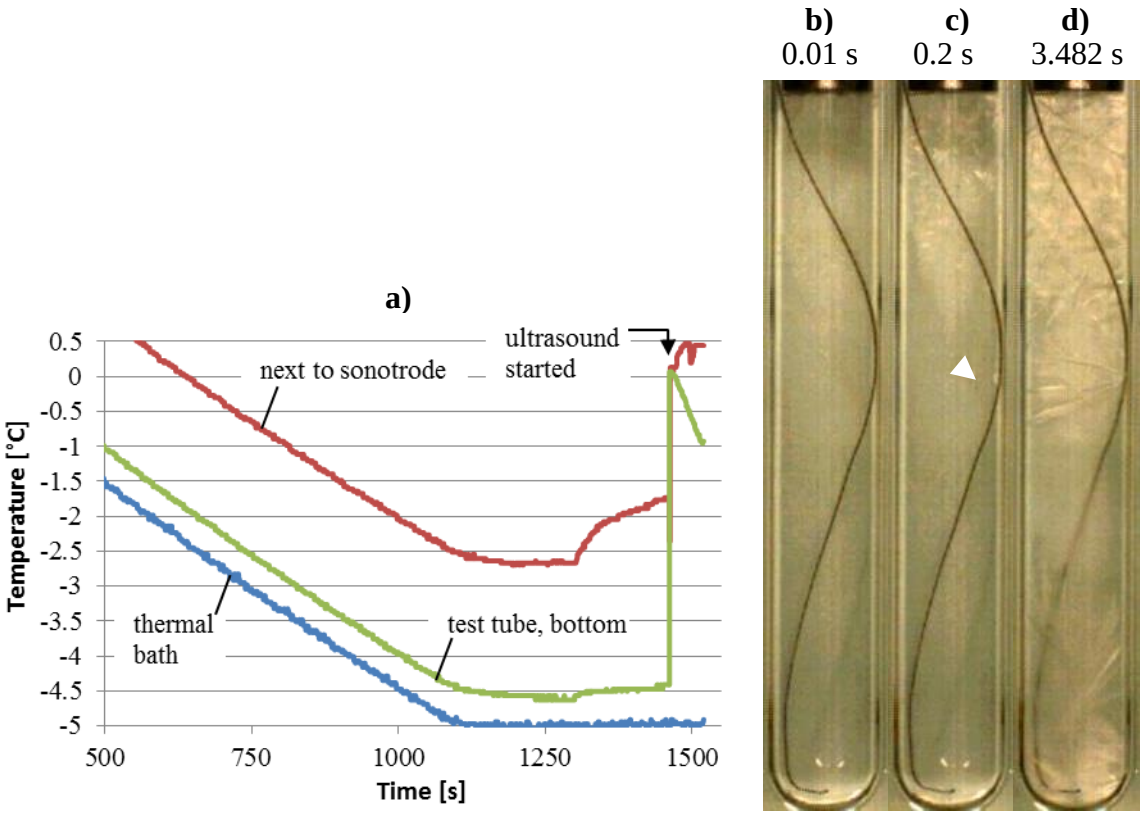

Figure 4.22. (a) Measured temperature next to the sonotrode and near to the bottom of the test tube. Applied ultrasound ($A = 300\,\text{mVpp}$) had duration of 0.01 seconds. Time indicated above the captures b) through d) is measured from the cavitation onset.

One notes in Figure 4.22a an increase in measured temperature at around 1300 seconds after the measurement started, during holding of the thermal bath at constant

temperature. The same feature is also shown in Figure 4.9, Figure 4.10, Figure 4.14a, Figure 4.24a below, and other figures that come after. This jump coincides with the moment when two strong lights (Figure 3.9) were turned on. Higher increase in temperature below the sonotrode shown in Figure 4.22a is because the therocouple tip was in direct contact with the sonotrode which heats up much more than the water below. Increase in the temperature up to +0.5 ºC after ultrasonification can be attributed to the heat from the sonotrode.

Solidification with immersed thermocouples, as in Figure 4.22, did not produce substantial difference, which is evident by comparison with Figure 4.23.

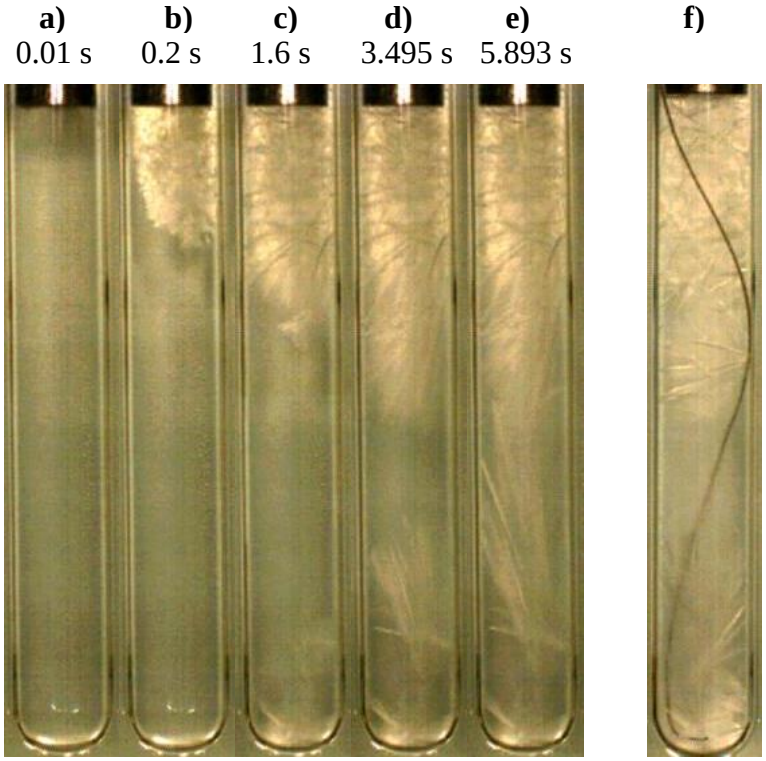

Figure 4.23. (a – e): Sample frozen under the same conditions as in Figure 4.22, just without thermocouples immersed. Time indicated above the captures is measured from the cavitation onset. (f): Sample from Figure 4.22, 5.826 seconds after the cavitation onset.

Figure 4.22d and Figure 4.23d, obtained around the same time after the cavitation onset, look very similar. The only difference is another nucleation site at the contact

between the thermocouple and the test tube wall, indicated in Figure 4.22c, which changed dendrite growth from the zone below the sonotrode. The thermocouple also seem to be an obstacle to dendrite growth (compare Figure 4.23e and Figure 4.23f).

In Figure 4.23a, which shows the moment when the sonotrode has stopped to oscillate, ceasing cavitation cloud as well as first appearance of ice crystrals are visible. Ice was also nulceated at the bottom of the test tube. This detail will be considered in the next chapter, when the effects of radiation pressure is estimated.

When ultrasound was applied for longer time (0.1 seconds), the density of nucleated ice below the sonotrode was higher (Figure 4.24b), resulting in equiaxed ice growth in that region, as shown in Figure 4.24c and Figure 4.24d. On the other hand, short ultrasonication (Figure 4.22 and Figure 4.23) resulted in what seems to be finer dendrites. Besides that, the test tube in Figure 4.24 is filled with ice much faster than in previous two examples, however it is also evident that coarse dendrites still grow below the equiaxed zone.

When the “radiation pressure” sonotrode (Figure 3.5) was used, ice was nucleated throughout the wall of the test tube, as shown in Figure 4.25. As a result, ice that was formed was much finer (Figure 4.25e) than in previously described experiments. The ice also filled the test tube in a shorter time. It can be seen that the majority of “dots” was created during the first half of ultrasonication (Figure 4.25a), they grow bigger (Figure 4.25b), and by the end of the ultrasonic irradiation (Figure 4.25c) their number does not increase, at least not significantly. Later, some of initial growth sites are consumed by surrounding ones (Figure 4.25d).

Watching a full sequence of high-speed images, it is easy to observe bubbles moving down the test tube. One of them is marked in Figure 4.25a. A sequence of images in Figure 4.26 shows nucleation of ice as a consequence of this bubble colliding with the test tube wall. The bubble could be traced up to its collapse, but its rebound was not observed.

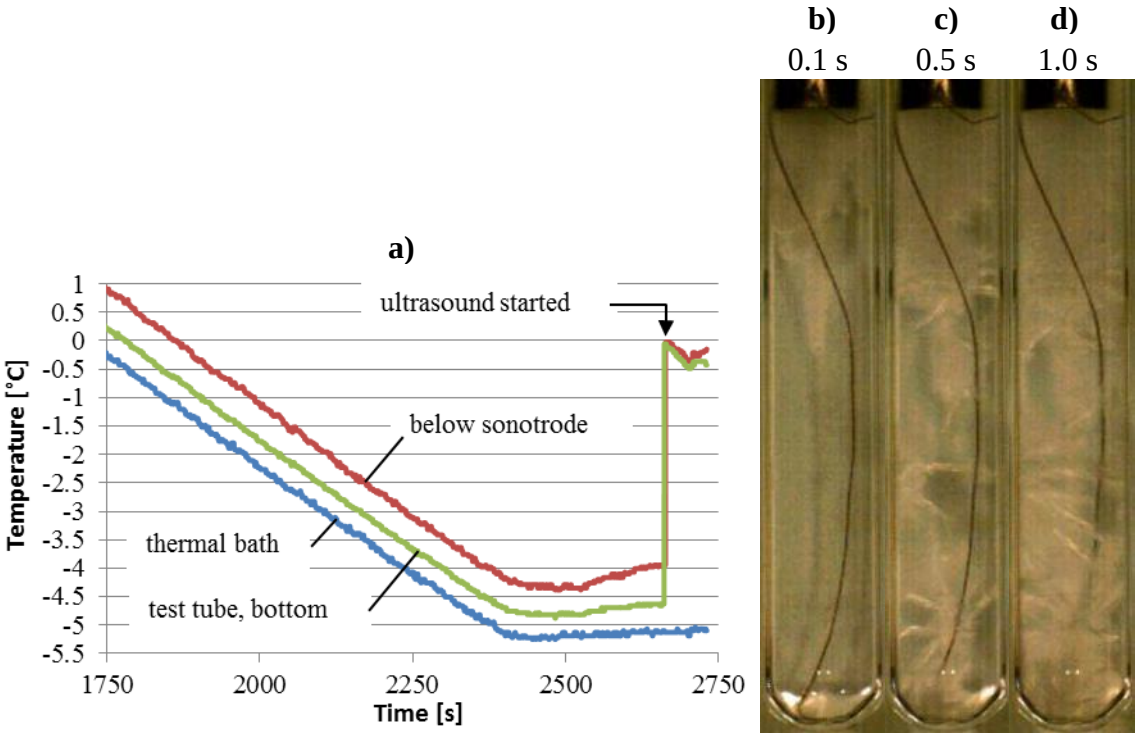

Figure 4.24. Measured temperature (a), and high-speed images of ice formation in the test tube. Duration of applied ultrasound ($A = 300\,\text{mVpp}$) was 0.1 seconds. Time indicated above the captures is measured from the cavitation onset.

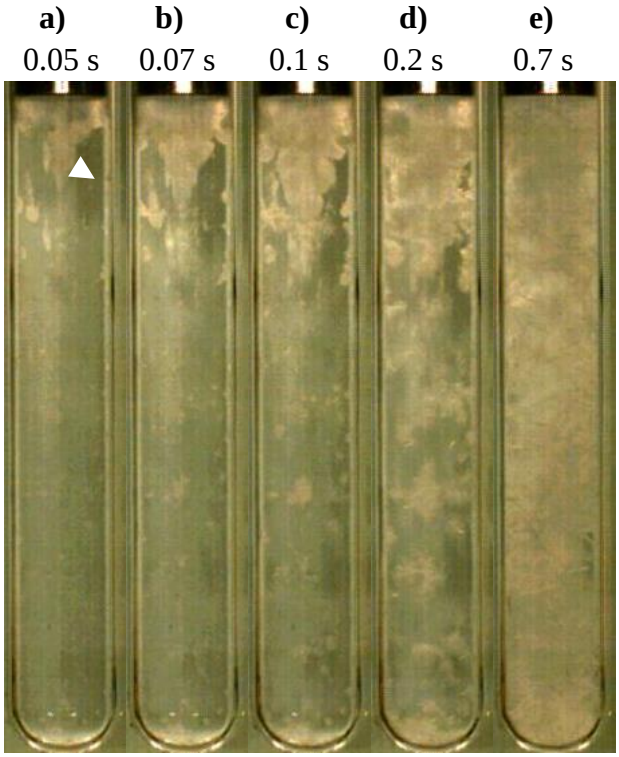

Figure 4.25. High-speed images of ice formation when the "radiation pressure" sonotrode used. Duration of applied ultrasound ($A = 300\,\text{mVpp}$) was 0.1 seconds. Time indicated above the captures is measured from the cavitation onset.

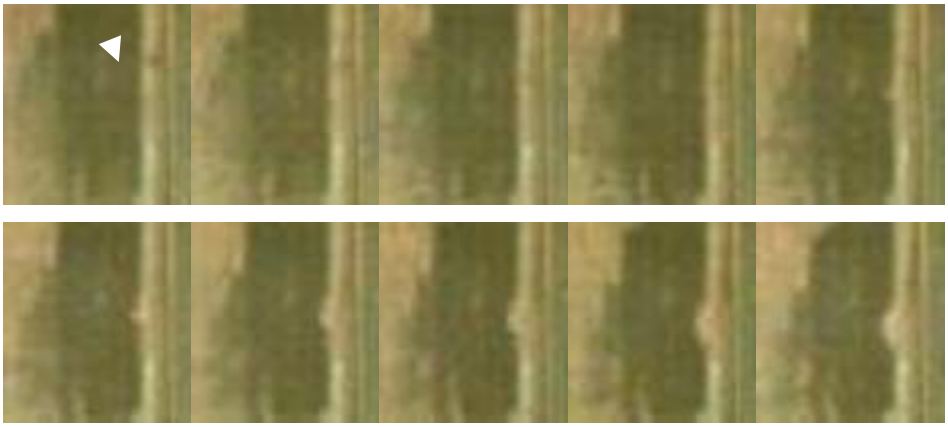

Figure 4.26. Magnified portion of the test tube marked with triangle in Figure 4.25. Frames cover the time between Figure 4.25a and Figure 4.25b in intervals of 0.002 s, with the first frame capturing the moment at 0.051 s and ending frame at 0.069 s after the cavitation onset.

The following example, Figure 4.27, is an example of remelting by excessive ultrasonication in a sense of the duration of ultrasound. Maximal density of ultrasonically nucleated ice crystals, judged visually, was reached between 0.3 and 0.4 seconds after ultrasound was started (Figure 4.27b). By the time ultrasound has stopped, large portion of ice created in the early stages had been remelted below the sonotrode. One second after cavitation had stopped, Figure 4.27d, the lower part of the test tube was almost filled with coarse dendrites, while no solidification occurred in the part next to the horn. Furthermore, around two seconds later some ice visibly floats up through that part.

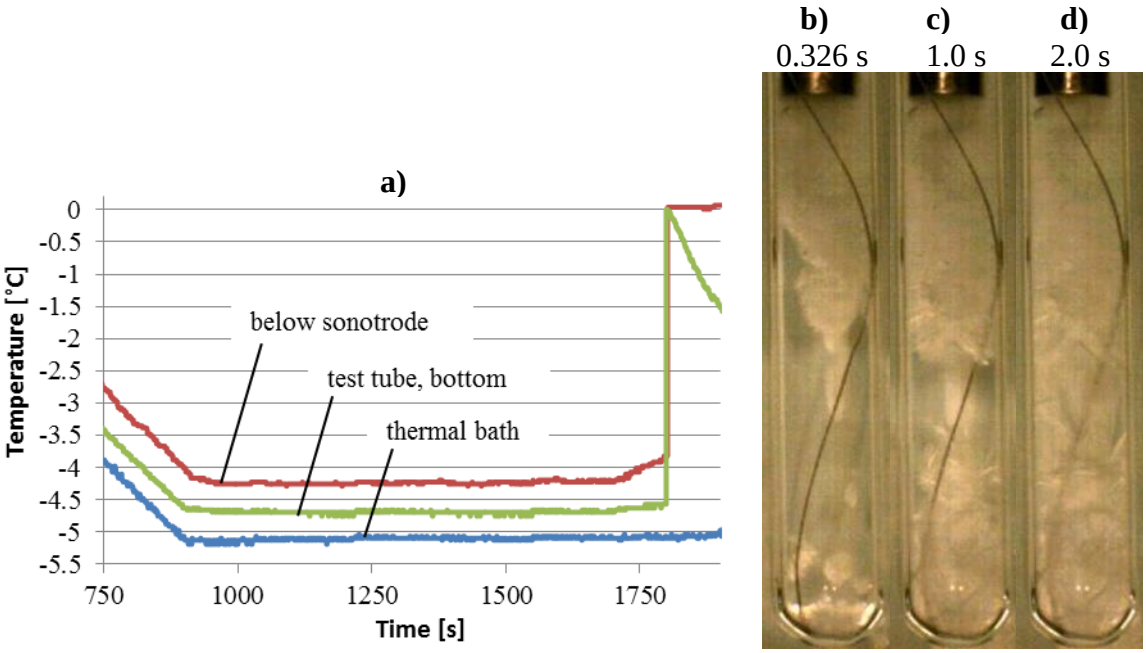

Figure 4.27. Measured temperature (a), and captures of ice in the test tube (b – d), where number of seconds above the captures signify the time passed after ultrasonic vibrations had commenced. Duration of applied ultrasound ($A = 300\,\text{mVpp}$) was 1.0 seconds.

With higher intensity of ultrasound, in this case $A = 900\,\text{mVpp}$, remelting of ice is even more obvious, as shown in Figure 4.28. Heating of water below the sonotrode after ultrasonification is very pronounced (Figure 4.28a). According to high-speed images, ice was continuously produced up to 0.2 seconds after ultrasound started (Figure 4.28b). After that period nucleation seems to cease, ice continues to grow thermally, and

remelting starts below the sonotrode. By 0.8 s from the start of ultrasound (Figure 4.28c), the upper 1/5 of the test tube has already been isolated that will be completely remelted by the end of ultrasonication (Figure 4.28d). The rest of the ice in the upper half is mushy in Figure 4.28c and Figure 4.28d is mushy.

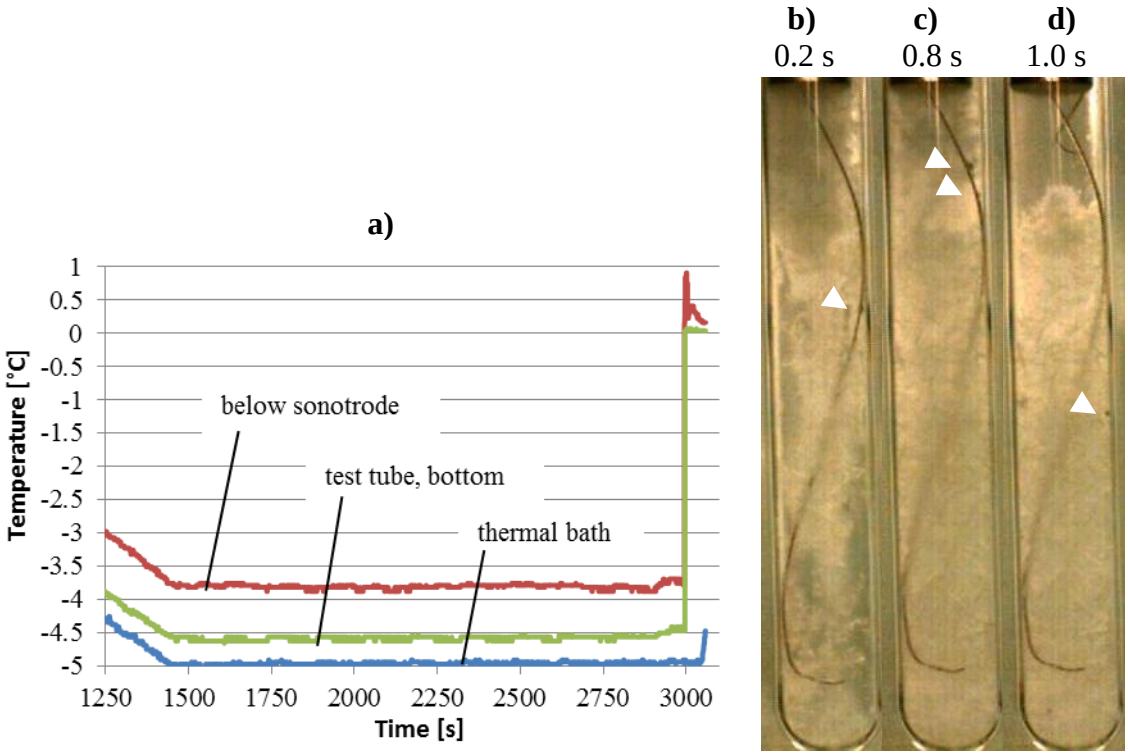

Figure 4.28. Measured temperatures (a) and high-speed images (b-d) from the experiment with higher intensity of ultrasound with $A = 900\,\text{mVpp}$, and a 2 seconds duration of ultrasonication. The captures were made 0.2 s (b), 0.8 s (c), and 2 s (d) after cavitation started. Triangle mark some of larger bubbles pushed downwards.

With the amplitude of pre-amplified signal $A = 900\,\text{mVpp}$, the free surface of the liquid around the sonotrode is easily disturbed, and the negative pressure phase at the sonotrode tip entraps more bubbles than when lower amplitudes are used. A few of those bubbles are shown in Figure 4.28. In a repeated experiment without thermocouples, one bubble was pushed all along the test tube wall. As shown in a sequence of high-speed images, Figure 4.29, the bubble travels downwards leaving a trace of ice behind. By closer inspection of the whole set of images it is possible to notice that bubble pulsates

and decreases in size while traveling. Ice growth in the path of the bubble is evident. Except in the last frame, ice growing in the bubble's path is wedge-like shaped, reflecting different times of growth.

Also shown in Figure 4.29 are two trails of ice left by two bubbles. Two arrows indicate the spots where those bubbles collided with the wall.

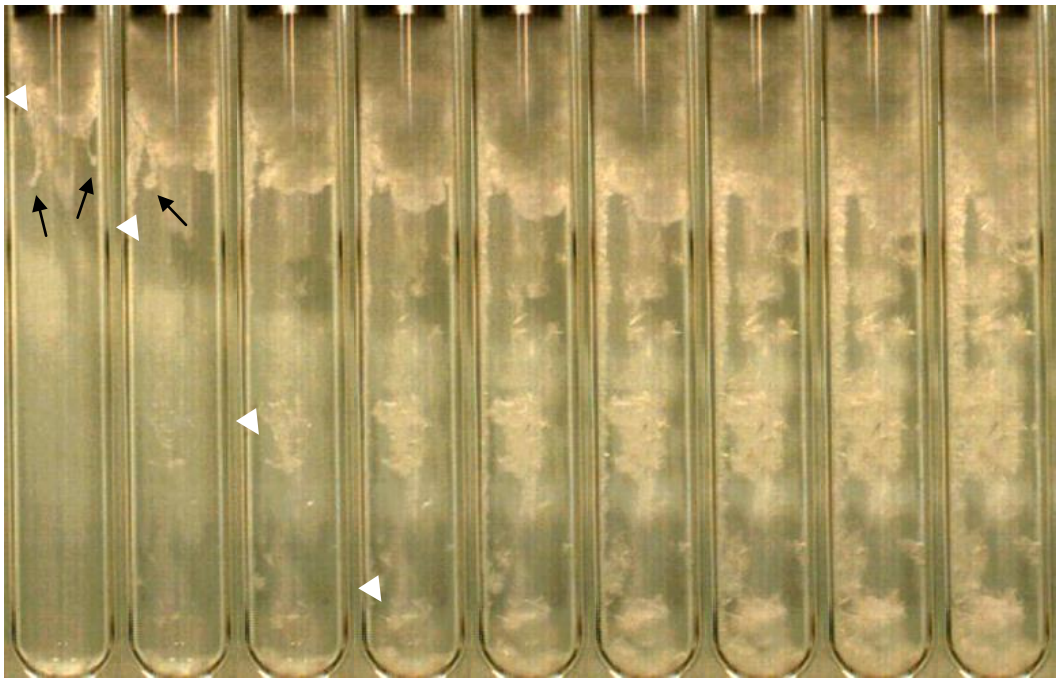

Figure 4.29. High-speed images taken the experiment with the same parameters as in *Figure 4.28*. The time interval between frames is 0.055 s, the leftmost frame taken 0.055 s after the cavitation onset, while the last one in the sequence is taken 0.455 seconds. White triangle follows one bubble as it is pushed along the test tube wall. The two black arrows indicate spots where two bubbles hit the test tube wall.

Occasionally, ultrasonic vibrations below the cavitation threshold (Section 4.1) could nucleate ice. As shown in Figure 4.30a through Figure 4.30f, no cavitation is visible below the sonotrode. However, bubbles were created around the pressure antinode, then pushed down and collapsed soon afterwards, either upon hitting the test tube wall, or upon arriving in the zone of high enough pressure. Only two bubbles, marked "A" and "B", nucleated ice when they collapsed at the test tube. It is interesting that not only bubbles are created and collapse at approximately the same distance from

the sonotrode, but many of them tend to converge to the same spot at the test tube wall, like bubbles marked 1, B, and 2. Also, what is designed as a bubble A is actually a cluster of three bubbles which collided in too short interval to conclude which one nucleated ice, or whether all of them took part in nucleation of ice.

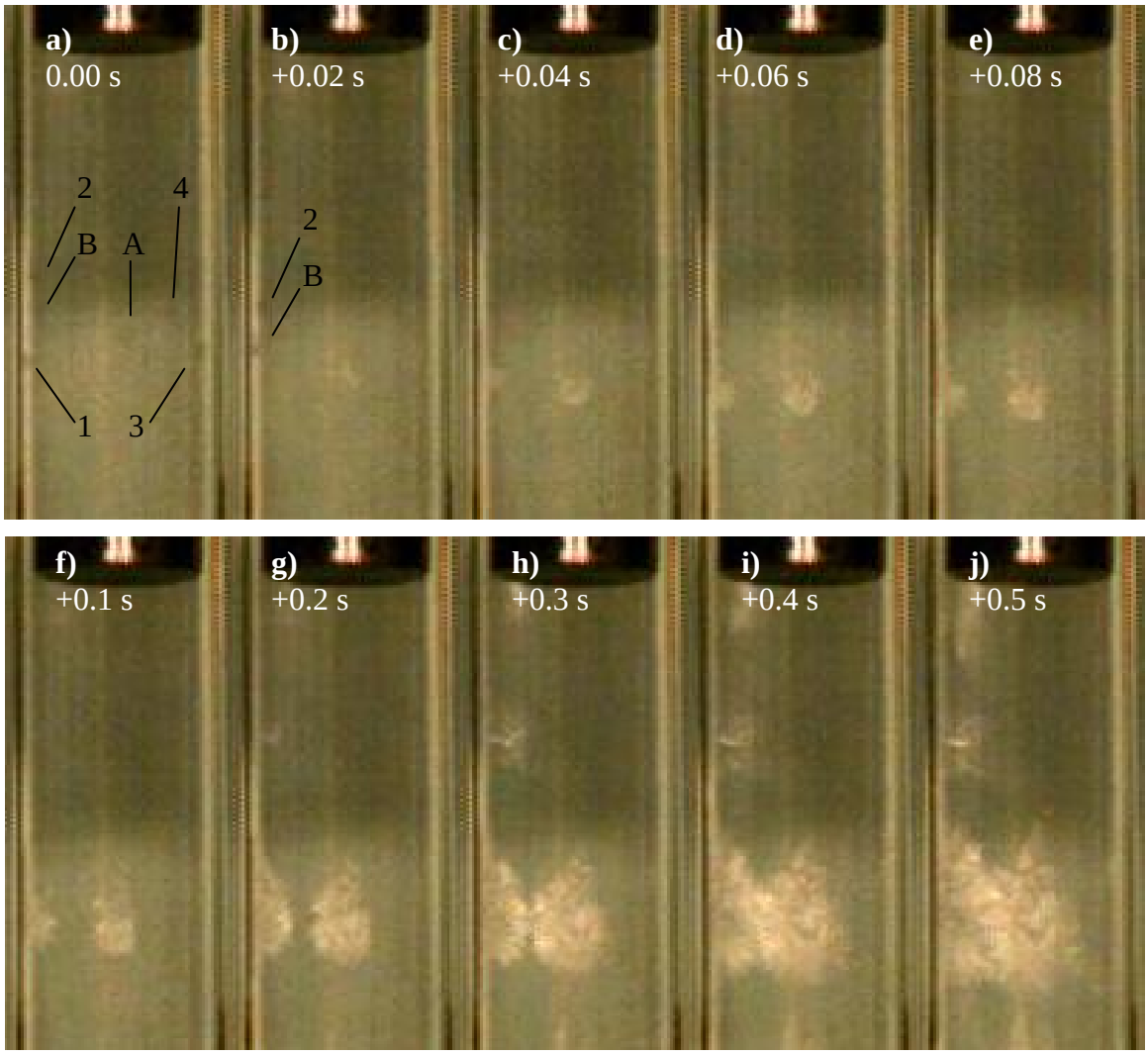

Figure 4.30. A sequence of high-speed images showing several bubbles, only bubbles "A" and "B" being active nucleation sites upon the collapse. More bubbles were produced in this sample than marked, some appear and collapse between the time instances shown in this set, while others are captured but much easier to see if watched as motion pictures. Duration of ultrasound ($A = 100\,\text{mVpp}$) was 0.1 second. Thermal bath was at -5 ºC.

Similarly to the experiment shown in Figure 4.13, the test tube was not inserted in the crystallizer all the way down, allowing the sonotrode tip to be close to the free surface of the heat transfer liquid. Increase in the temperature next to the sonotrode was additionally helped by directing a stream of warm air towards the sonotrode. The result is the measured temperature below the sonotrode that oscillated around +1.5 ºC (Figure 4.31). After ultrasound had started, the temperature below the sonotrode dropped to +0.163 ºC for 1 second, and then increased again. Fine ice was visible around the sonotrode, especially in Figure 4.31d through Figure 4.31g, but it is not clear whether only around the test tube wall or in the central zone of the test tube, where the temperature was measured.

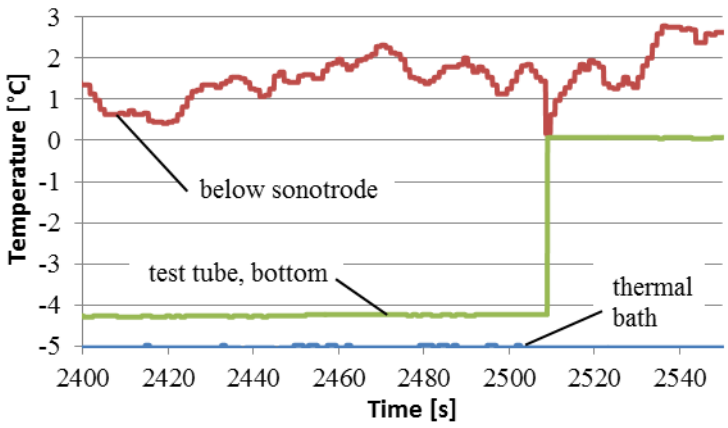

Figure 4.31. Temperature readings in the experiment where the thermal bath temperature was set to -5 ºC while the temperature of water below the sonotrode was kept at temperature above freezing point.

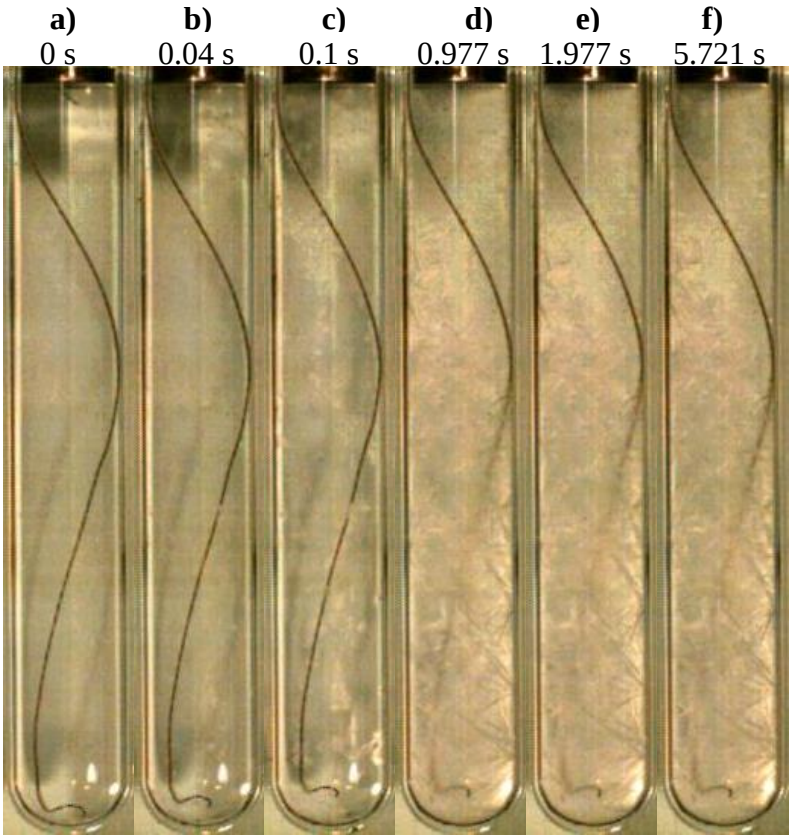

Figure 4.32. High-speed images of ice growth triggered by ultrasound ($A = 300\,\text{mVpp}$) with 0.1 s duration. Temperature measurement is given in Figure 4.31. Number of seconds next to each frame is the time elapsed form the moment when ultrasound started.

The waveform of the driving signal for oscillations of the sonotrode did not show to have any significant effect, like already shown for small supercooling.

4.3.3. Supercooling around 10 ºC

In the example shown in Figure 4.33a, temperatures at the onset of cavitation were -9.019 and -9.486 ºC below the sonotrode and at the bottom of the test tube, respectively. After ultrasound had started, ice formed immediately below the sonotrode, and after 0.006 s at the bottom and at approximately 2/5 of the water column measured from the bottom. These zones are shown in Figure 4.33b, captured 0.01 s after the

cavitation onset. Ice continued to grow mostly in these regions (Figure 4.33c) and it took around 0.24 s for ice to fill the test tube (Figure 4.33d).

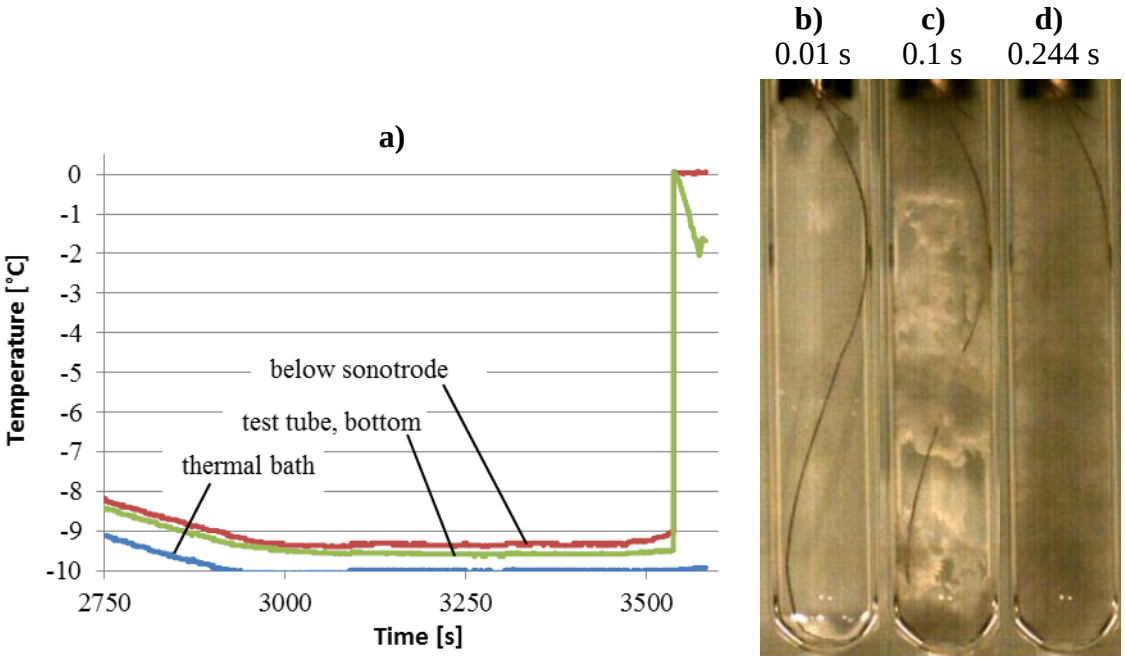

Figure 4.33. Measured temperatures (a) and high-speed images (b-d) from the experiment with 0.1 s duration of ultrasound ($A = 300\,\text{mVpp}$). Number of seconds next to each frame denotes the time elapsed form the moment when ultrasound started.

Without thermocouples, nucleation sites become more numerous and scattered throughout the test tube, as shown Figure 4.34. Appearance of these quasi-periodic formations resembles those in Figure 4.25, except the spots appeared bigger in shorter time. Roughly estimating, the whole test tube in Figure 4.34a was filled with ice after 0.19 seconds, and in Figure 4.34b after 0.175 seconds.

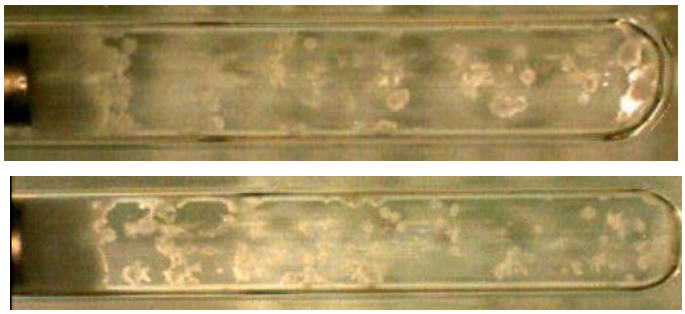

Figure 4.34. Ice formed 0.04 seconds after the cavitation onset, with the amplitude of pre-amplified signal 300 mVpp (a), and 900 mVpp (b).

With the supercooling which is relatively close to the temperature of spontaneous nucleation, ice is created practically without an incubation period. Also, no strong stimuli are required to cause nucleation. With the amplitude of pre-amplified signal below the cavitation threshold defined in Section 4.1, ice could be nucleated. Shown in Figure 4.35 is ice grown only from one nucleation site, and it can serve as a good comparison for the time needed to fill the test tube with ice without the help of ultrasound when supercooling is between 9 and 10 ºC.

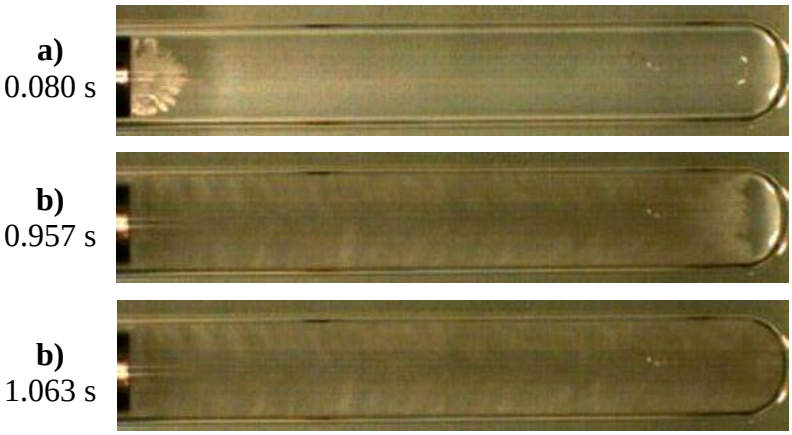

Figure 4.35. Growth of ice nucleated at the sonotrode with 0.01 second of vibrations below the cavitation threshold ($A = 100\,\text{mVpp}$). Indicated is the time elapsed from the moment the first glimpse of ice appeared at the sonotrode.

Situation in Figure 4.35 occurred only by chance. With ultrasonic parameters below the cavitation threshold, ice usually occurred at the bottom of the test tube and/or on the side wall of the test tube. In most of the experimental runs nothing could be noticed in the test tube before ice nucleated. However, in one experiment bubbles were large enough and were caught clearly to cause ice nucleation, as shown in Figure 4.36 and Figure 4.37. Ultrasound with $A = 100\,\text{mVpp}$ was applied for 0.1 second. Figure 4.36 and Figure 4.37 show a succession of 42 high-speed images with 0.001 second between adjacent images. Bubbles are clearly visible to cause ice nucleation at the spot where they hit the test tube. One bubble on the right-hand side can be clearly seen to collapse, trigger nucleation, and stray trapped inside ice after its rebound.

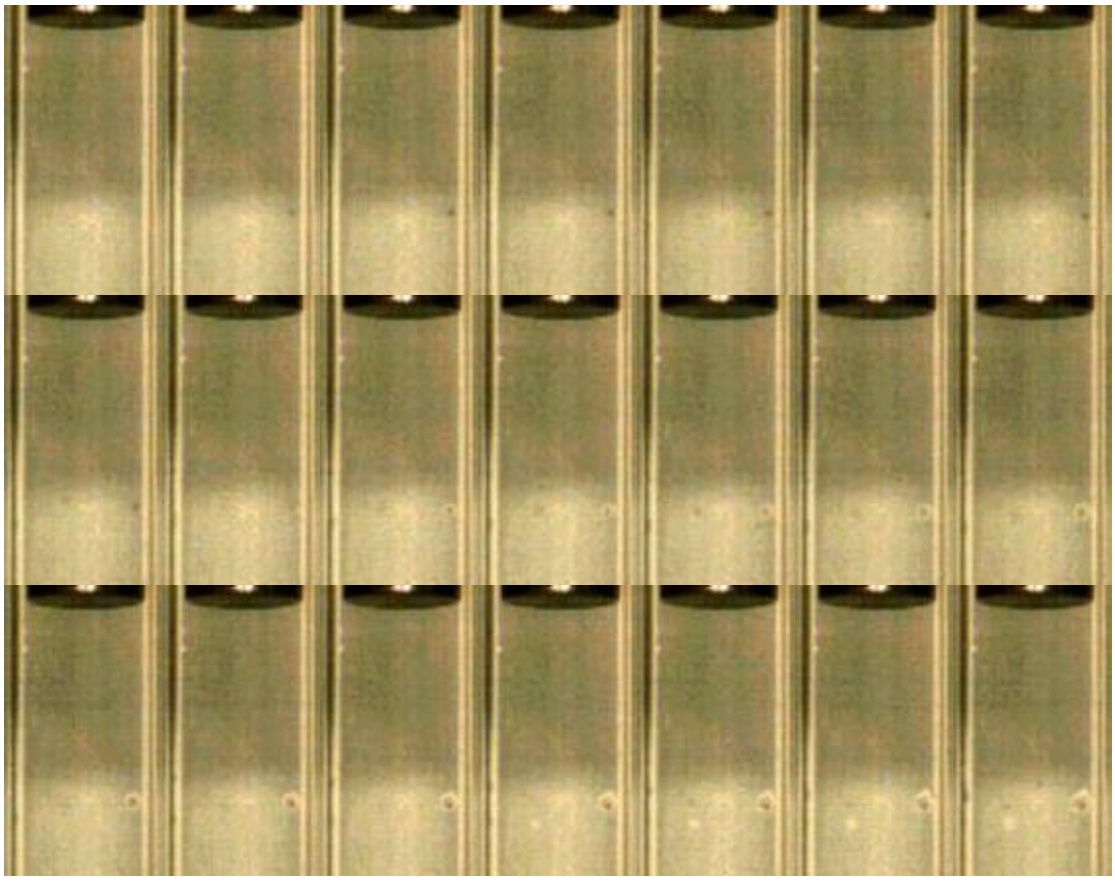

Figure 4.36. A one millisecond succession of high-speed images showing nucleation of ice by bubbles created with ultrasound below the cavitation threshold ($A = 100\,\text{mVpp}$).

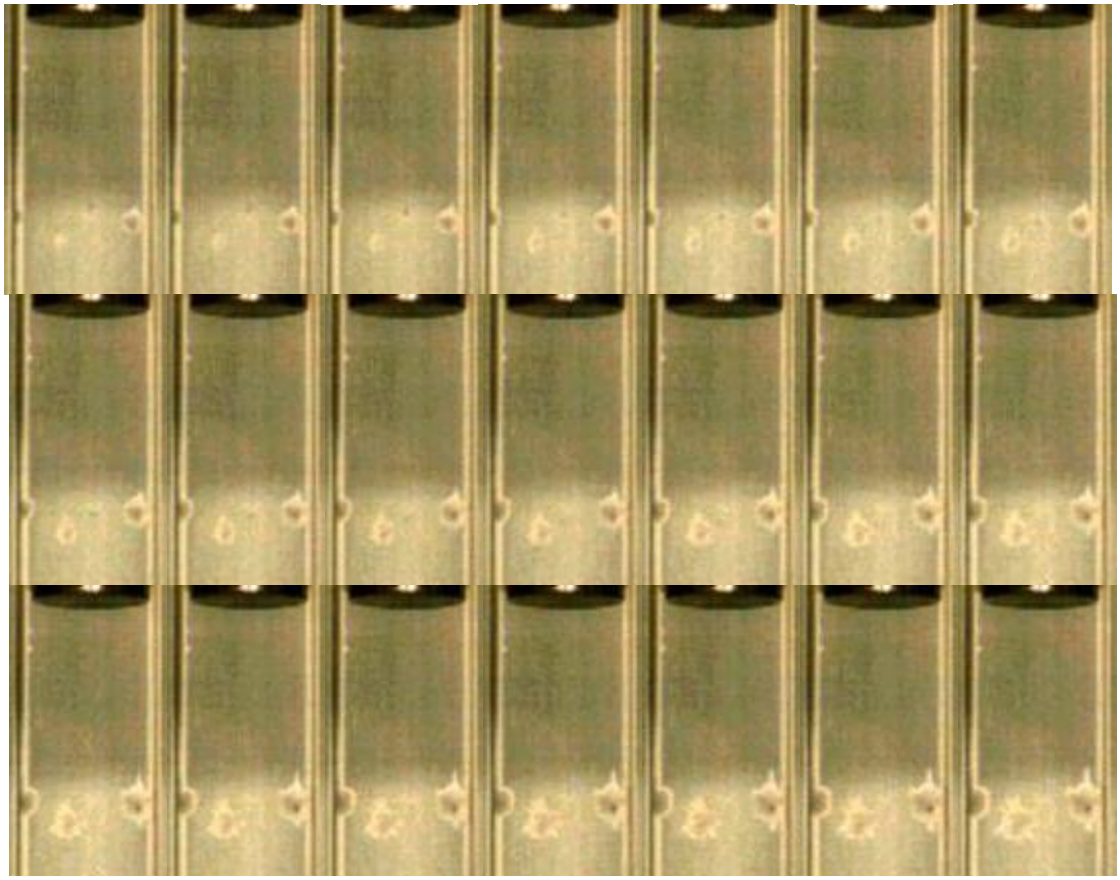

Figure 4.37. (Figure 4.36 continued). A one millisecond succession of high-speed images showing nucleation of ice by bubbles created with ultrasound below the cavitation threshold ($A = 100\,\text{mVpp}$).

It is interesting that no visible bubbles were created below the sonotrode, but only away from it, in the zone that seems to be the pressure antinode. That does not exclude, however, that bubbles are created next to the sonotrode and become larger when arrive in the zone with low pressure. When the high-speed images are reviewed as a movie, it is apparent that bubbles tend to converge and hit the test tube in the same spots, an interesting behavior observed also in Figure 4.30.

Excessive ultrasonification seems to manifest only in remelting of the layer adjacent to the sonotrode, as shown in Figure 4.38. At lower ultrasonic intensity ($A = 300\,\text{mVpp}$) ice filled the test tube in about 0.21 seconds, while it took around 0.17 seconds at higher intensity ($A = 900\,\text{mVpp}$). In both cases remelting was started around

0.15 seconds after freezing was completed, while after 0.5 seconds one can recognize the layer that would be completely remelted.

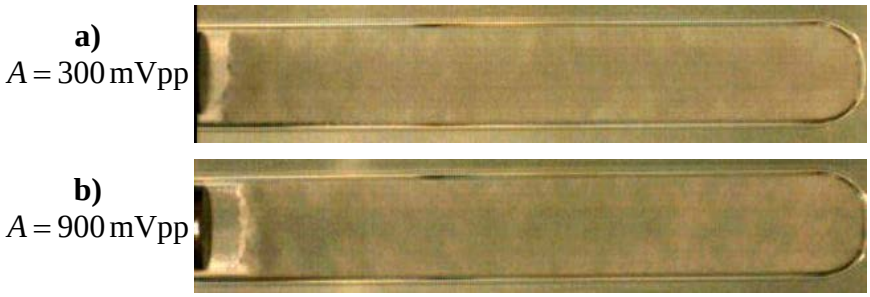

Figure 4.38. Remelting of ice by too long ultrasonication (2 seconds in both cases) for two amplitudes of pre-amplified signal, 300 and 900 mVpp. The images were taken (a) 0.058 s and (b) 0.027 seconds after ultrasound had stopped.

4.4. Fragmentation of Dendrites by Bubbles

Figure 4.39 shows event when a bubble enters a mushy zone with growing dendrites and fragments them. Threated liquid is aqueous solution of ammonium chloride (4.5 weight %). Nucleation was first induced by tapping a glass rod against the bottom of the test tube. While the solid phase was growing, the "acoustic streaming" sonotrode was immersed in the liquid so a bubble remains trapped at its tip (marked with arrow in Figure 4.39a). Ultrasound with the intensity above the cavitation threshold ($A = 600\,\mathrm{mVpp}$) was applied in burst with the rate of 5 bursts per second and 50% duty cycle. A thin cavitation zone can be seen by comparing frames b) through e) with frame a), however no new crystals could be observed.[20] Hence all the small crystals in frames b) through e) are fragmented by the bubble.

The bubble was first propelled by the ultrasonic field towards the test tube wall, and after bouncing off, it started to oscillate vigorously. When the bubble reached the

---

[20] Formation of the solid phase under identical conditions is shown in Figure 4.17. First crystallites were observed around 0.63 seconds after the onset of the first cavitation cycle (Figure 4.17), but more significant amount of crystals was formed between 1.3 and 2 seconds after ultrasonication had started.

dendrite, first fragments were ejected and the bubble split in two smaller bubbles (Figure 4.39d). One of them entered the mushy zone, while the other (marked with arrow in Figure 4.39e) bounced back and headed in the opposite direction. The swirling mixture in Figure 4.39f, taken 0.144 s after the first burst ceased, may contain newly nucleated crystals together with fragmented ones but, as already mentioned in the footnote on this page, they are most likely not visible after such a short time.

Ultrasonication of the SCN-water solution most likely produced some dendrite fragments, but not nearly as much as in the solution of ammonium chloride. An example is shown in Figure 4.40. One reason for that is that dendrites are relatively far from the sonotrode and acoustic field is not strong enough to produce collapse/rebound motion of bubbles. Other reasons are higher solid fraction in the mush and high ductility of SCN dendrites. Since the test tube is three-dimensional space, it is often difficult to conclude whether a bubble actually interacts with the mushy zone.

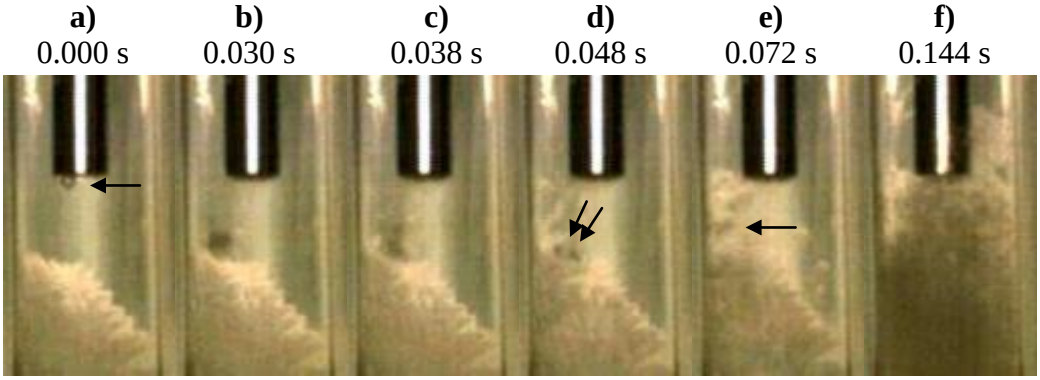

Figure 4.39. Fragmentation of a growing dendrite by a bubble. The liquid is water with 4.5 wt% ammonium chloride. Ultrasound ($A = 600\,\text{mVpp}$) was applied in bursts, with the frequency of 5 Hz and 50% duty cycle.

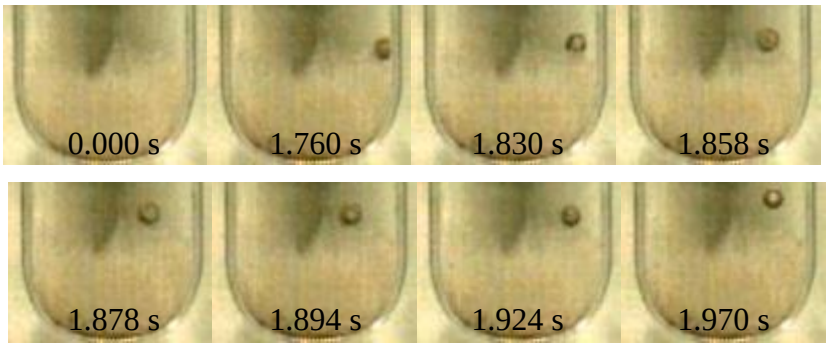

Figure 4.40. High-speed images of a bubble encountering SCN dendrites. Continuous ultrasonic field ($A = 300\,\text{mVpp}$) was applied. Despite poor image quality, it can be seen that the bubble did not cause significant damage to dendrites. Small fragments might have been produced, but the scale of fragmentation is far from that shown in Figure 4.39.

4.5. Potential Effect of Radiation Pressure on Dendrite Fragmentation

As already mentioned, radiation pressure has not been mentioned before as a phenomenon that might have some significance in solidification. The following experiment was used to verify if radiation pressure could have some sensible effect. A cork was used to make a flat bottom and seal the dome end from the rest of the test tube (Figure 4.41). When the test tube was filled, water passed through the cork, but not all air could escape. When ultrasound was applied, only a portion of radiation pressure not absorbed by cork could influence behavior of the bubble in the isolated compartment. Although the sonotrode (S&M 1102, see Section 3.1) is 90% of the test tube diameter and cork is a good sound absorber, radiation pressure at the bottom of the test tube is quite noticeable. By observing high-speed images, it is quite apparent that agitation comes from the cork, not the test tube wall. However, that does not exclude a possibility that significant portion of vibrations of the cork were transferred from the test tube.

Trials to fragment dendrites in ammonium chloride crystals were not so successful, especially knowing that its solidified aqueous solution is very mushy with the concentration used in experiments (4.5 wt%). Nucleation was induced by a glass rod, and due to small supercooling (around 1 ºC or less), it was quite difficult to do so. Figure 4.42 shows a successful trial. Comparing Figure 4.42a with Figure 4.42b, the two solid

clusters were moved downwards during the first pulse. However, it took six bursts to cause significant damage to the clusters as well as their larger shifting (Figure 4.42d).

If initial dendrites grew near the sonotrode, like in case of SCN-water solution (Figure 4.43 through Figure 4.45), dendrites can be completely fragmented, even if SCN dendrites make a good contact with the test tube and are very ductile. However, dendrites that grew in the lower part of the test tube were intact by the action of ultrasound and bubbles that reached there (Figure 4.40, Figure 4.44, and Figure 4.45). Unlike aqueous ammonium chloride, initial precipitation in the SCN-water solution was spontaneous.

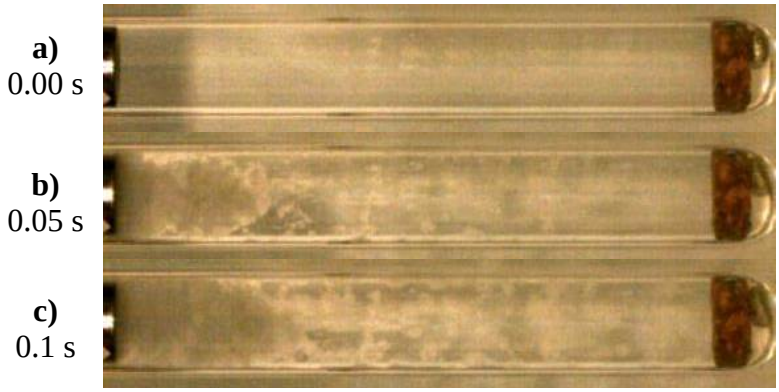

Figure 4.41. Captures made by a high-speed camera at the moment ultrasound ($A = 300\,\text{mVpp}$) is starting (a), at the moment it is stopping (c), and half time in between (b). Water is used, and the thermal bath temperature was set to -5 ºC.

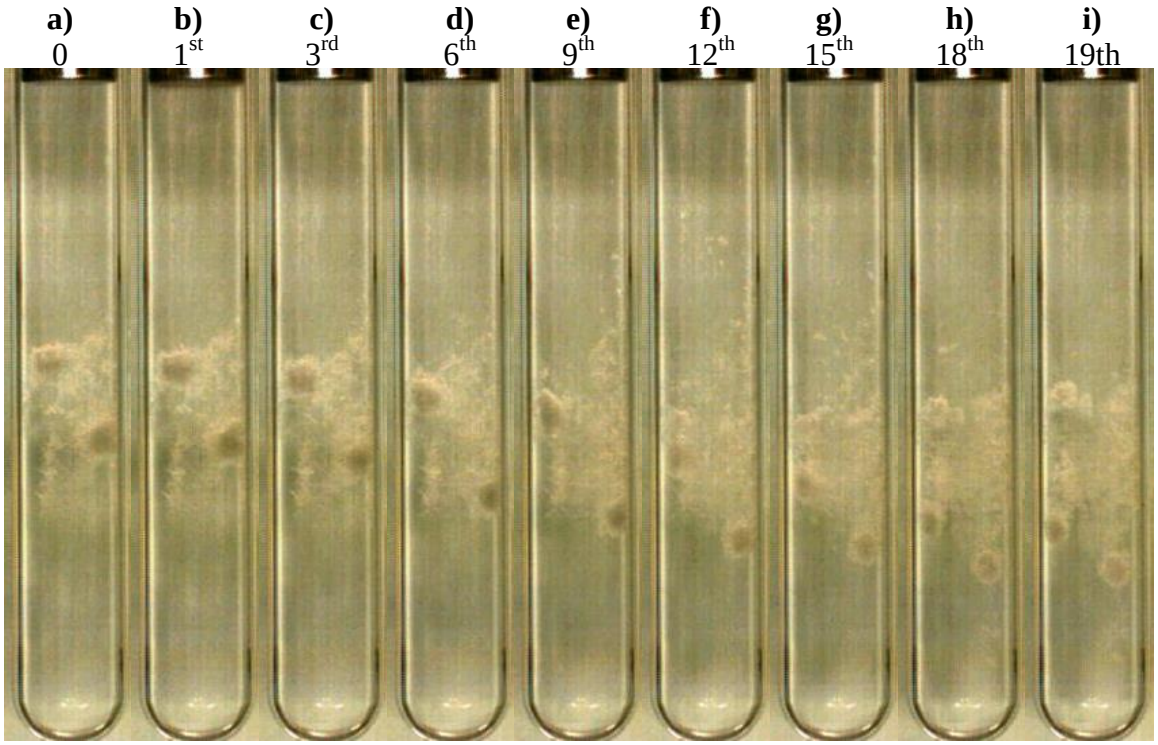

Figure 4.42. Position of ammonium chloride (4.5 wt%) crystals after 19 burst applied within approximately 11.5 seconds. Duration of each burst was 0.1 second, but they were applied manually in irregular intervals. The amplitude of pre-amplified signal was 600 mVpp. Temperature of the thermal bath was set to -5 ºC, so the supercooling is estimated to be less than 1 ºC

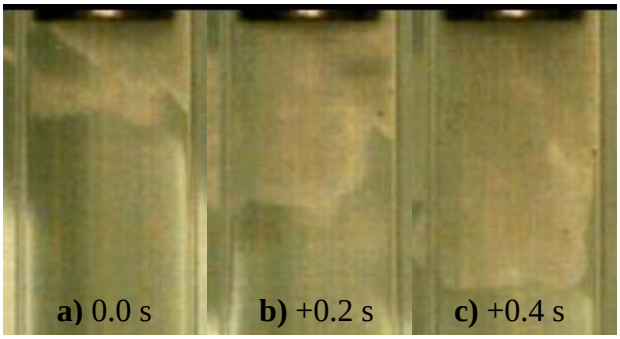

Figure 4.43. Nucleation of the solid phase and dendrite fragmentation, where a) is captured at the moment the first, b) when the second, and c) when the third burst starts. Sinusoidal wave with $A = 600\,\text{mVpp}$ was applied with 5 bursts per second and 50% duty cycle. Temperature in the thermal bath was set to +22 ºC, so estimated initial temperature was around +21.75 ºC.

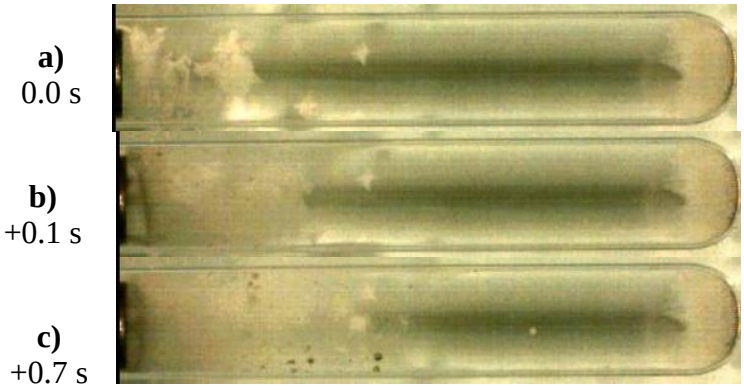

Figure 4.44. At the moment when ultrasound is commencing (a), some precipitation had already proceeded for several minutes. Ultrasound was continuous with $A = 600\,\text{mVpp}$, while estimated initial temperature was around +23.75 ºC (temperature in the bath was set to +24 ºC). This is the sample as in Figure 4.20.

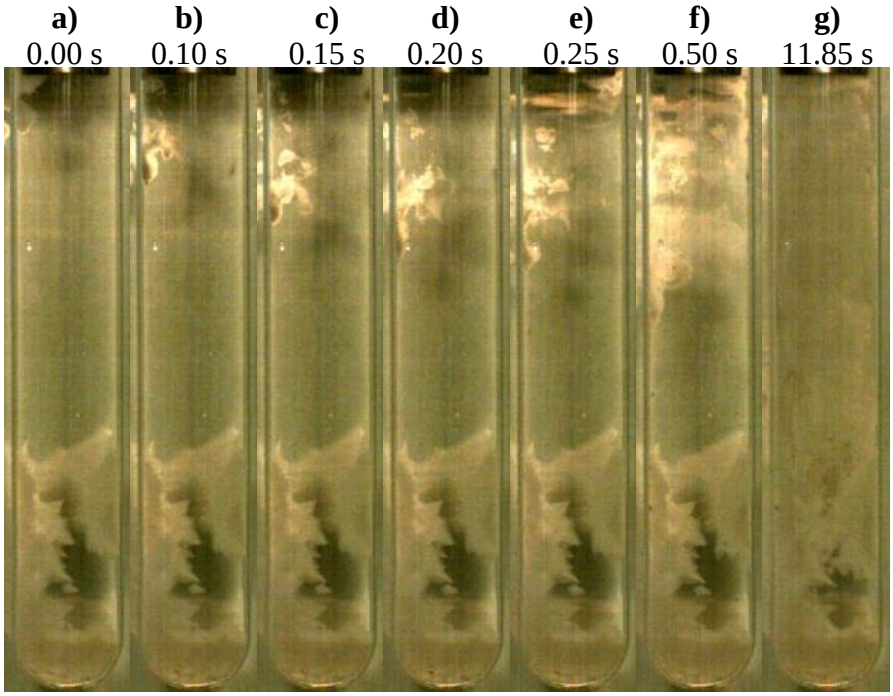

Figure 4.45. Ultrasound ($A = 300\,\text{mVpp}$) was applied for 0.5 seconds (frame f). Initially, SCN precipitated at the bottom of the test tube. Precipitation below the sonotrode was allowed for some time before ultrasound was started. Frames b) through d) show complete breakup of those dendrites, while dendrites at the bottom remain intact. New crystals became visible around the time in frame d) and are clearly visible in frame e). Frame g) illustrates difference in the growth rate between ultrasonicated and unprocessed (bottom) part of the sample. Estimated initial temperature was around +23.75 ºC (temperature in the bath was set to +24 ºC).

4.6. Gas Entrapment and Morphology of Solidified Solutions

Figure 4.46 shows sample from Figure 4.43 ($A = 600\,\text{mVpp}$, bursts 5 Hz, 50% duty) at the end of ultrasonication. Figure 4.47 was taken two hours after ultrasonication of the sample, together with the sample solidified in air two days earlier. Both samples were held in vertical position, except for taking the image, when they were laid horizontal position. The ultrasonicated sample (Figure 4.47a) has segregated, the lower part containing fine equiaxed grains, and the top quarter filled with liquid. The unprocessed sample (Figure 4.47b) consists of coarser dendrites without segregation regions, except a thin layer next to the oxidized surface.

Figure 4.46. Sample from Figure 4.43, approximately 11.8 seconds after the cavitation onset (Figure 4.43a), shortly before the final pulse.

a)

b)

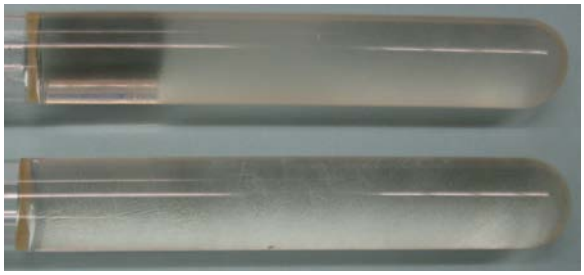

Figure 4.47. Sample a) is from Figure 4.43 and Figure 4.46, two hours after ultrasonication. Sample b) is two days after it solidified at room temperature. Both samples were held in vertical position all the time, except for taking this image. A crust, most likely oxide, formed at the surface during solidification.

Another sample is SCN with 4.5 wt% water, solidified at room temperature and left in the test tube for two months. It was ultrasonicated with the “radiation pressure” sonotrode. Due to viscosity and surface tension, air could not be released through the gap between the sonotrode and the test tube, so larger air bubble remained trapped (Figure

4.48). During ultrasonication, the bubble oscillated around the pressure antinode (Figure 4.48b). Some small bubbles that were created from the large one, together with newly created cavitation bubbles, were forced down the test tube into the mushy zone.

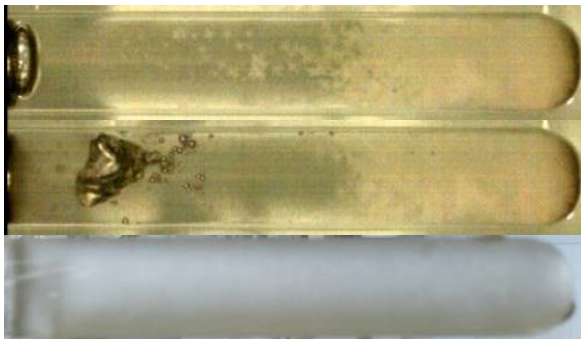

Figure 4.48. (a) SCN-4.5 wt% water prepared and solidified two months before this experiment. The sample was remelted at +35 ºC, and then cooled down to around +21.75 ºC. Visible are precipitates with free crystals slowly sinking down, the so called "snowing" effect. (b) A moment captured close to the end ultrasonication (around 5.6 seconds after the start), showing oscillations of a large bubble initially entrapped below the sonotrode. No visible crystals have been formed during ultrasonication, but after longer delay. (c) The sample just taken out of the crystallizer. The sample is still mushy, but no liquid segregation occurred.

All the three above mentioned samples, together with the sample shown in Figure 4.20 and Figure 4.44, were set in the horizontal position for 15 hours. In samples c) and d) in Figure 4.49, segregated liquid mixed to some extent with the mushy zone with equiaxed grains. That process was helped by shaking gently these two samples to confirm that they consist of liquid and solid phases On the other hand, no significant change was noticed in samples a) and b). Also, gas bubbles can be observed in ultrasonicated samples, samples b), c), and d) in Figure 4.49.

In Figure 4.49, bubbles in the sample d) are located at the bottom of the test tube, and it corresponds to the collection of small bubbles at the bottom of the test tube in Figure 4.20. Excessive gas porosity in sample b) is quite evident. On the other hand, no (significant) porosity is visible in unprocessed sample solidified at room temperature (sample a).

After additional eight days in the horizontal position, all the samples except one (the two-month old sample, shown and second from left in Figure 4.49 and Figure 4.50) achieved similar structure. Approximately the same amount liquid phase collected next to the surface. The only difference is the number, size, and distribution of bubbles entrapped in the samples (Figure 4.50). Figure 4.51 shows solid phase remaining after the liquid from the sample solidified without ultrasound had been decanted.

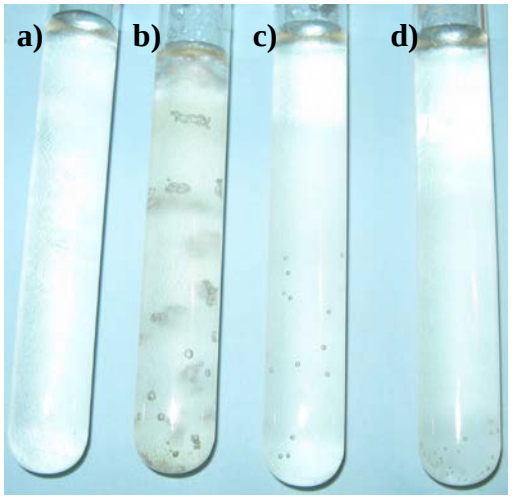

Figure 4.49. (a) Sample solidified and kept in vertical position for two days (the sample from Figure 4.47b). (b) Sample from Figure 4.48. (c) Sample from Figure 4.43, Figure 4.46, and Figure 4.47a. (d) Sample from Figure 4.20 and Figure 4.44. The image was taken 15 hours after all four samples had been laid in the horizontal position.

Figure 4.50. SCN-water samples after additional eight days in horizontal position. The first two samples from left are samples a) and b) from Figure 4.49 placed in the same order.

Figure 4.51. Solid fraction of untreated sample after the liquid had been decanted.

As already mentioned, the hypereutectic concentration of the water-ammonium chloride solution was not used because of the “snowing” effect (Figure 4.52), but also because of the long time lag between applied ultrasound and the moment when its effects become visible (Figure 4.52b). After ultrasonication the density of “snowing” crystallites is multiplied many times, and the crystals are much finer (compare samples a) and b)), but the time lag is long.

a)

b)

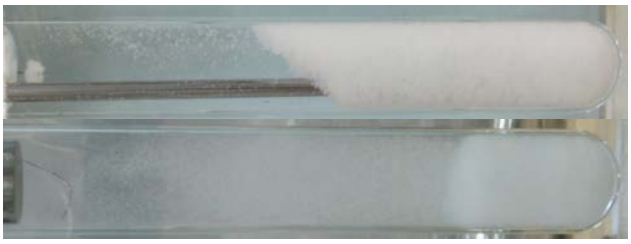

Figure 4.52. Aqueous solution of ammonium chloride (25 wt%). (a) The solution is solidifying spontaneously, with two surface thermocouples (MT-D, Section 3.1) immersed. Agglomeration of crystallites is visible around the tip of the thermocouple placed below the free surface. Picture was taken while the temperature in the sample was between -2 and -4 ºC. (b) A sample pictured roughly one minute after 1 second of ultrasonication ($A = 300\,\mathrm{mVpp}$). Temperature in the cooling bath was set to +2 ºC, while the solution is saturated at around +7 ºC.

CHAPTER 5. DISCUSSION, CONCLUSIONS, RECOMMENDATIONS

Discussions in the first three sections of this chapter, Sections 5.1, 5.2, and 5.3, have two-fold purpose. In these sections are presented simple estimations of physical parameters that led to results presented in the previous chapter, and they serve as building blocks that support further discussion in Section 5.4.

5.1. On the Collapse and Rebound of a Single Bubble

Because they are filled with a gas and/or vapor, bubbles have inert reaction to changes around them, as discussed in Sections 2.1.2 and 2.1.3. The main feature of interest in this work is pressure that develops upon the collapse and rebound of a bubble. There are numerous examples in the literature about high pressures developing around collapsing bubbles. However, the behavior of a bubble is not so straightforward, as will be shown in this section. For example, only slight changes in the amplitude of driving pressure can lead from high pressures developed upon violent bubble collapse, to not so much violent collapse and hence much smaller pressures.

To estimate the motion of the bubble wall, we will use Eq. 2.19, Eq. 2.21, and Eq. 2.22:

$$\left(1-\frac{\dot{r}_b}{c_b}\right)r_b\ddot{r}_b+\frac{3}{2}\left(1-\frac{\dot{r}_b}{3c_b}\right)\dot{r}_b^2=\left(1-\frac{\dot{r}_b}{c_b}\right)\frac{r_b\dot{h}_b}{c_b}+\left(1+\frac{\dot{r}_b}{c_b}\right)h_b \qquad \text{Eq. 2.19}$$

$$h_b = \frac{n}{n-1}\frac{\left(p_\infty + B\right)^{1/n}}{\rho_L}$$

$$\left\{\left[\left(p_\infty + \frac{2\gamma}{r_{b0}}\right)\left(\frac{r_{b0}}{r_b}\right)^{3\kappa} - \frac{2\gamma}{r_b} + B\right]^{\frac{n-1}{n}} - \left[p_{atm} - p_A \sin\left(2\pi f t\right) + B\right]^{\frac{n-1}{n}}\right\} \qquad \text{Eq. 2.21}$$

$$c_b = \sqrt{c_\infty^2 + (n-1)h_b} \qquad \text{Eq. 2.22}$$

Assumed pressure in the liquid at infinity (sonotrode surface) is

$$p_\infty = p_{atm} - p_A \sin\left(2\pi f\, t\right) \qquad \text{Eq. 5.1}$$

The collapse and rebound of a bubble will be assumed as purely adiabatic process, so the pressure inside the bubble is approximated as

$$p_b = p_{b0}\left(r_{b0} / r_b\right)^{3\kappa} \qquad \text{Eq. 5.2}$$

This equation of state for the gas inside the bubble, used by Hickling and Plesset (1964), gives the highest pressure at the bubble-liquid interface. More complex equations of state have been used in literature, which include additional effects, mostly surface tension and viscosity (Ivany & Hammit, 1965), or the van der Waals hard core radius (Löfstedt, Weninger, Putterman, & Barber, 1995), or all of the above mentioned (Holzfuss, Rüggeberg, & Billo, 1998).

It is evident that the choice of the equation of state, in other words a combination of physical effects, is based on individual preference. We decided to use Eq. 5.2 because surface tension in small scales and under high pressures seems to be very different from the bulk value. Namely, it has long been known that surface tension is not constant, but decreases with the decrease in the bubble radius (Tolman, 1949). As mentioned in Section 2.1.2, some theoretical models which use this approach predict negative values of surface tension around submicron-sized bubbles (Corti, Kerr, & Torabi, 2011). Besides that, surface tension between water and many gases decreases as the pressure increases (Massoudi & King, 1974). One can conjecture similar behavior of viscosity. For that reason we decided that taking those effects into account might introduce larger error than leaving them out.

Calculations will be given for an air bubble in water, with physical properties given in Table 5.1.

Table 5.1. *Parameters of the system of an air bubble in water used in calculations.*

Speed of sound (water)	c_L	m/s	1481
Density of liquid (water)	ρ_L	kg/m^3	1000
Gas density (air)	ρ_g	kg/m^3	1.2
Vapor pressure (water-air)	p_V	Pa	2300
Constants in Tait equation of state (water)	B	Pa	$3.04 \cdot 10^8$
	n	-	7
Dynamic viscosity (water)	μ	Pa·s	$1 \cdot 10^{-3}$
Surface tension (water-air)	γ	N/m	0.072
Ratio of heat capacities (air)	κ	-	1.4

As already mentioned several times, bubble does not behave in a straightforward manner that would be easy to predict by intuition. It is illustrated in Figure 5.1 for a bubble with the initial radius 5 μm, driven with the pressure amplitude of $p_A = 1.55 p_{atm}$ (Figure 5.1a through Figure 5.1d) and $1.6 p_{atm}$ (Figure 5.1e through Figure 5.1h). A bubble driven with higher p_A reaches somewhat larger maximal radius and, in according to that, lower pressure at that moment. Accordingly, higher velocity of the bubble-liquid interface is reached at the collase (270 m/s in Figure 5.1f versus 200 m/s in Figure 5.1b). Despite all that, the bubble driven with lower p_A reaches smaller radius, producing much higher pressure inside the bubble. Higher pressure in turn creates much higher velocity of the bubble boundary during the first rebound, around 2500 m/s (Figure 5.1b), than approximately 80 m/s when $p_A = 1.6$ atmospheres (Figure 5.1f).

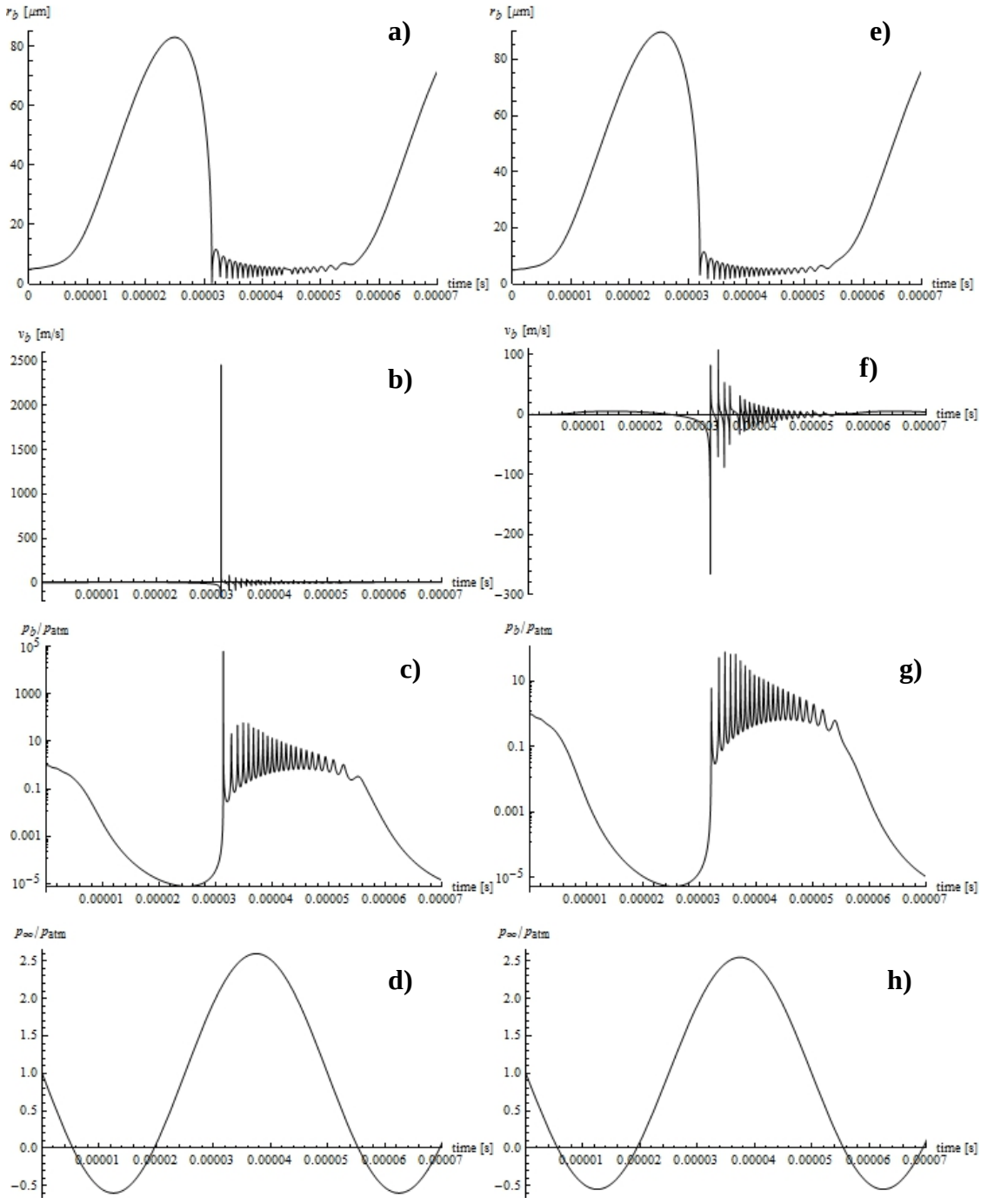

Figure 5.1. Variations of the radius (a, e), velocity (b, f), and pressure at the bubble-water interface (c, g) for a bubble with $r_{b0} = 5\,\mu\text{m}$. Values in frames a) – c) are calculated for an air bubble driven by the pressure with the amplitude $p_A = 1.55\, p_{atm}$ (d), while frames e) – g) are for $p_A = 1.6\, p_{atm}$ (h). The frequency of the pressure change is 20 kHz.

This counterintuitive result illustrates how important is the interplay between the bubble motion and the driving pressure. Further examples are given in Table 5.2. As the initial bubble radius increases, the maximal pressure developed during the collapse varies less and the bubble behaves in a more predictable fashion. However, if the pressure amplitude p_A is too high, a bubble expands too much so its frequency of collapses and rebounds becomes smaller than the frequency of applied pressure. Asynchronous pressure phase decreases the velocity of the bubble boundary, not allowing the bubble to collapse to a small radius and produce high pressure. Zero values in Table 5.2 signify this behavior.

Table 5.2. *Approximate maximal pressures (in atmospheres) which develop around a bubble at its collapse and rebound, as a function of* r_{b0} *and* p_A. *Examples are given for the air bubble – water system and oscillating frequency 20 kHz.*

Pressure amplitude, p_A [atmospheres]	Initial bubble radius, r_{b0} [μm]			
	1	5	10	100
1	1.5	2.1	20	100
1.1	1.6	40	390	160
1.2	1.7	90	280	220
1.3	1.6	250	290	450
1.4	1.7	1800	900	700
1.5	1.8	260	290	900
1.55	1.7	65000	280	1200
1.6	28	80	310	1200
1.8	35	220	670	2200
2.0	0	70	950	2700
2.5	48	100	900	3400
5	0	18	10	13500
10	0	8	15	29000
25	0	0	0	(50)
50	0	0	0	(500)
100	0	0	0	(2500)

Values in brackets signify sporadic occurrence of pressure peaks.

As shown in Table 5.2 the highest pressures are obtained when the initial bubble radius is around 5 μm, and the pressure amplitude is between 1.4 and 1.6 atmospheres. Most of examples found in the literature list r_{b0} and p_A in these ranges. It is also interesting that little attention has been paid on the above discussed cavitation behavior with the changes in p_A. Frequency does not have such an effect and will not be discussed here. Also significant is the choice of equations of state for the liquid and gaseous phases.

Using Eq. 2.3, calculated cavitation thresholds for bubbles in Table 5.2 are: $p_A = 1.39\, p_{atm}$ for $r_{b0} = 1\,\mu\text{m}$ 1 μm, $1.05\, p_{atm}$ for $r_{b0} = 5\,\mu\text{m}$, $1.02\, p_{atm}$ for $r_{b0} = 10\,\mu\text{m}$, and $1.001\, p_{atm}$ for $r_{b0} = 100\,\mu\text{m}$.

5.2. On the Cavitation Zone in the Experimental Setup Used this Work and Other Aspects of the Propagation of Ultrasound in the Liquid Phase

Applying Eq. 2.26 and Eq. 2.27 to estimate acoustic intensity produced in water by the sonotrode S&M 1102 ($r_P = 0.25\,\text{in}$, or 6.35 mm; see Section 3.1) oscillating with the frequency $f = 23280\,\text{Hz}$, one obtains graph shown in Figure 5.2. In an ideal situation without losses, the wavelength of the plane wave can be estimated as $\lambda = c_0 / f$. Since $r_P / \lambda < 1$, in this case $r_P / \lambda \approx 0.1$, the characteristic near-field zone shown in Figure 2.12 is absent, and acoustic intensity drops to negligible value within a short distance from the sonotrode. This means that the liquid heats up only in a thin layer next to the sonotrode (Eq. 2.25), so heating in that zone is quite intensive.

For acoustic intensity along the beam axis, Eq. 2.28 reduces to Eq. 2.26. Assuming $\xi_0 = -\xi_{0A} \sin(2\pi f t)$, where ξ_{0A} is the displacement amplitude of the sonotrode tip, acoustic pressure can be obtained directly from Eq. 2.26:

$$p_a \approx 2\sqrt{2}\pi\rho_0 c f \xi_{0A} \cos(2\pi f t) \sin\left[\frac{\pi}{\lambda}\left(\sqrt{z^2 + r_B^2} - z\right)\right] \qquad \text{Eq. 5.3}$$

This function, with the assumption of $\xi_{0A} = 2.5 \cdot 10^{-6}\,\text{m}$, is shown in Figure 5.3.

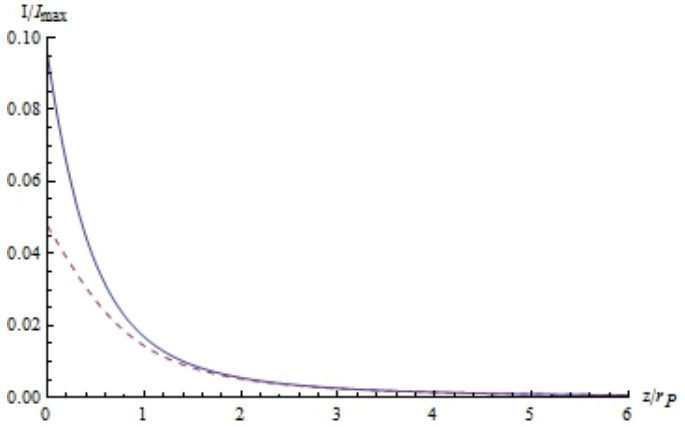

Figure 5.2. Distribution of acoustic intensity along the axis of the sound beam for $\lambda / r_P = 10$. Solid line is I_P defined in Eq. 2.26, and dashed line is I defined in Eq. 2.27.

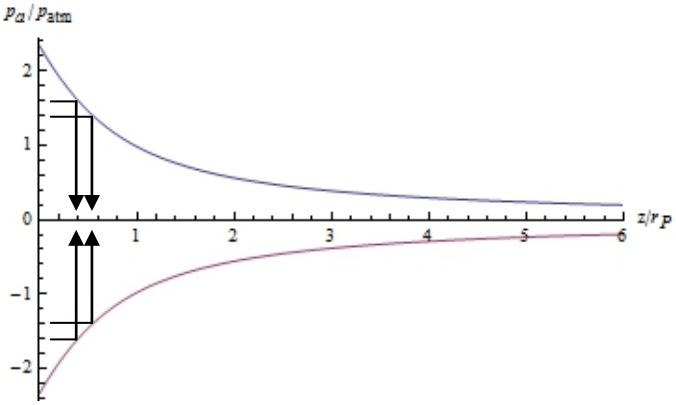

Figure 5.3. Variation of the maximal and minimal acoustic pressure along the sound beam axis, occurring at times which are even-number multiples of $t = 1/f$ and odd-number multiples of $t = 1/(2f)$, respectively. These symmetric curves actually represent the variation of the amplitude of applied pressure field, p_A, the total pressure being $p_\infty = p_{atm} + p_A$. Displacement of the sonotrode tip was assumed to be $\xi_{0A} = 2.5 \cdot 10^{-6}$ m. Arrows show the distance from the sonotrode where p_A is roughly 1.4 to 1.6 atmospheres.

It has been discussed in Section 5.1 that cavitation of micrometer-sized bubbles seems to be strongest when p_A ranges from 1.4 to 1.6 atmospheres. In Figure 5.3 this range of pressures appear at 0.4 to 0.6 of the radius of sonotrode (piston), r_P. According

to this conjecture, cavitation should be strongest in that zone. Indeed, this zone is captured faithfully in Figure 4.10, Figure 4.12 b) and e), and Figure 4.44 b) and c). similar bubbly shell around the sonotrode is visible in all recorded experiments where the duration of ultrasound is long enough for this cloud to form and the supercooling is small so ice does not become immediately visible. For most experiments it took between 0.03 and 0.1 seconds for the cavitation cloud to form. It seems that cavitation really occurs where the amplitude of the acoustic pressure, p_A, is around 1.5 atmospheres. Additional evidence that cavitation occurs mainly at some distance from the sonotrode is absence of the cavitation damage at the surface of the sonotrode, even after it accumulated long time of use.

The shape of the cavitation cloud changes constantly during ultrasonication, as illustrated in Figure 5.4 and Figure 5.5. The cavitation cloud in the first sample (Figure 5.4) becomes very thin after around 0.18 seconds and remains so until the end of ultrasonication which lasted 0.5 seconds. That might be attributed to depletion of larger bubble nuclei so predominantly smaller bubbles[21] are cavitating at higher p_A near the sonotrode. On the other hand, sample in Figure 5.5 had sustained thickness of the cavitation zone, which implies that this sample probably contained much more cavitation nuclei with larger diameter.

A conjecture that cavitation most readily occur when p_A is between 1.4 and 1.6 atmospheres implies that water contains mostly bubbles with radii larger than 0.7 μm.[22]

Simple calculations shown in this section give reasonably good estimations. In order to prove this claim, we will compare the input power from the signal amplifier with the effective power of the ultrasonic field next to the sonotrode. The maximal acoustic intensity can be easily extracted from Eq. 2.26:

---

[21] According to Eq. 2.3, the maximal amplitude of $2.35\, p_{atm}$ shown in Figure 5.3 can cause cavitation of bubbles no smaller than 0.33 μm.

[22] Cavitation threshold for a bubble with $r_{b0} = 0.7\,\mu\text{m}$ is around $p_A = 1.6\, p_{atm}$ (Eq. 2.3).

$$I_{\max} = \left[2\rho_0 c \dot{\xi}_0^2 \right]_{\max} = \left[8\pi^2 \rho_0 c f^2 \xi_{0A}^2 \cos^2 \left(2\pi f t \right) \right]_{\max} = 8\pi^2 \rho_0 c f^2 \xi_{0A}^2 \qquad \text{Eq. 5.4}$$

In our case with $\xi_{0A} = 2.5 \cdot 10^{-6}$ m, one calculates $I_{\max} = 395686$ W / m^2.

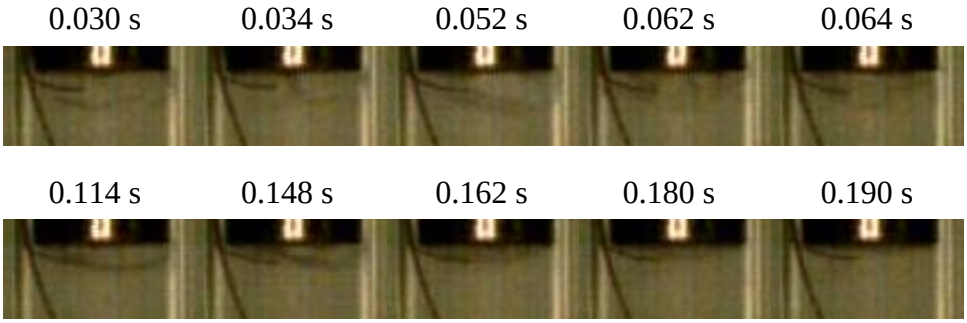

Figure 5.4. Fluctuations of the shape of cavitation cloud. Number of seconds next to each frame denotes time elapsed after the cavitation onset. Ultrasonication lasted 0.5 seconds, and the supercooling was below 2 ºC. The cavitation zone remained thin as shown in the last two frames until the end of ultrasonication. The small thermocouple seems to interfere with the cloud after first two frames. Unfortunately, almost all experiments with water and small supercooling were performed with small thermocouples.

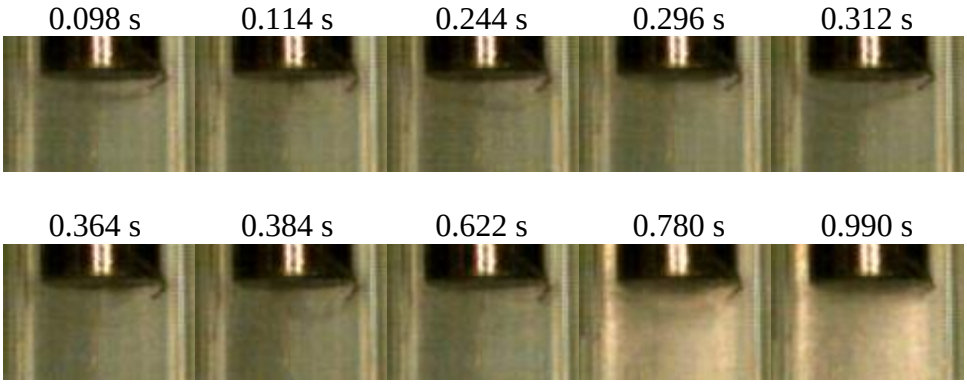

Figure 5.5. Fluctuations of the cavitation cloud. Ultrasonication lasted 1 second and the supercooling was below 2 ºC. The sample was also shown in Figure 4.10 and Figure 4.16 a-d. This time the cavitation zone also become thin several times but succeeded to recover, and even retain its shape with a lot of ice crystallites around (frame at 0.780 seconds after the cavitation onset).

The power irradiated by the sonotrode S&M 1102 is calculated from Eq. 5.4 to be roughly 50.12 W, meaning that not all of the input electric power from the amplifier (120

W) is converted to the energy of the acoustic field. One part of the lost power went on losses in the piezo-crystals, heating them.[23] Some part of the input power probably went on creating and sustaining fractional harmonics, which is discussed next.

As shown in Figure 5.6, the pressure profile in the liquid column is not expected to have oscillatory character, despite periodic drive of the sonotrode. However, some samples shown in the previous chapter exhibit signs of periodic waves in the test tube. More or less bands where first ice forms are visible in Figure 4.25, Figure 4.29, Figure 4.33 b) and c), Figure 4.34. Figure 4.30 and Figure 4.36 show magnified view of appearance of the first band. It should be noted that these bands occurred only at supercooling higher than 3-4 ºC, and not always.

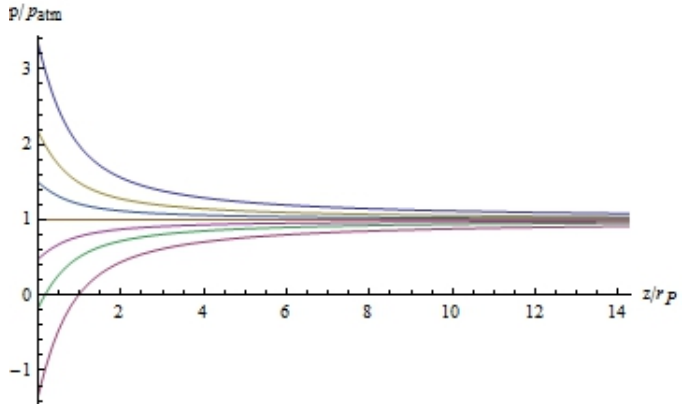

Figure 5.6. Calculated variation of the total pressure along the centerline of the liquid column, the length of which is around 14.3 times the radius of the sonotrode (piston, r_P). Although the sonotrode oscillates in a sinusoidal fashion, the pressure profile does not have that shape. However, the pressure changes between the two bounding pressure profiles in accordance with the main frequency of oscillation.

Formation of bands of primary crystals could occur even in a non-cavitating regime, as shown in Figure 4.36. Formation of ice below cavitation threshold happened because much smaller pressure amplitudes created by bubbles are needed at larger

---

[23] Those piezoelectric crystals used in experiments heat up quickly and need intensive air cooling to prevent their damage.

supercoolings. Figure 5.7 is a schematic of what was observed in Figure 4.30 and Figure 4.36. Bubbles most likely grow around the low-pressure antinode, then hit the container wall and collapsed at higher pressure. It is quite intuitive to expect that increased resistance by higher pressure that acts from below will force bubbles to move sideways, so they eventually hit the wall. The same pattern of motion is expected to happen with small crystals created by cavitation, with the difference that solid particles are more likely to pass through the high-pressure antinode than bubbles are.

When a liquid column experiences variations of resonant frequency, waves with fractional frequencies f_i can appear in addition to original wave with the driving frequency f (Adler & Breazeale, 1970). Actually more than one doublet $f_i + \Delta f_i$ occur around each additional frequency f_i. In our case Δf_i is very small, no more than 50 Hz. The condition for occurrence of fractional harmonics is (Adler & Breazeale, 1970):

$$\frac{\xi_{0A}}{L_0} > \frac{c\alpha}{2\pi f} \qquad \text{Eq. 5.5}$$

where L_0 is the length of the liquid column, and α is the total absorption coefficient of the liquid.

The condition in Eq. 5.5 actually states that the driving signal has to be strong enough so it does not attenuate until it reaches the opposite end of the column. In our case with $\xi_{0A} = 2.5 \cdot 10^{-6}\,\text{m}$, $L_0 \approx 9 \cdot 10^{-2}\,\text{m}$, and α being of the order of $10^{-7}\ \text{m}^{-1}$ (Liebermann, 1948), condition in Eq. 5.5 is satisfied.

In their experiments, Korpel and Adler (1965) observed two additional frequencies, f_1 and f_2, as well as waves with frequencies $|f_1 - f_2|$ and $|2f_1 - f_2|$.

Because the position where bubbles strike the wall is uncertain, as illustrated in Figure 5.7, it was hard to determine what additional frequencies are present in the samples which exibit formation of what seems as periodic bands of first solid crystals. Measuring periods, the most probable candidates are $f/2$, f, $3f/2$, $5f/2$, $7f/2$, and even overtones $2f$ and $4f$. The answer to the most of these possibilities is that additional (idler) frequencies are $f_1 = 3f/2$, $f_2 = f/2$, and their combinations, like

those observed by Korpel and Adler: $f_1 - f_2 = f$, $2f_1 - f_2 = 5f/2$. Other combinations might be imagined, like $f_1 + f_2 = 2f$, or $2f_1 + f_2 = 7f/2$.

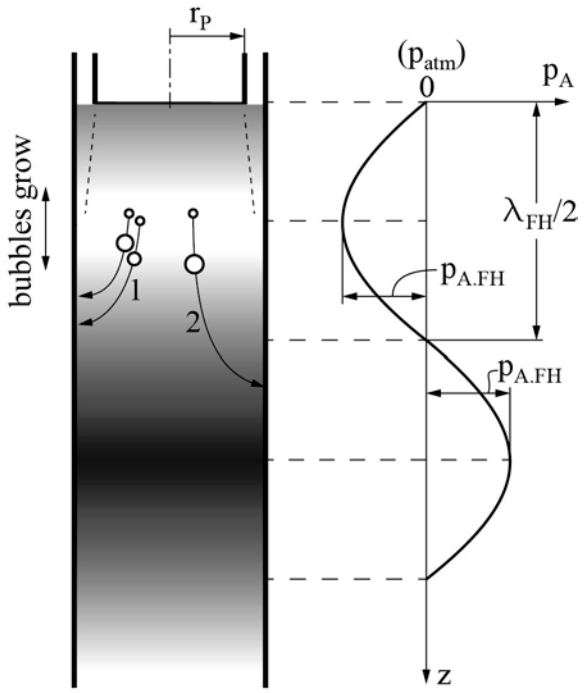

Figure 5.7. The sinusoidal character of the fractional harmonics that is superimposed with the main pressure distribution shown in Figure 5.6. Another difference from the main pressure distribution is that this should be a standing wave. The color intensity in the liquid column represents schematically the pressure amplitude shown on the right side, the darker shades representing higher pressure. Bubbles grow around the pressure antinode, and while pushed down by the pressure field, they gain more lateral component of motion as they penetrate deeper in the region of higher pressure. Most likely bubbles and solid particles reach the test tube wall around the pressure node (path 1) or between the node and the following antinode (path 2).

In our experiments, the length of the liquid column L_0 was not tuned for standing waves,[24] so some of bands that form on the test wall might originate from reflected wave.

[24] L_0 was chosen so the incoming wave is around its pressure node for frequencies around 20 kHz (assuming sinusoidal traveling wave), hoping that this will decrease

Other possibilities is slowly traveling wave, or some uncommon fractions of the driving frequency (e.g. 11/4 or so). Additional problem is that the bottom of the test tube is not flat, which complicates how the waves in the liquid column behave. Also, pressure field can be significantly altered when the sound wave passes through the cavitation zone around the horn; solid particles and formed bands may also add to the complexity of the sound field in the sample. A more detailed work is needed to clarify all these issues.

It can be concluded that oscillations of the bubble at the bottom of the test tube, shown in Figure 4.41, come from the resonation of the liquid column, not from the pure pressure propagation from the sonotrode. From example in Figure 4.36, when applied ultrasound was below the cavitation threshold, one can estimate that pressure amplitudes ($p_{A.FH}$ in Figure 5.7) of fractional harmonics are not negligible. In our experiments they should be around atmospheric pressure, since thay were able to grow larger bubbles. Although radiation pressure due to the driving frequency might not be significant, pressure of fractional harmonics can. Again, this topic needs more wotk, especially since no attention has been paid to this topic, at least to the author's knowledge.

5.3. Influence of Pressure on the Nucleation Rate

Approximate homogeneous nucleation rate is (Eq. 2.40):

$$J = J_0^* \exp\left[-\frac{16\pi}{3} \frac{\sigma_{SL}^3}{\Delta H_f^2 \, \rho_S^2 k_B} \frac{1}{T} \left(\frac{T_{M.p}}{T - T_{M.p}} \right)^2 f(\Theta) \right] \qquad \text{Eq. 5.6}$$

where $J_0^* = 10^{39}$ m^{-3}s^{-1} in Eq. 2.40, and $f(\Theta)$ is calculated from Eq. 2.41. As in Section 2.3.1, we will denote melting temperature at atmospheric pressure as $T_{M.1}$, while the melting point at any other pressure as $T_{M.p}$. An example of nucleation of ice in water is shown in Figure 5.8. Agreement of calculated supercooling for homogeneous nucleation

---

returning wave. The dome-shaped bottom of the test tube is not suitable for standing waves.

in Figure 5.8, 32 to 33 ºC, is in excellent agreement with experimental results from freezing of water droplets with volumes in milliliters (Langham & Mason, 1958; Fletcher, 1970).[25] This is actually no wonder, since physical parameters are determined by fitting accepted theory with experimental measurements. Measured ice-water surface energy reported in the literature ranges from 0.022 to 0.041 J/m^2 (Kloubek, 1974). With $\sigma_{SL} = 0.033\,\mathrm{J/m^2}$, which seems to be used in the literature, estimated supercooling would be around 39 to 40 ºC.[26] That corresponds to nucleation in micrometer-sized bubbles, so we decided to take the value used by Yokoyama et al.

To match Eq. 5.6 with results of our experiments, it was declared that $\Theta = 59.5°$ for heterogeneous nucleation of ice on stainless steel and glass. Then $J \approx 86\,\mathrm{m^{-3}s^{-1}}$ at supercooling of 12 ºC, which leads to 1.3 nuclei in a 15 mL sample of water.[27] A meticulous precision is not so necessary as the same parameters would yield 295000·nuclei in the same volume at only 1 ºC larger supercooling.

Nucleation rate versus supercooling in Figure 5.8 is a classic example for the situation where the diffusion coefficient in the supercooled liquid is not significantly smaller than in the liquid at melting temperature (Frenkel, 1955; Flemings, 1974). In that case the nucleation rate is very sensitive to the level of supercooling; small additional supercoolings beyond that needed for the onset of nucleation increases predicted nucleation rate by many orders of magnitude. Hence we will not take the approach used by Saclier and coworkers (Saclier, Peczalski, & Andrieu, 2010), where the Gilmore model is combined with the classic nucleation theory to find nucleation rate as a function of pressure and supercooling.

---

[25] Figure 4.4 in the book by Fletcher (1970), or Figure 54 in paper by Langham and Mason (1958).

[26] Supercoolings of 63 ºC have been reported for very small bubbles (Hobbs, 1974).

[27] In most of the samples, ice grew from one or two spots, so an average of more than 1 was taken for a 15 mL sample.

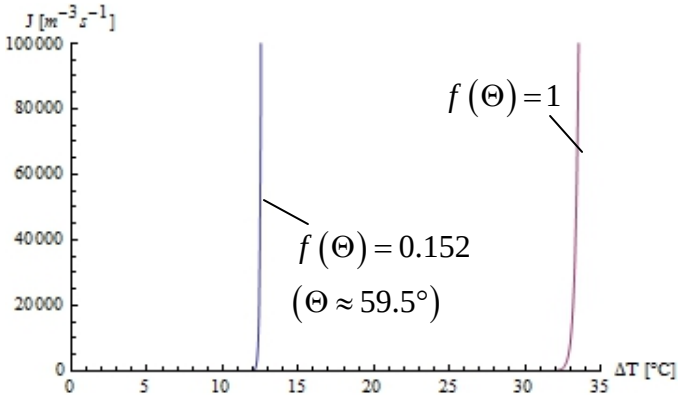

Figure 5.8. Nucleation rate ice in purified water, calculated from Eq. 5.6, where $\Delta H_f = 333.6\,\mathrm{kJ/kg}$, $\sigma_{SL} = 0.028\,\mathrm{J/m^2}$ (Yokoyama, et al., 2011), $k_B = 1.38 \cdot 10^{-23}\,\mathrm{J/K}$, and $\rho_S = 920\,\mathrm{kg/m^3}$. Supercooling for homogeneous nucleation is 32 to 33 ºC. For heterogeneous nucleation it was assumed that $\Theta \approx 60.9°$ to obtain supercooling of 12 to 13 ºC, as observed in experiments.

We first need to consider one property of Eq. 5.6. The term $T_{M.p}^2 / \left(T - T_{M.p}\right)^2$ allows negative supercoolings, i.e. nucleation at $T > T_{M.p}$, and that leads to appearance of fictive results, one example being shown in Figure 5.9. The curves are not symmetric around $T_{M.p}$ due to the $1/T$ term in Eq. 5.6.

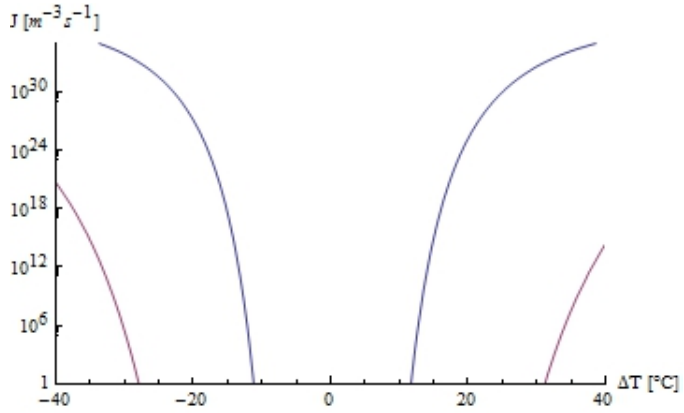

Figure 5.9. Example of solution to Eq. 5.6 for homogeneous nucleation of ice in water at atmospheric pressure. Spurious solutions appear at negative supercoolings.

A problem may occur in our case when we want to examine effects of ultrasound on the supercooling relative to the melting point at atmospheric pressure, $T_{M.1}$. In our case spurious solutions may intrude the range of temperatures below $T_{M.1}$. This is illustrated in Figure 5.10, where appearance of spurious solutions is noticed for pressures above around 50 atmospheres (~ 5 MPa) in case of the nucleation of ice I. Since the melting temperature of ice I decreases with increased pressure (Figure 5.11), so does the supercooling required for nucleation. This is reflected in Figure 5.10. However, when pressures are above 5 MPa, additional solutions appear at small supercoolings, as shown with arrows in Figure 5.10. Hence nucleation rates can be very erroneous when calculated for small supercoolings close to $T_{M.1}$.

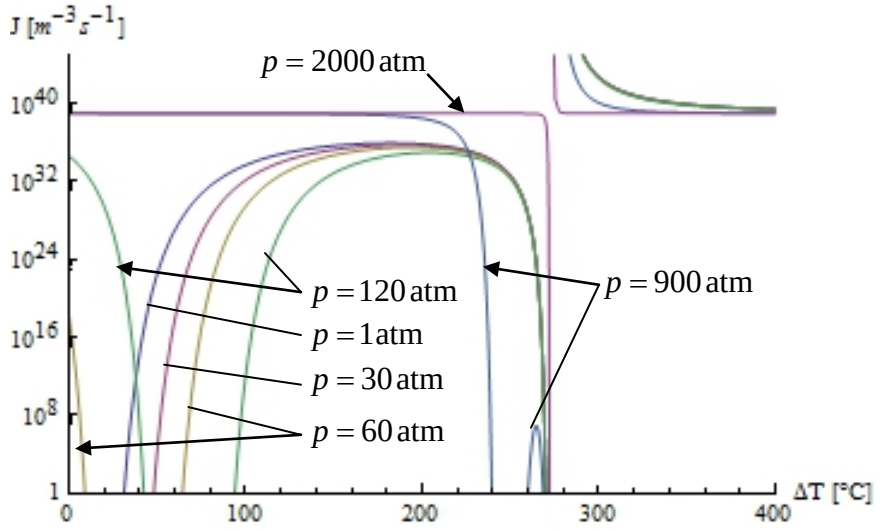

Figure 5.10. Solutions to Eq. 5.6 for homogenous nucleation, with $T_{M.p}$ calculated using Eq. 2.39 and Table 2.1. Pressures 1 to 2000 atmospheres are in the range of nucleating ice I. Spurious solutions, marked with arrows, start to appear at around 50 atmospheres. One also notes nucleation rates of $J \geq 10^{39}$ $m^3 s^{-1}$ at temperatures below absolute zero ($\Delta T > 273.15\,°C$).

In order to avoid the problem of lurking spurious solution, we slightly modify Eq. 5.6 by substituting the negative sign in the exponent with $\left(T - T_{M.p}\right) / \left|T - T_{M.p}\right|$, so Eq. 5.6 takes the following form:

$$J = J_0^* \exp\left[\frac{16\pi\sigma_{SL}^3}{3\Delta H_f^2\,\rho_S^2 k_B}\frac{T_{M.p}^2}{T\left|T-T_{M.p}\right|\left(T-T_{M.p}\right)}f(\Theta)\right] \qquad \text{Eq. 5.7a}$$

$$J < 10^{39}\ \mathrm{m^{-3}s^{-1}} \qquad \text{Eq. 5.7b}$$

$\left|T-T_{M.p}\right|$ is the absolute value of supercooling. Eq. 5.7a gives the same values as the correct solutions to Eq. 5.6. Now, spurious solutions to Eq. 5.7a have values $J \geq 10^{39}\ \mathrm{m^3s^{-1}}$, so it is easy to eliminate them by the condition in Eq. 5.7b. A combination of Eq. 5.7a and Eq. 5.7b is in accordance with Eq. 5.6, since it is obvious that Eq. 5.6 cannot give values larger than $10^{39}\ \mathrm{m^{-3}s^{-1}}$.[28] Solutions to Eq. 5.7a are shown in Figure 5.12.

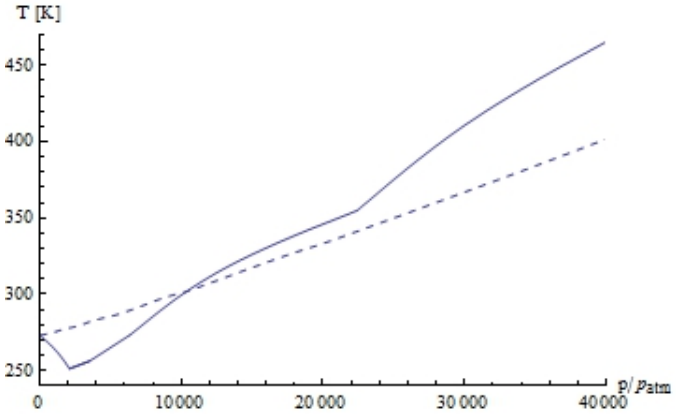

Figure 5.11. Ice-water equilibrium temperatures for pressures up to 40000 atmospheres (~ 4 GPa), represented with solid line, and illustration of adiabatic increase in the temperature of water at those pressures. The ice-water equilibrium was drawn based on the data from AIP Handbook (Gray, 1957). Adiabatic heating (dashed line) was calculated combining Eq. 5.8 and the data from Bridgman (1935) for the specific volume. The result depends significantly on how the data were extrapolated out of the range given by Bridgman. This curve resembles those obtained by Hickling (Hickling R., 1965a; 1994) and Hunt and Jackson (1966b).

---

[28] This value of $J = 10^{39}\ \mathrm{m^{-3}s^{-1}}$ means that nuclei form every 0.001 Angstrom, the distance 1000 times smaller than the diameter of hydrogen atom. Maximal values of J calculated from Eq. 5.6 are several orders of magnitude lower.

As shown in Figure 5.10 and Figure 5.12, ice I cannot nucleate homogeneously by the local increase in pressure – it nucleates thermally at smaller undercoolings. If adiabatic heating is taken into account (Figure 5.11), ice can nucleate only at high pressures, above 1000 MPa. More precisely, it is around 2600 MPa for relatively larger supercoolings and around 2800 MPa for minimal supercoolings (Figure 5.13). This means that only ice VII can nucleate by cavitation (see Table 2.1). Metastable at room temperature, this morphology transforms to ice Ih after nucleation.[29]

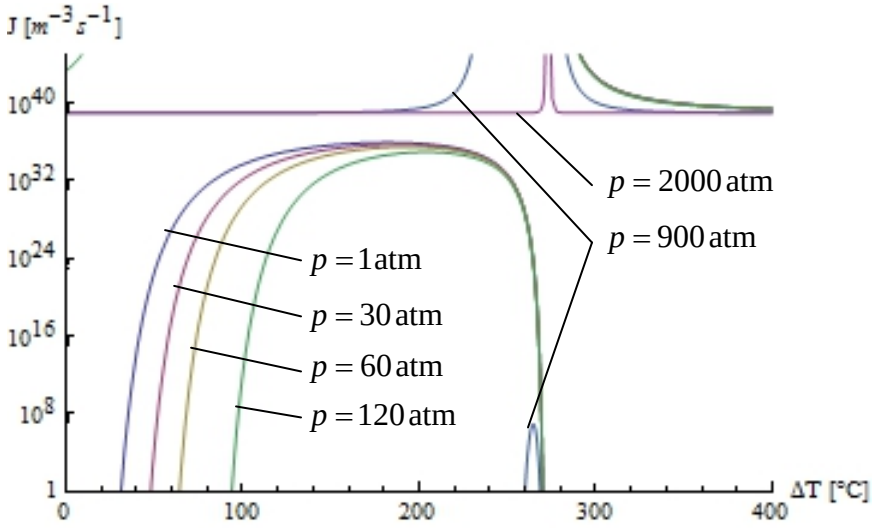

Figure 5.12. Solution to Eq. 5.7a for the same conditions as in Figure 5.10. All correct solutions remain unchanged, while all spurious solutions have values of $J \geq 10^{39}$ $m^{-3}s^{-1}$, placing them in the same range with J at temperatures below absolute zero ($\Delta T > 273.15\,°C$). All these faulty results are eliminated with Eq. 5.7b.

To estimate the potential of ultrasonication to increase the nucleation rate, we calculated only supercooling needed for nucleation, bearing in mind that small additional supercoolings increase that rate by many orders of magnitude. Example in Figure 5.13

---

[29] It seems that nucleation of unstable morphologies of ice are prone to debate, like many theories mentioned in this work. The author has read a report that no ice VI and VII could be detected during solidification; instead only Ih was detected during nucleation. Unfortunately, the author is now unable to find that reference.

clearly shows that it is possible to nucleate solid phase even in superheated liquid. There is no much use from this phenomenon, unless freshly nucleated crystals get in the vicinity of supercooled wall and/or solidification front.

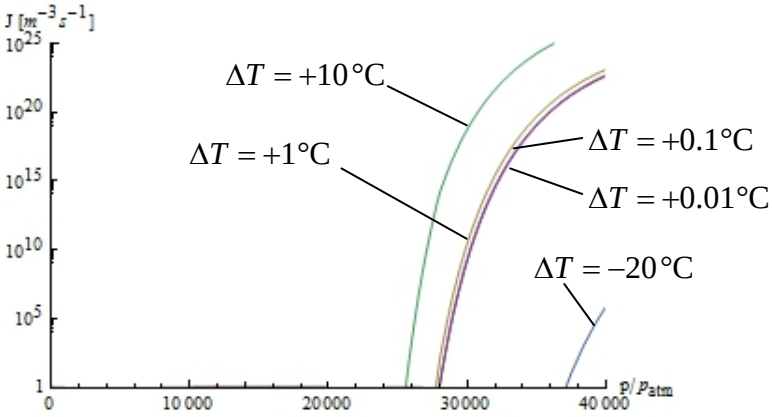

Figure 5.13. The rate of homogeneous nucleation of ice in water as a function of the supercooling (ΔT) and pressure. Calculations were performed combining Eq. 5.7 with data used for calculation of curves in Figure 5.11. Curves for supercoolings of 0.01 and 0.1 ºC are indistinguishable in this plot. For nucleation of ice in water superheated to 20 ºC a local increase in pressure of 37000 atmospheres is necessary.

All the examples in this section have been given for water. One reason is that we used water in majority of experiments presented in Section 4. Water is also a good example because of its complex dependence of meting temperature and pressure (Figure 5.11). This dependence is usually very simple for most metals. For example, melting temperature of aluminum and copper is treated as a linear function of pressure (Table 2.1).

Using definition for adiabatic heating of the liquid phase, for example in AIP Handbook (Gray, 1957), heating of pressurized liquid can be estimated using any of the following relations:

$$\Delta T_{adiab} = \frac{T}{c_p}\left(\frac{\partial \bar{V}_L}{\partial T}\right)_p \Delta p = \frac{T}{c_p}\bar{V}_L \beta_L \Delta p = \frac{T}{c_p \rho_L}\beta_L \Delta p \qquad \text{Eq. 5.8}$$

where c_p is specific heat of the liquid phase at constant pressure, $\bar{V}_L$ specific volume of the liquid phase, and β_L is cubic thermal expansion coefficient of the liquid phase at

constant pressure. We assume the following parameters for aluminum (Gale & Totemeier, 2004): $c_p = 1080\,\mathrm{Jkg^{-1}K^{-1}}$, $\beta_L \approx 1.3\cdot 10^{-4}\,\mathrm{K^{-1}}$, and $\bar{V}_L \approx 1/2700\,\mathrm{m^3/kg}$, neglecting small difference in volumes of liquid and solid phase around melting point. From Eq. 2.39 and Table 2.1, change in the pelting temperature of aluminum is $\Delta T_{M.p} \approx \Delta p/156$. It turns out that $\Delta T_{M.p}/\Delta T_{adiab} \approx 6.4\,^\circ\mathrm{C}/4.5\,^\circ\mathrm{C}$ per 1000 bar (100 MPa) of pressure increase.[30] The net effect is increased supercooling.

By plugging physical parameters for metals in Eq. 5.6, or Eq. 5.7, it is easy to verify that classic nucleation theory does not work well for metals. However, this topic is beyond the scope of this work.

5.4. Further Discussion

Previous three sections, 5.1, 5.2, and 5.3, presented reasonable quantitative estimations of main physical phenomena believed to influence formation of microstructure during solidification. Some aspects of microstructure formation are further discussed in this section.

5.4.1. Grain Refinement

It has been reported in the literature that ultrasonication produces significant grain refinement, as discussed in Sections 1.1, 1.3, and 2.4. Two mechanisms have been recognized as the most influential: increased nucleation rate and dendrite fragmentation.[31] Our observations show that increased nucleation rate is dominant mechanism of grain refinement that always occurs, while dendrite fragmentation can occur only if appropriate conditions are met, as discussed later.

---

[30] This is a very rough estimation since constant value of β_L was used.

[31] Nucleation and dendrite fragmentation are often referred to as primary and secondary nucleation, respectively.

5.4.1.1. Increased Nucleation Rate

Our experiments show that nucleation rate is by far the most influential mechanism of grain refinement. As discussed in Section 5.3, cavitation is capable of increasing the nucleation rate by many orders of magnitude.

It is known that the final grain size is a result of the competition between the nucleation rate and the crystal growth rate. This is exactly what we have observed. The finest ice was observed at minimal supercoolings, which can be seen comparing images of samples in Section 4.3.1 with samples in Sections 4.3.2 and 4.3.3. Observed growth rate in experiments with minimal supercoolings is very slow, slower than predicted by Eq. 2.5, and that is due to the release of latent heat.[32] On the other hand, the nucleation rate in ultrasonicated water is significant at minimal supercoolings and even superheats, as shown in Section 5.3 and Figure 5.13.

Combining very slow growth rate and increased nucleation rate, very fine grains were observed at small supercoolings, see for example Figure 4.16, Figure 4.17, and Figure 4.21. On the other hand, coarse dendrites are visible in the samples held at intermediate levels of supercooling (Figure 4.22, Figure 4.23, and Figure 4.24). These three images are very nice illustrations of the influence of ultrasonication on the grain refinement – the difference in the size of grains grown during ultrasonication and without ultrasound is obvious.

Significance of dispersion of nuclei is shown by much finer structure in Figure 4.25, achieved due to appearance of fractional harmonics. In that way, the structure approached that obtained at supercoolings close to 10 ºC (Section 4.3.3).

Some examples of samples solidified at supercooling close to 10 ºC are shown in Figure 4.33 and Figure 4.38. Those samples were ultrasonicated and had finer structure

---

[32] As per Eq. 2.54, expected growth rate of ice is 0.075 mm/s for $\Delta T = 0.5\,°\mathrm{C}$ and 0.9 mm/s for $\Delta T = 1.5\,°\mathrm{C}$. Much slower growth rate in our experiments is attributed to the release of latent heat, reducing ΔT to negligible values. Practically instant increase in the measured temperature to around 0 ºC is obvious in all cooling curves. Roughly estimating, solidification of around 1.2 % of the volume of water increases temperature in the whole volume by 1 ºC in adiabatic conditions.

than untreated grown sample (Figure 4.35). However, all these samples had coarser structure than spontaneously nucleated sample at supercooling of around 15 ºC (Figure 4.3). [33] Kapustin (1963) made the same conclusion (conclusion 16 in Section 2.4) that application of an ultrasonic field at large supercoolings does not make much difference.

Although dendrites may look finer in Figure 4.3, one might argue that there is most likely much fewer grains in that samples than there is in samples in Figure 4.33 and Figure 4.38.

As discussed in Section 4.3.1, one can obtain fine structure throughout the sample volume with appropriate positioning of the sonotrode. This is illustrated in Figure 4.19 in case of SCN, which is denser and sinks upon solidification, and with the sonotrode positioned at the top of the sample, it was possible to fill the test tube with fine grains. Likewise, the same could be achieved in water if the sample is irradiated from below.

Based on our results, one can conclude that ultrasonication is the most effective at small supercoolings, at temperatures near the melting point at atmospheric pressure. Abramov (1987) reported that the degree of grain refinement decreases when the temperature gradient increases. Since the temperature gradient is proportional to the velocity of the crystal growth and the level of supercooling, this finding agrees with our observation that ultrasonication at small supercoolings achieves best effects.

We did some investigation on the effect of the waveform and did not find any significant difference (Figure 4.21). Between sinusoidal and square, we would still give a slight preference to the sinusoidal waveform due to its continual motion which might cause better agitation.

---

[33] This difference can be attributed to two effects. One effect is smaller dendrite spacing obtained when the supercooling is larger (Eq. 2.56). The other effect is different transparency of ice in samples, sample in Figure 4.3 being obviously more opaque than those shown in Section 4.3.3. All the samples eventually become transparent with time. The opacity of an ice sample depends mostly on the amount of gas dissolved and presence of the interdendritic liquid.

5.4.1.2. Dendrite Fragmentation by Bubbles

Figure 4.39 shows very intensive fragmentation caused by a bubble. On the other hand bubble in Figure 4.40 did not make any visible damage to the dendrites it was in contact with. However, there are some significant differences between these two cases. Firstly, the bubble in Figure 4.39 underwent vigorous oscillations, collapsed and split in two bubbles. High pressure certainly developed during this event. One bubble then penetrated the mushy zone and collapsed there, producing majority of fragments. The fragmentation shown in Figure 4.39 is much more severe than reported previously (Swallowe, Fields, Rees, & Duckworth, 1989; Shu, Sun, Mi, & Grant, 2012).

Vigorous bubble oscillations in Figure 4.39 are due to its vicinity to the sonotrode. This matches with results of Swallowe et al. (Swallowe, Fields, Rees, & Duckworth, 1989), who found that bubbles are very effective if dendrites are close enough to the sonotrode. The bubble in Figure 4.40 was at the bottom of the test tube and it did not oscillate vigorously,[34] because it was driven only with the pressure generated by fractional harmonics.

Another important difference is the solid fraction in the mushy zone, or the thickness of the mushy zone. The mushy zone of SCN samples is expected to be thinner and have better mechanical properties.[35]

We can conclude that bubbles can be effective in dendrite fragmentation if the source of ultrasonic vibrations is close to the mushy zone and if the composition is such that the mushy zone is wider.

---

[34] This conclusion should be taken with caution that the sample is three-dimensional and images do not have good quality, so it is not completely certain how much the bubble was in contact with dendrites.

[35] SCN is generally known for its plasticity.

5.4.1.3. Dendrite Fragmentation by Acoustic Streaming, Radiation Pressure, and Resonation of the Liquid Phase

It is commonly accepted that convection, even forced convection, is not a direct cause of dendrite fragmentation. Instead, by stirring the melt and bringing the melt at higher temperature in contact with dendrites, convection can help constitutional remelting in the roots of dendrite arms, which is considered as the primary mechanism of fragmentation; furthermore, convection transports the fragments away from the mush (Jackson, Hunt, Uhlmann, & Seward, 1966; Paradies, Kim, Glicksman, & Smith, 1993; Pilling & Hellawell, 1996; Paradies, Smith, & Glicksman, 1997). Our observations also indicate that convection (in our case, acoustic streaming) does not cause dendrite fragmentation. Although close to the sonotrode, the dendrite in Figure 4.39 did not fragment until the bubble came in contact with it.

Based on experiments with forced convection, Paradies et al. found that mechanical shearing is not likely the mechanism of dendrite fragmentation, but they did not exclude other mechanical sources (Paradies, Kim, Glicksman, & Smith, 1993; Paradies, Smith, & Glicksman, 1997).

The possibility of fragmenting dendrites with the pressure field has not been reported so far, most likely because it is a “second-order effect”, like acoustic streaming. Indeed, Figure 5.2 and Figure 5.3 indicate that, in our experimental setup, the acoustic pressure decreases to very small magnitudes within the short distance from the sonotrode. Short range of radiation pressure is illustrated in Figure 4.43 to Figure 4.45, when SCN dendrites next to the sonotrode were completely broken while dendrites at the bottom were intact. Even one dendrite in Figure 4.44, positioned at ~ 2/5 of the column length from the sonotrode, was not affected by ultrasound for the first half a second.

Acoustic pressure created by the driving frequency is not likely to cause slow fragmentation of ammonium chloride clusters in Figure 4.42. It is more likely that the pressure created by fractional harmonics did that. Although crystals shifted on the first burst, more significant fragmentation started after six bursts (somewhat over 3 seconds). That happened probably due to initial position of the clusters around pressure nodes. Due to longer delay of fragmentation, remelting cannot be excluded as a contributing factor.

In another experiment, on the other hand, much more defined dendrite of ammonium chloride formed. Dendrite collapsed during the first burst, Figure 5.14, and fragmentation continued progressively on every subsequent burst. However the sonotrode was in slight contact with the test tube so some rubbing occurred during ultrasonication. For that reason this experiment was not included in the results section (Section 4).

As mentioned, calculations predict negligible radiation pressure at the bottom of the test tube. But in some experiments, like that in Figure 4.41, quite measurable pressure oscillations were found. As discussed in Section 5.2, existence of fractional harmonics was due to resonation of the liquid column with frequencies that are fractions of the driving frequency. This led to collection of first crystals in bands in Figure 4.41. Other examples of periodic accumulation of first crystals can be seen in Figure 4.25, Figure 4.33, and Figure 4.34. Resonance could not be observed in all samples, like in samples with immersed thermocouples. The most obvious reason in this case is obstruction of resonance by wires. Resonance was also less noticeable in samples with short duration of ultrasonication (less than 0.1 seconds), or with short duration of bursts.

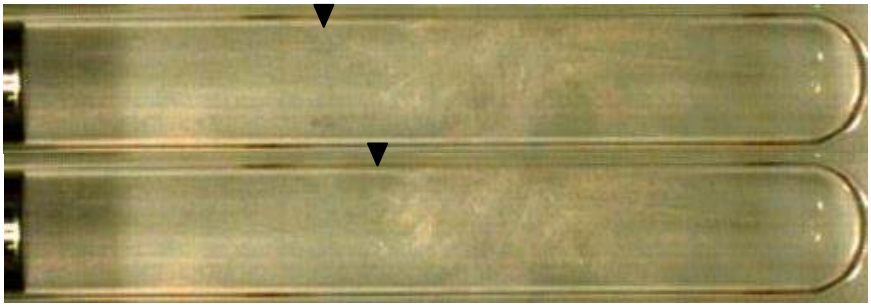

Figure 5.14. Fragmentation of ammonium chloride dendrite. Ultrasound ($A = 600\,\text{mVpp}$) was applied in bursts of 5 Hz and 25% duty cycle. First frame is taken at the onset of the first burst, and the second one at the end of the same burst, 0.05 s later. Arrows indicate the position of the dendrite tip. A big drawback of the experiment is slight rubbing of the sonotrode against the test tube.

The phenomenon of liquid resonance needs further analysis. Due to relatively long time needed for first crystals to become visible, one might argue whether or not resonance did occur in SCN (Figure 4.43 to Figure 4.45) and ammonium chloride (Figure

4.42 and Figure 5.14). Namely, indented layers of dendrites that formed before ultrasonication might be a barrier to resonance. However, judging how bubbles move (e.g. Figure 4.19, Figure 4.20, Figure 4.40, Figure 4.46), there must be varying pressure field throughout the test tube. Since acoustic pressure created by oscillations with the primary frequency quickly vanishes away from the sonotrode (Figure 5.3), it remains that the pressure field should vary with fractional frequencies, as discussed in Section 5.2. One can expect resonance to be especially strong in situations where dendrites grow from the flat surface which is perpendicular to the direction of the sound beam.

According to personal belief, pressure that varies with fractional frequencies should be treated as radiation pressure. From experiments like that shown in Figure 4.41, it is obvious that propagation of this pressure propagates throughout the liquid column since they are developed by resonance. Following analysis in Sections 2.2.1, 2.2.3, and 5.2, significant effects of radiation pressure can be achieved by increasing driving frequency. Example in Figure 5.15 shows predicted acoustic pressure p_a when the driving frequency is ten times the frequency used in our experiments. The pressure amplitude is higher and the propagation depth is longer than shown in Figure 5.3, just on account of ten-fold increase of the frequency (Figure 5.15a). An important benefit is that the length of the cavitation zone is larger. When the radius of sonotrode is doubled (Figure 5.15b) cavitation zone is extended to 7 inches below the sonotrode ($z / r_P = 14$).

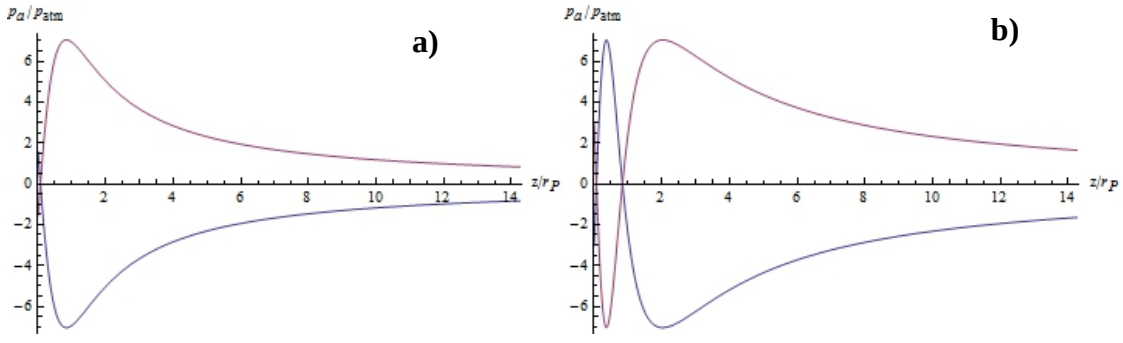

Figure 5.15. Acoustic pressure p_a (Eq. 5.3), for the driving frequency of $f = 232800\,\text{Hz}$, ten times the frequency used in experiments in this work, while the displacement amplitude ξ_{0A} remained the same (2.5 μm). The sonotrode radius, r_P, is a) 1/4 inches (sonotrode S&M1120), and b) 1/2 inches. Pressure distributions with maximal amplitudes are shown.

5.4.1.4. Significance of Bubbles

Bubbles have shown to be the most important feature in the modification of solidifying microstructure by ultrasonication. First of all, they are necessary for cavitation. As mentioned in Section 4.1, cavitation was absent in some experiments when the liquid was previously degassed.[36] A sequence of images in Figure 4.26 shows nucleation of ice by collision of a bubble with the test tube. In Figure 4.29 bubbles even left a trail of ice crystals as they move through the liquid. In both these cases nucleation was most likely heterogeneous, since it happened at the solid body.

Bubbles are especially effective at larger supercoolings. Figure 4.30 and Figure 4.36/Figure 4.37 show nucleation by bubbles in a non-cavitating regime at supercoolings of close to 5 ºC and 10 ºC, respectively.[37]

Another benefit bubbles make is already in mentioned fragmentation of dendrites. Another benefit is agitation of the melt with bubbles pushed by the acoustic field, which was regularly seen in our experiments. It has been observed in experiments that acoustic streaming is always present, even though, theoretically, it should not exist or it should be very small. Grain refinement by agitation of melt with gas bubbles was proposed recently (Wannasin, Martinez, & Flemings, 2006).

5.4.2. On the Possibility to Nucleate Crystals above the Melting Point at Atmospheric Pressure

According to discussion in Section 5.3 and Figure 5.13, it is possible to nucleate ice even when the liquid is superheated. Some cooling curves were shown in Figure 4.10 through Figure 4.13, where a thin layer of water was expected to be slightly above freezing point of water. The thickness of this superheated layer is equal or larger than expected thickness of the cavitation zone. In all these cases ice was nucleated, although in

---

[36] Again, this assertion needs more experimentation to be generalized.

[37] Creation and arresting of these bubbles in the pressure field is discussed in Section 5.2.

smaller amount. The probable reason is that not all nuclei survive passage through superheated zone and simultaneous release of latent heat.

Figure 4.13 shows an example with thicker superheated zone, indicated with the tip of the upper thermocouple (frames b and c). Other than cavitation, no other sources of nucleation have been noticed at such small supercoolings. Small amount of ice crystals that rise from the bottom (Figure 4.13c) were most likely generated below the sonotrode, ejected downwards, and survived passage through superheated zone.

In Figure 4.10 through Figure 4.12 there is sudden temperature drop below sonotrode at the moment when ultrasound is started, as a consequence of mixing. The temperature below the sonotrode jumps down due to small amount of superheated water. On the other hand, there was a significant amount of superheated water below the sonotrode in the sample in Figure 4.13, so the temperature jumps up when warmer liquid is pushed downward towards the thermocouple and mixed with the colder liquid.

With better designed experiments, it would be possible to confirm more clearly that nucleation of ice can start above freezing point.

Experiments were performed where the test tube was immersed only halfway in the crystallizer and exposed part heated with warm air, Figure 5.16 and Figure 5.17. In this experiment, ice was nucleated in the supercooled part of the test tube. There is a great probability that the first nucleation site, marked with arrow in Figure 5.16b, was started by nuclei that came from the cavitation zone below the sonotrode. Of course, there are many other arguments that can oppose this claim. Large number of bubbles nucleated on surfaces in the upper part of the test tube due to elevated temperature. It is also possible that some of these bubbles were pushed down, where they collapsed and nucleated ice. A personal opinion is that it arrival of small nuclei ejected by high pressures is more probable. Again, a better designed experiment is needed to clarify this situation.

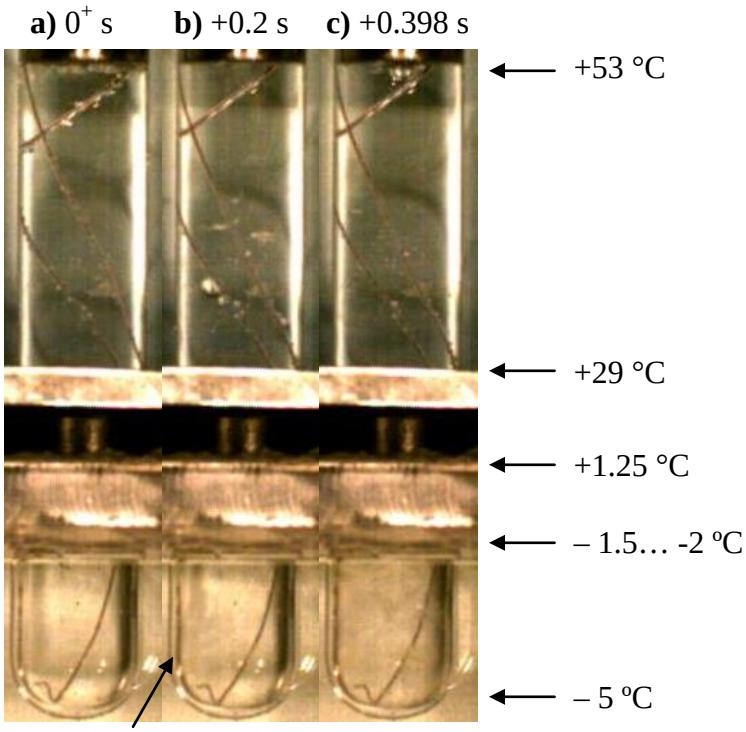

Figure 5.16. Experimental setup where the initial temperature below the sonotrode was around +53 °C, and the temperature at the bottom of the test tube was around – 5 °C. Approximate temperature profile was obtained by moving one thermocouple down the test tube (Figure 5.17). The sample was ultrasonicated for 0.2 seconds with the sine wave of $A = 300\,\text{mVpp}$. Frames were captured at the moment ultrasound started (a), when the ultrasound has just stopped (b), and when ice covered the bottom part of the wall (c). Arrow shows the location of the nucleation site. The temperature of the heat transfer fluid around the test tube was about – 13 °C.

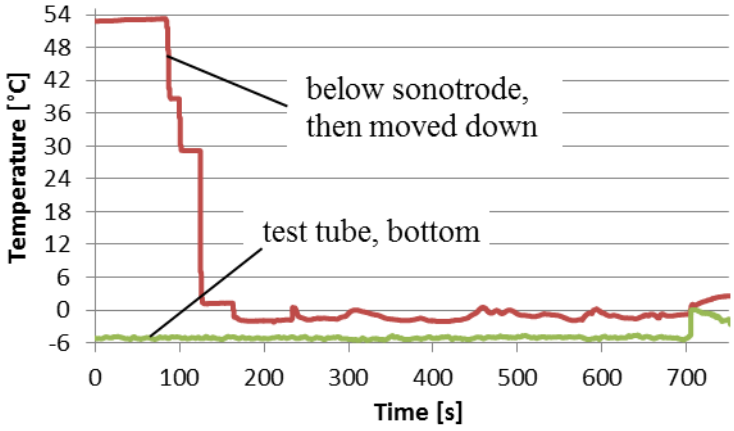

Figure 5.17. Temperature measurements in the experiment shown in Figure 5.16.

5.4.3. Potentially Negative Effects of Ultrasonication

Besides many positive effects of ultrasonication, there are same negative sides which should be taken care of. Two the most important negative effects are overheating and gas entrapment.

Heating of the liquid phase is produced by losses of the acoustic energy. Since ultrasonication is the most effective at very small supercoolings, heating may become very important. Some examples of excessive overheating are shown in Figure 4.18, Figure 4.20, Figure 4.28d, and Figure 4.38.

Ultrasonication has long been recognized as an effective degassing method (Eskin, 1998; Xu, Jian, Meek, & Han, 2004; Xu, Han, & Meek, 2008). However, existence of bubbles around solidifying front always poses a danger of gas entrapment. Hence fragmentation of dendrites by bubbles might turn into formation of a defect. Drastic examples of gas entrapment and some comments are given in Section 4.6. Having high viscosity, SCN samples are prone to gas entrapment. A large number of gas bubbles were regularly observed in SCN samples, like in Figure 4.19 and Figure 4.46, so they can get entangled between growing dendrites, like at the bottom of the sample in Figure 4.20, and stay there (Figure 4.49d).

Gas entrapment can happen in less viscous fluids. One such bubble was captured in Figure 4.36/Figure 4.37 as it was becoming entrapped in the ice nucleated by the same bubble. Entrapment was helped by fractional harmonics that arrested the bubble by the pressure field, so it tended to stay around that position. In other examples, like in Figure 4.30, it is not certain what happens with bubbles which collapse and nucleate ice since they are not visible any more. Similarly, Ohsaka and Trinh (1998) are not absolutely sure about fate of a bubble after it collapses and nucleates ice. They have noticed that, in most cases, a bubble with ice nucleus get ejected from the position where the bubble collapsed to the wall of a container, where ice continues to grow.

5.5. Conclusions

Only main findings discussed in previous sections will be briefly reiterated here. Based on our findings it can be concluded that:

1. Ultrasonication has strong effect on modification of solidifying microstructure.
2. Cavitation-induced nucleation is the most influential factor in grain refinement.
3. Nucleation rate is increased during the collapse and rebound of bubbles. Melting point of pressurized liquid increases more than its temperature increases due to compression. The net effect is increased supercooling, which in turn increases nucleation rate.
4. Ultrasonication at small supercoolings is the most effective for grain refinement.
5. Fragmentation of dendrites is not as strong grain refiner as increased nucleation rate.
6. The most efficient dendrite fragmentation is achieved by bubbles that come in contact with the solid phase and undergo vigorous oscillations.
7. Radiation pressure has not been considered before as a possible contributor to dendrite fragmentation. In our experiments it did not make much effect. However, if high-frequency vibrations and sonotrodes with larger diameters are used, radiation pressure might be a powerful tool in dendrite fragmentation. Experiments are necessary to verify if some not envisioned phenomena arise that could prevent the use of high frequencies in solidification. It is certain that the cavitation zone will be longer.
8. Also not considered before is a phenomenon of resonation of the liquid phase. It creates vibrations with fractional frequencies relative to the driving frequency. These vibrations propagate throughout the liquid and their magnitude can be quite strong.
9. A care must be taken about heating of the liquid by the ultrasonic field, as well as gas entrapment during solidification.

5.6. Recommendations for Future Work

This work hopefully answered some questions, but more surely it opened many. Some of these questions may serve as ideas for future work; there are very ambitious ones, others are not. A brief list of recommendations is given here.

Classical nucleation theory was used in this work since it worked reasonably well for water. However, one can easily verify that it does not work well with pure metals, not to mention alloys or any other complex system. Anisimov (2003) has declared the end of the classical nucleation theory with a reason. However, the author of this work has not been convinced that newer theories are better either, largely because he has not invested enough time to study them. In any way, it is highly recommended to start exploring improved nucleation theories and verify their applicability to metals and their alloys. Otherwise we would have to be contended with qualitative estimations by comparing supercoolings.

As repeated throughout this work, prediction of bubble behavior plays a central role in prediction of effects of ultrasonication. While significant progress has been made in the area of a single bubble dynamics, there is still no model which would explain existence of small stable bubbles. Accordingly, the recommendation is to work on explaining existence of stable bubbles with sizes in the micrometer and sub-micrometer range. The ultimate goal is to be able to estimate the size distribution of bubbles in liquids.

Literature is full of numerical examples for bubbles with the initial radius of 5 μm, driven with the pressure amplitude of 1.4 to 1.6 atmospheres. We also obtained very high pressure at the collapse-rebound moment for the same conditions. As shown, however, not so high pressures are obtained with initial conditions away from the above mentioned range. This is a clear indication that the theory needs to be revisited, at least by studying it more closely to verify that calculations reported in Table 5.2 are not due to instability of numerical solution. According to estimations based on classical nucleation theory, nucleation of ice in water requires pressures of at least 14000 atmospheres, even for supercooling of 10 ºC. Hence most of cavitation events would not develop pressures high enough for nucleation. Contrary to that, experiments presented in this work show

that even small oscillations of bubbles are sufficient to nucleate ice at larger supercoolings. Of course, it is very subjective observation that those bubbles did not undergo larger oscillations or even collapse, especially if there was plenty of time between two frames for such events to occur. It is important that in many of these cases nucleation was most likely heterogeneous when it happened at the walls of the test tube.

One should expect even more problems with the theory of bubble clouds, than with a single bubble. This topic has not been mentioned in this work. To study this phenomenon, one is advised to start with the work of van Wijngaarden (1964) and his later publications. Estimations of the pressure at which solid phase nucleates has been almost exclusively estimated from the the aspect of the collaspe of a single bubble, neglecting effects of the collective collapse. A study of ultrasonication should ultimately adopt analysis of bubble clouds instead of a single bubble.

A study of resonance of liquids seems very interesting phenomenon, and worthwile understanding for successful ultrasonic processing. It could be used both for nucleation and dendrite fragmentation.

Ultrasonication with higher frequencies looks promising for dendrite fragmentation (“secondary nucleation”). Under these conditions radiation pressure is expected to be high enough to cause prolific fragmentation. Experiments are needed to verify this conjecture, since one cannot exclude that some detrimental physical phenomena could become prominent under these conditions. Beside cost, there are maybe other reasons why frequencies of 20 kHz, up to 40 kHz, are mostly used in practice.

A detailed simulation would give a better insight in physical processes that influence nucleation and further growth of the solid phase. Simulations could include the sound field in liquid samples, buble clouds, stresses in growing dendrites, and so on.

It is very advisable to design experiments to determine statistical significance of main parameters of ultrasonic processing. Final verification of the theory has to be performed on metallic samples.

Results obtained using only one crystallized have been presented in this work. Other simple crystallizing cells were made and are available in the laboratory.

Unfortunately, experimental results obtained with them were not suitable for the purpose of this work. Drawings of these crystallizers are given here, so ideas for new crystallizers might come by combining features of their design.

There are many drawbacks in each of the cells shown in Figure 5.18 through Figure 5.20. One of them is inability to control the outside temperature. This is aligned with fogging of the cell if the temperature of the sample is below dew point. With the cell used in this work (Figure 3.1) this problem was solved by heating the outside walls, while the sample was very well protected by the coolant that circulates around the test tube. On the other hand, samples were heated significantly in each of the cells shown in this section.

With steep thermal gradients and slow growth rate, all the cells would actually be better suited for other applications, not the research performed in this work.

There were practical problems to study dendrite fragmentation because it was difficult to cause controlled nucleation before ultrasonication in the cell in Figure 3.1, as discussed previously. The cell in Figure 5.18 was used by placing previously cooled test tube, but with no much success. It is very likely that combination of the cell in Figure 3.1 with those in Figure 5.18 and Figure 5.19 would be successful for this purpose.

Most experiments of the pilot experiments were done using the cell shown in Figure 5.20. Some interesting results were obtained, but they are not pertinent to the topic of this work. Interesting capabilities could be obtained by combining designs of the cell in Figure 3.1 with this one.

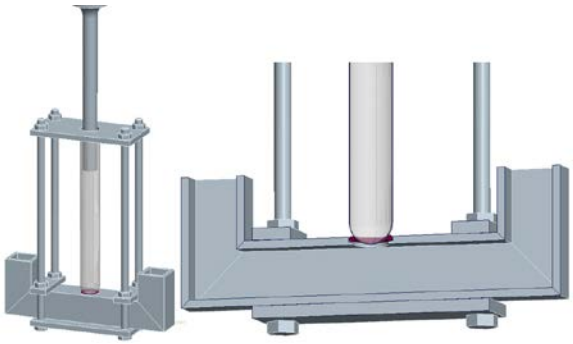

Figure 5.18. Crystallizer for cooling from the bottom of test tube with liquid nitrogen and ultrasonication from the fop.

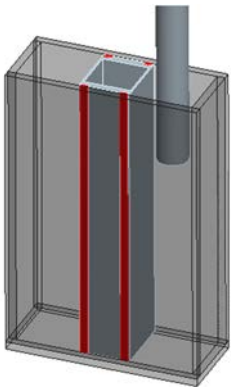

Figure 5.19. Crystallizer initially designed for simultaneous crystallization of ultrasonicated and untreated liquids.

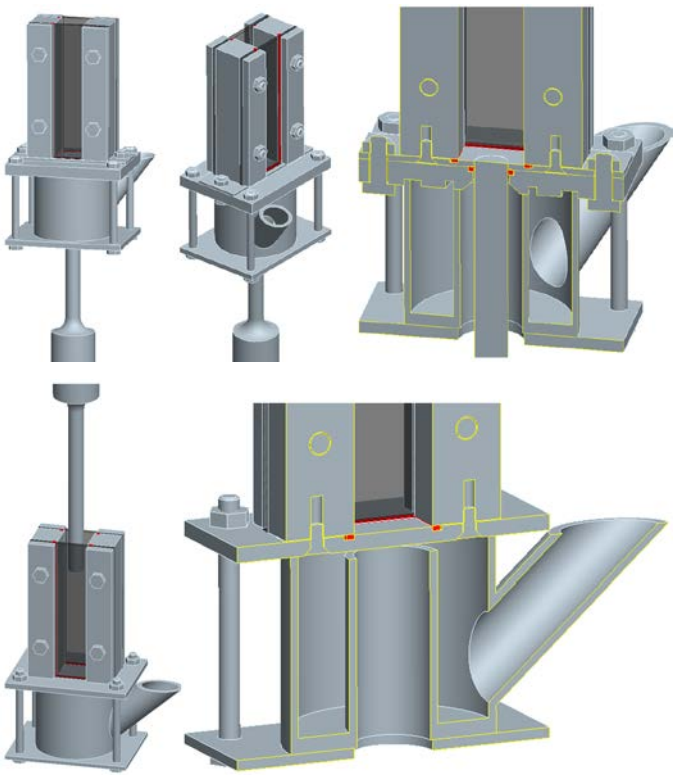

Figure 5.20. Crystallizer cooled with liquid nitrogen from the bottom. The cell is converted to ultrasonication from the bottom and top by changing plates which separate compartments for liquid nitrogen and the sample.

REFERENCES

LIST OF REFERENCES

Abramov, O. V. (1987). Action of High Intensity Ultrasound on Solidifying Metal. *Ultrasonics, 25,* 73-82.

Abramov, O. V. (1998). *High-Intensity Ultrasonics: Theory and Industrial Applications.* Amsterdam: Gordon and Breach Science Publishers.

Abramov, V. O., Abramov, O. V., Straumal, B. B., & Gust, W. (1997). Hypereutectic Al–Si Based Alloys with a Thixotropic Microstructure Produced by Ultrasonic Treatment. *Materials & Design, 18,* 323-326.

Abramov, V., Abramov, O., Bulgakov, V., & Sommer, F. (1998). Solidification of Aluminium Alloys Under Ultrasonic Irradiation Using Water-Cooled Resonator. *Materials Letters, 37,* 27-34.

Adler, L., & Breazeale, M. A. (1970). Generation of Fractional Harmonics in a Resonant Ultrasonic Wave System. *Journal of the Acoustical Society of America, 48,* 1077-1083.

Aghayani, K. M., & Niroumand, B. (2011). Effects of Ultrasonic Treatment on Microstructure and Tensile Strength of AZ91 Magnesium Alloy. *Journal of Alloys and Compounds, 509,* 114-122.

Akulichev, V. A. (1971). Pulsations of Cavitation Voids. In L. D. Rozenberg (Ed.), *High-Intensity Ultrasonic Fileds* (J. S. Wood, Trans., pp. 201-259). New York: Plenum Press.

Anisimov, M. P. (2003). Nucleation: Theory and Experiment. *Russian Chemical Reviews, 72,* 591-628.

Babb, J. S. (1963). Parameters in the Simon Equation Relating Pressure and Melting Temperature. *Reviews of Modern Physics, 35,* 400-413.

Beck, B. V. (1968). Determination of Undisturbed Temperatures from Thermocouple Measurements Using correction Kernels. *Nuclear Engineering and Design, 7*, 9-12.

Beissner, K. (1982). On the Plane-Wave Approximation of Acoustic Intensity. *Journal of the Acoustical Society of America, 71*, 1406-1411.

Beissner, K. (1984). Acoustic Radiation Pressure in the Near Field. *Journal of Sound and Vibration, 93*, 537-548.

Beissner, K. (1986). Two Concepts of Acoustic Radiation Pressure. *Journal of the Acoustical Society of America, 79*, 1610-1612.

Beyer, R. T. (1974). *Nonlinear Acoustics.* Naval Ship Systems Command.

Beyer, R. T. (1978). Radiation Pressure - the History of a Mislabeled Tensor. *Journal of the Acoustical Society of America, 63*, 1025-1030.

Binsbergen, F. L. (1973). Neterogeneous Nucleation of Crystallization. *Progress in Solid State chemistry, 8*, 189-238.

Blake, F. (1949). *The Onset of Cavitation in Liquids.* Boston: Acoustical Reserch Laboratory, Harvard University.

Blander, M. (1979). Bubble Nucleation in Liquids. *Advances in Colloid and Interface Science, 10*, 1-32.

Borkent, B. M., Dammer, S. M., Schoenherr, H., Vancso, G. J., & Lohse, D. (2007). Superstability of Surface Nanobubbles. *Physical Review Letters, 98*, 204502.

Brennen, C. E. (1995). *Cavitation and Bubble Dynamics.* New York: Oxford University Press.

Brenner, M. P., Hilgenfeldt, S., & Lohse, D. (2002). Single-Bubble Sonoluminescence. *Review of Modern Physics, 74*, 425-484.

Bridgman, P. W. (1935). The PressureVolumeTemperature Relations of the Liquid, and the Phase Diagram of Heavy Water. *Journal of Chemical Physics, 3*, 597-605.

Briggs, L. J. (1949). A New Method for Mesuring the Negative Limiting Pressure in Liquids. *Science, 109*, 440.

Briggs, L. J. (1950). Limiting Negative Pressure of Water. *Journal of Applied Physics, 21*, 721-722.

Brillouin, L. (1964). *Tensors in Mechanics and Elasticity.* New York: Academic Press.

Cahn, J. W. (1960). Theory of Crystal Growth and Interface Motion in Crystalline Materials. *Acta Metallurgical, 8*, 554-562.

Cahn, J. W. (1987). The Emergence of Modern Nucleation Theory. In G. S. Cargill, F. Spaepen, & K.-N. Tu (Ed.), *Phase Transitions in Condensed Systems - Experiments and Theory* (pp. 42-55). Pittsburgh: Materials Research Society.

Cahn, J. W., Hilling, W. B., & Sears, G. W. (1964). The Molecular Mechanism of Solidification. *Acta Metallurgica, 12*, 1421-1439.

Campbell, J. (2000). *Castings.* Woburn, MA: Butterworth-Heinemann.

Cantor, B., & Doherty, R. (1979). Heterogeneous Nucleation in Solidifying Alloys. *Acta Metallurgica, 27*, 33-46.

Cha, Y. (1981). On the Equilibrium of Cavitation Nuclei in Liguid-Gas Solution. *Journal of Fluids Engineering, 103*, 425-430.

Chalmers, B. (1964). *Principles os Solidification.* New York: John Wiley & Sons, Inc.

Chow, R., Blindt, R., Chivers, R., & Povey, M. (2003). The Sonocrystallisation of Ice in Sucrose Solutions: Primary and Secondary Nucleation. *Ultrasonics, 41*, 595-604.

Chow, R., Blindt, R., Kamp, A., Grocutt, P., & Chivers, R. (2004). The Microscopic Visualisation of the Sonocrystallisation of Ice Using a Novel Ultrasonic Cold Stage. *Ultrasonic Sonochemistry, 11*, 245-250.

Chow, R., Bloindt, R., Chivers, R., & Povey, M. (2005). A Study on the Primary and Secondary Nucleation of Ice by Power Ultrasound. *Ultrasonics, 43*, 227-230.

Chu, B.-T., & Apfel, R. E. (1982). Acoustic Radiation Pressure Produced by a Beam of Sound. *Journal of the Acoustical Society of America, 72*, 1673-1687.

Chu, B.-T., & Apfel, R. E. (1984). Response to the Comments of Nyborg and Rooney [J. Acoust. Soc. Am. 75, 263-264 (1984)]. *Journal of the Acoustical Society of America, 75*, 1003-1004.

Cole, R. (1974). Boiling Nucleation. *Advances in Heat Transfer, 10*, 85-166.

Cole, R. H. (1948). *Underwater Explosions.* Princeton: Princeton University Press.

Corti, D. S., Kerr, K. J., & Torabi, K. (2011). On the interfacial thermodynamics of nanoscale droplets and bubbles. *Journal of Chemical Physics, 135*, 024701.

Das, A., & Kotadia, H. (2011). Effect of High-Intensity Ultrasonic Irradiation on the Modification of Solidification Microstructure in a Si-rich Hypoeutectic Al–Si Alloy. *Materials Chemistry and Physics, 125*, 853-859.

Das, S., Snoeijer, J. H., & Lohse, D. (2010). *Effect of impurities in description of surface nanobubbles, 82*, 056310.

Dekker, D. L., Piziali, R. L., & Dong, J. E. (1974). Effect of Boundary Conditions on the Ultrasonic-Beam Characteristics of Circular Disks. *Journal of the Acoustical Society of America, 57*, 87-93.

Ducker, W. A. (2009). Contact Angle and Stability of Interfacial Nanobubbles. *Langmuir, 25*, 8907-8910.

Eckart, C. (1948). Vortices and Stremas Caused by Sound Waves. *Physical Review, 73*, 68-76.

Epstein, D., & Keller, J. B. (1972). Expansion and Contraction of Planar, Cylindrical, and Spherical Underwater Gas Bubbles. *Journal of the Acoustical Society of America, 52*, 975-980.

Epstein, P., & Plesset, M. (1950). On the Stability of Gas Bubbles in Liquid-Gas Solutions. *The Journal of Chemical Physics, 18*, 1505-1509.

Epstein, P., & Plesset, M. (1951). Erratum: On the Stability of Gas Bubbles in Liquid-Gas Solutions. *The Journal of Chamical Physics, 19*, 256.

Eriksson, J. C., & Ljunggren, S. (2004). Thermodynamics of Curvad Interfaces in Relation tot the Helfrich Curvature Free Energy. In S. Hartland (Ed.), *Surface and Interfacial Tension* (pp. 547-614). New York: Marcel Dekker.

Eskin, G. I. (1994). Influence of Cavitation Treatment of Melts on the Processes of Nucleation and Growth of Crystals during Solidification of Ingots and Castings from Light Alloys. *Ultrasonic Sonochemistry, 1*, S59-S63.

Eskin, G. I. (1998). Properties of Ultrasonic (Cavitational) Treatment of the Melt in the Manufacture of Aluminum Alloy Products. *Metallurgist, 42*, 284-291.

Eskin, G. I. (2001). Broad Prospects for Commercial Application of the Ultrasonic (Cavitation) Melt Treatment of Light Alloys. *Ultrasonic Sonochemistry, 8*, 319-325.

Fermi, E. (1956). *Thermodynamics.* New York: Dover Publications, Inc.

Fisher, J. C., Hollomon, J. H., & Turnbull, D. (1948). Nucleation. *Journal of Applied Physics, 19*, 775-784.

Fisher, J. C., Hollomon, J. H., & Turnbull, D. (1949). Rate of Nucleation of Solid Particles in a Subcooled Liquid. *Science, 109*(2825), 168-169.

Flemings, M. C. (1974). *Solidification Processing.* New York: Mc-Graw-Hill.

Fletcher, N. (1970). *The Chemical Physics of Ice.* Cambridge: Cambridge University Press.

Fox, F. E., & Herzfeld, K. F. (1954). Gas Bubbles with Organic Skin as Cavitation Nuclei. *Journal of the Acoustic Society of America, 26*, 983-989.

Franc, J.-P., & Michel, J.-M. (2004). *Fundamentals of Cavitation.* Boston: Kluwer Academic Publishers.

Frenkel, Y. I. (1955). *Kinetic Theory of Liquids.* New York: Dover Publications.

Fujikawa, S., & Akamatsu, T. (1980). Effects of the Non-Equilibrium Condensation of Vapour on the Pressure Wave Produced by the Collapse of a Bubble in a Liquid. *Journal of Fluid Mechanics, 97*, 481-512.

Gaitan, D. F., Crum, L. A., Church, C. C., & Roy, R. A. (1992). Sonoluminescence and Bubble Dynamics for a Single, Stable, Cavitating Bubble. *Journal of the Acoustical Society of America, 91*, 3166-3183.

Gale, W. F., & Totemeier, T. C. (Eds.). (2004). *Smithells Metals Reference Book* (8 ed.). Burlington: Elsevier Butterworth-Heinemann, The Materials Information Society.

Gibbs, J. W. (1906). *The Scientific Papers of J. Willard Gibbs, Volume One: Thermodynamics.* Woodbridge: Ox Bow Press.

Gilmore, F. R. (1952). *The Growth and Collapse of a Single Bubble in a Viscous Compressible Fluid. Report No. 26-4.* California Institute of Technology, Hydrodynamics Laboratory, Pasadena.

Glicksman, M. E. (2011). *Principles of Solidification.* New York: Springer.

Glicksman, M. E., & Selleck, M. E. (1987). Crystal Growth Mechanisms and Kinetics. In G. S. Cargill, F. Spaepen, & K.-N. Tu (Ed.), *Phase Transitions in Condensed Systems - Experiments and Theory* (pp. 433-449). Pittsburgh: Materials Research Society.

Glicksman, M. E., Schaefer, R. J., & Ayers, J. D. (1976). Dendritic Growth-A Test of Theory. *Metallurgical Transactions A, 7A*, 1747-1759.

Gray, D. E. (Ed.). (1957). *American Institute of Physics Handbook.* New York: McGraw-Hill.

Greene, C. H., & Gaffney, R. F. (1959). Apparatus for Measuring the Rate of Absorption of a Bubble in Glass. *Journal of the American Cheramic Society, 42*, 271-275.

Greenspan, M. (1979). Piston Radiator: Some Extensions of the Theory. *Journal of the Acoustucal Society of America, 65*, 608-621.

Greer, A., Bunn, A., Tronche, A., Evans, P., & Bristow, D. (2000). Modelling of Inoculation of Metallic Melts: Application to Grain Refiniment of Aluminum by Al-Ti-B. *Acta Materialia, 48*, 2823-2835.

Harvey, E. N., Barnes, D., McElroy, W., Whitelty, A., Pease, D., & Cooper, K. (1944a). Bubble Formation in Animals, I. Physical Factors. *Journal of Cellular and Comparative Physiology, 24*, 1-22.

Harvey, E. N., McElroy, W., & Whitelty, A. (1947). On the Cavity Formation in Water. *Journal of Applied Physics, 18*, 162-172.

Harvey, E. N., Whitelty, A., McElroy, W., Pease, D., & Barnes, D. (1944b). Bubble Formation in Animals, II. Gas Nuclei and Their Distribution in Blood and Tissues. *Journal of Cellular and Comparative Physiology, 24*, 23-34.

Hecht, U., Granasyb, L., Pusztaib, T., Boettger, B., Apel, M., Witusiewicz, V., . . . Rex, S. (2004). Multiphase Solidification in Multicomponent Alloys. *Materials Science and Engineering R, 46*, 1-49.

Heidemann, E. A. (1954). Metallurgical Effects of Ultrasonic Waves. *Journal of the Acoustical Society of America, 26*, 831-842.

Hickling, R. (1965a). Nucleation of Freezing by Cavity Collapse and its Relation to Cavity Damage. *Nature, 206*, 915-917.

Hickling, R. (1965b). Nucleation of Freezing by Cavity Sub-cooled Bismuth and Gallium. *Nature, 207*, 742.

Hickling, R. (1994). Transient, High-Pressure Solidification Associated with Cavitation in Water. *Physical Review Letters, 73*, 2853-2856.

Hickling, R., & Plesset, M. S. (1964). Collapse and Rebound of a Spherical Bubble in Water. *Physics of Fluids, 7*, 7-14.

Hobbs, P. V. (1974). *Ice Physics.* Oxford: Claredon Press.

Hollomon, J. H. (1953). Nucleation. *Progress in Metal Physics, 4*, 333-388.

Holzfuss, J., Rüggeberg, M., & Billo, A. (1998). Shock Wave Emissions of a Sonoluminescing Bubble. *Physical Review Letters, 81*, 5434-5437.

Hunt, J., & Jackson, K. (1966a). Nucleation of the Solid Phase in an Undercooled Liquid by Cavitation. *Journal of Applied Physics, 37*, 254-257.

Hunt, J., & Jackson, K. (1966b). Nucleation of the Solid Phase by Cavitation in an Undercooled Liquid which Expands on Freezing. *Nature, 211*, 1080-1081.

Inada, T., Zhang, X., Yabe, A., & Kozawa, Y. (2001). Active Control of Phase Change from Supercooled Warter to Ice by Ultrasonic Vibration 1. Control of Freezing Temperature. *International Journal of Heat and Mass Transfer, 44*, 4523-4531.

Ivany, R. D., & Hammit, F. G. (1965). Cavitation Bubble Collapse in Viscous,. *Compressible Liquids—Numerical Analysis, 87*, 977-985.

Jackson, K. A. (1958). Interface Structure. In R. H. Doremus, B. W. Roberts, & D. Turnbull (Ed.), *Growth and Perfection of Crystals* (pp. 319-324). New York: John Wiley & Sons.

Jackson, K. A., & Hunt, J. D. (1965). Transparent Compounds That Freeze Like Metals. *Acta Metallurgica, 13*, 1212-1215.

Jackson, K. A., Hunt, J. D., Uhlmann, D. R., & Seward, I. T. (1966). On the Origin of the Equiaxed Zone in Castings. *Transactions of the Metallurgical Society of AIME, 236*, 149-158.

Jian, X., Meek, T., & Han, Q. (2006). Refinement of Eutectic Silicon Phase of Aluminum A356 Alloy Using High-Intensity Ultrasonic Vibration. *Scripta Materialia, 54*, 893-896.

Jian, X., Xu, H., Meek, T., & Han, Q. (2005). Effect of Power Ultrasound on Solidification of A356 Alloy. *Materials Letters, 59*, 190-193.

Johnson, B. D., & Cooke, R. C. (1981). Generation of Stabilized Microbubbles in Seawater. *Science, 213*, 209-211.

Kapustin, A. (1963). *The Effect of Ultrasound on the Kinetics of Crystallization (Authorized translation from the Russian).* New York: Consultants Bureau.

Keller, J. B., & Kolodner, I. I. (1956). Damping of underwater explosion bubble oscillations. *Journal of Applied Physics, 27*, 1152-1161.

Keller, J. B., & Miksis, M. (1980). Bubble oscillations of large amplitude. *Journal of the Acoustical Society of America, 68*, 628-633.

Kinsler, L. E., & Frey, A. R. (1950). *Fundamentals of Acoustics.* New York: Wiley.

Kirkwood, J. G., & Bethe, H. A. (1942). *The Pressure Wave Produced by an Underwater Explosion. Report No. 588.* Office of Scientific Research and Development.

Kloek, W., van Vliet, T., & Meinders, M. (2001). Effects of Bulk and Interfacila Rheological Properties on Bubble Dissolution. *Journal of Colloid and Interface Science, 237*, 158-166.

Kloubek, J. (1974). Calculation of Surface Free Energy Components of Ice According to Its Wettability by Water, Chlorobenzene, and and Carbon Disulfide. *Journal of Colloid and Interface Science, 46*, 185-190.

Korpel, A., & Adler, R. (1965). Parametric Phenomena Observed on Ultrasonic Waves in Water. *Applied Physics Letters, 7*, 106-108.

Kreyszig, E. (2006). *Advanced Engineering Mathematics* (9th Edition ed.). Hoboken: John Wiley & Sons, Inc.

Kurz, W., & Fisher, D. (1998). *Fundamentals of Solidification.* Enfield, NH: Trans Tech Publications Inc.

Langham, E. J., & Mason, B. J. (1958). The Heterogeneous and Homogeneous Nucleation of Supercooled Water. *Proceedings of the Royal Society of London. Series A, Mathematical and Physical Sciences, 247*, 493-504.

Lee, C. P., & Wang, T. G. (1993). Acoustic Radiation Pressure. *Journal of the Acoustical Society of America, 64*, 1099-1109.

Leighton, T. G. (1994). *The Acoustic Bubble.* London: Academic Press.

Lezzi, A., & Prosperetti, A. (1987). Bubble Dynamics in a Compressible Liquid. Part 2. Second-Order Theory. *Journal of Fluid Dynamics, 187*, 289-321.

Liebermann, L. (1957). Air Bubbles in Water. *Journal of Applied Physics, 28*, 205-211.

Liebermann, L. N. (1948). The Origin of Sound Absorption in Water and in Sea Water. *Journal of the Acoustical Society of America, 20,* 868-873.

Liebermann, L. N. (1949). The Second Viscosity of Liquids. *Physical Review, 75*, 1415-1425.

Lighthill, S. J. (1978). Acoustic Streaming. *Journal of Sound and Vibrations, 61*, 391-418.

Liu, S., & Hellawell, A. (1999). Experiments with Constrained Chimney-Plume Flows in the System Ammonium Chloride-Water: Comparison with the Unconstrained Case. *Journal of Fluid Mechanics, 388*, 21-48.

Löfstedt, R., Weninger, K., Putterman, S., & Barber, B. P. (1995). Sonoluminescing bubbles and mass diffusion. *Physical Review E, 51*, 4400-4410.

Lubetkin, S. D. (2004). Bubble Nucleation and Detachment. In S. Hartland (Ed.), *Surface and Interfacial Tension: Measurement, Theory, and Applications* (pp. 483-546). New York: Marcel Dekker, Inc.

Massoudi, R., & King, A. (1974). Effect of Pressure on the Surface Tension of Water. Adsorbtion of Low Molecular Weight Gasses on Water at 25 Degrees. *Journal of Physical Chemistry, 78,* 2262-2266.

Massoudi, R., & King, A. J. (1974). Effect of Pressure on the Surface Tension of Water. Adsorbtion of Low Molecular Weight Gasses on Water at 25 Degrees. *Journal of Physical Chemistry, 78,* 2262-2266.

Mastikhin, I., & Newling, B. (2008). Dynamics of dissolved gas in a cavitating fluid. *Physical Review E, 78*, 066316.

Matula, T. J. (1999). Inertial Cavitation and Single-Bubble Sonoluminescence. *Philosophical Transactions: Mathematical, Physical and Engineering Sciences, 357*, 225-249.

Melia, T. P. (1965). Crystal Nucleation from Aqueous Solution. *Journal of Applied Chemistry, 15*, 345-357.

Mori, Y., Hijikata, K., & Nagatani, T. (1977). Fundamental Study of Bubble Dissolution in Liquid. *International Journal of Heat and Mass Transfer, 20,* 41-50.

Nastac, L. (1999). Numerical Modeling of Solidification Morphologies and Segregation Patterns in Cast Dendritic Alloys. *Acta Materialia, 47*, 4263-4262.

Nastac, L. (2011). Mathematical Modeling of the Solidification Structure Evolution in the Presence of Ultrasonic Stirring. *Metallurgical and Materials Transactions B, 42B*, 1297-1305.

National Instruments. (2012). *NI FP-TC-120 Data Sheet.* Retrieved from www.ni.com: http://www.ni.com/pdf/products/us/4dio556_558.pdf

Neppiras, E., & Noltingk, B. (1951). Cavitation Produced by Ultrasonics: Theoretical Conditions for the Onset of Cavitation. *Proceedings of the Physical Society B, 64*, 1032-1038.

Noltingk, B., & Neppiras, E. (1950). Cavitation Produced by Ultrasonics. *Proceedings of the Physical Society B, 63*, 674-685.

Nyborg, W. L. (1981). Heat Generation by Ultrasound in a Relaxing Medium. *Journal of the Acoustical Society of America, 70*, 310-312.

Nyborg, W. L. (n.d.). Acoustic Streaming due to Attenuated Plane Waves. *Journal of the Acoustical Society of America, 25*, 68-75.

Nyborg, W. L., & Rooney, J. A. (1984). Comments on "Acoustic radiation pressure produced by a beam of sound" [J. Acoust. Soc. Am. 72, 1673-1687 (1982)]. *Journal of the Acoustical Society of America, 75*, 263-264.

O'Hern, T., d'Agostino, L., & Acosta, A. (1988). Comparison of Holographic and Coulter Counter Measurements of Cavitation Nuclei in the Ocean. *Journal of Fluids Engineering, 27*, 200-207.

Ohsaka, K., & Trinh, E. H. (1998). Dynamic Nucleation of Ice Induced by a Single Stable Cavitation Bubble. *Applied Physics Letters, 73*, 129-131.

Paradies, C., Kim, G., Glicksman, M., & Smith, R. (1993). The Effects of Varying Melt Flow Velocity on the Grain Fragmentation in a Mushy Zone. *Light Metals* (pp. 779-782). The Minerals, Metals & Materials Society.

Paradies, C., Smith, R., & Glicksman, M. (1997). The Influence of Convection during Solidification on Fragmentation of the Mushy Zone of a Model Alloy. *Metallurgical and Materials Transactions A, 28A*, 875-883.

Pilling, J., & Hellawell, A. (1996). Mechanical Deformation of Dendrites by Fluid Flow. *Metallurgical and Materials Transaction A, 27A*, 229-232.

Plesset, M. S. (1949). The Dynamics of Cavitation Bubbles. *Journal of Applied Mechanics, 71*, 277-282.

Plesset, M. S., & Prosperetti, A. (1977). Bubble Dynamics and Cavitation. *The Annual Review of Fluid Mechanics, 9*, 145-185.

Poritsky, H. (1952). The collapse or growth of a spherical bubble or cavity in a viscous fluid. In E. Stemberg (Ed.), *Proceedings of the First U.S. National Conference in Applied Mathematics, June 11-16, 1951, Illinois Institute of Technology, Chicago, IL* (pp. 813-821). New York: ASME.

Prosperetti, A., & Lezzi, A. (1986). Bubble Dynamics in a Compressible Liquid. Part 1. First-Order Theory. *Journal of Fluid Mechanics, 168*, 457-468.

Pruppacher, H. R. (1967). Interpretation of Experimentally Determined Growth Rates of Ice Crystals in Supercooled Water. *Journal of Chemical Physics, 47*, 1807-1813.

Puga, H., Barbosa, J., Costa, S., Ribeiro, S., Pinto, A., & Prokic, M. (2013). Influence of Indirect Ultrasonic Vibration on the Microstructure and Mechanical Behavior of Al–Si–Cu Alloy. *Materials Science&EngineeringA, 560*, 589-595.

Qian, M., Ramirez, A., & Das, A. (2009). Ultrasonic Refinement of Magnesium by Cavitation:Clarifying the Role of wall Crystals. *Journal of CrystalGrowth, 311*, 3708-3715.

Qian, M., Ramirez, A., Das, A., & StJohn, D. (2010). The Effect of Solute on Ultrasonic Grain Refinement of Magnesium Alloys. *Journal of Crystal Growth, 312*, 2267-2272.

Rayleigh, J. W. (1917). On the Pressure Developed in a Liquid during the Collapse of a Spherical Cavity. *Philosophical Magazine, 34*, 94-98.

Rayleigh, J. W. (1945a). *The Theory of Sound* (Vol. One). New York: Dover Publications.

Rayleigh, J. W. (1945b). *The Theory of Sound* (Vol. Two). New York: Dover Publications.

Richards, W. T., & Loomis, A. L. (1927). The Chemical Effects of High Frequency Sound Waves 1. A Preliminary Survay. *Journal of the Chemical Society of America, 49*, 1086-1100.

Russell, K. C. (1980). Nucleation in Solids: The Induction and Steady State Effects. *Advances in CoIloid and Interface Science, 13*, 205-318.

Saclier, M., Peczalski, R., & Andrieu, J. (2010). A Theoretical Model for Ice Primary Nucleation Induced by Acoustic Cavitation. *Ultrasonics Sonochemistry, 17*, 98-105.

Satyamurthu, P., Marwah, R. K., Venkatramani, N., & Rohatgi, R. K. (1979). Estimation of Error in Steady-State Measurement Due to Conduction Along Thermocouple Leads. *International Journal of Heat and Mass Transfer, 22*, 1151-1154.

Shah, Y., Pandit, A., & Moholkar, V. (1999). *Cavitation Reaction Engineering.* New York: Kluwer Academic / Plenum Publishers.

Shepelev, D., Oshri, G., Graznov, P. G.-M., Moldavsky, L., Shuster, K., Fichman, M., & Bamberger, M. (2008). Ultrasonic Induced Structural Modification in Mg Alloys. *Materials Science and Technology, 24*, 1293-1298.

Shu, D., Sun, B., Mi, J., & Grant, P. A. (2012). A High-Speed Imaging and Modeling Study of Dendrite Fragmentation Caused by Ultrasonic Cavitation. *Metallurgical and Materials Transaction A, 41A*, 3755-3766.

Simon, V. F., & Glatzel, G. (1929). Bernerkungen zur Schmelzdruckkurve. *Zeitschrift für anorganische und allgemeine Chemie, 178*, 309-316.

Singh, B. S., & Dybbs, A. (1976). Error in Temperature Measurements Due to Conduction Along the Sensor Leads. *Journal of Heat Transfer, 98*, 491-495.

Sirotyuk, M. G. (1971). Experimental Investigations of Ultrasonic Cavitation. In L. D. Rozenberg (Ed.), *High-Intensity Ultrasonic Fields* (J. S. Wood, Trans., pp. 261-343). New York: Plenum Press.

Southin, R., & Chadwick, G. (1978). Heterogeneous Nucleation in Solidifying Metals. *Acta Materialia, 26*, 223-231.

Stefanescu, D. M. (2009). *Science and Engineering of Casting Solidification* (Second ed.). New York: Springer.

Swallowe, G. M., Fields, J. E., Rees, C. S., & Duckworth, A. (1989). A Photographic Study of the Effect of Ultrasound on Solidification. *Acta Metallurgica, 37*, 961-967.

Tan, F. L. (2009). Solidification of Binary Alloy in a Finned Enclosure from the Bottom. *Heat and Mass Transfer, 45*, 255-262.

Thompson, C. V., & Spaepen, F. (1983). Homogeneous Crystal Nucleation in Binary Metallic Alloys. *Acta Metallurgica, 31*, 2021-2027.

Tolman, R. C. (1949). The Effect of Droplet Size on Surface Tension. *Journal of Chemical Physics, 17*, 333-337.

Tomita, Y., & Shima, A. (n.d.). On the Behavior of a Spherical Gas Bubble and Impulse Pressure in a Viscous Compressible Liquid. *Bulletin of the Japan Society of Mechanical Engineers, 20*, 1453-1460.

Trilling, L. (1952). The Collapse and Rebound of a Gas Bubble. *Journal of Applied Physics, 23*, 14-17.

Turnbull, D. (1950a). Kinetics of Heterogeneous Nucleation. *Journal of Chemical Physics, 18*, 198-203.

Turnbull, D. (1950b). Formation of Crystal Nuclei in Liquid Metals. *Journal of Applied Physics, 21*, 1022-1028.

Turnbull, D., & Fisher, J. (1949). Rate of Nucleation in Condensed Systems. *Journal of Chemical Physics, 17*, 71-73.

van Wijngaarden, L. (1964). On the Collective Collapse of a Large Number of Bubbles in Water. *Proceedings of the Eleventh International Congress of Applied Mechanics Munich (Germany) 1964* (pp. 854-861). Berlin: Springer-Verlag.

Virone, C., Kramer, H. J., van Rosmalen, G. M., Stoop, A. H., & Bakker, T. W. (2006). Primary Nucleation Induced by Ultrasonic Cavitation. *Journal of Crystal Growth, 294*, 9-15.

Wannasin, J., Martinez, R. M., & Flemings, M. C. (2006). Grain Refinement of an Aluminum Alloy by Introducing Gas Bubbles During Solidification. *Scripta Materialia, 55*, 115-118.

Weinberg, M. C., & Subramanian, R. S. (1980). Dissolution of Multicomponent Bubbles. *Journal of the American Chemical Society, 63*, 527-531.

Westervelt, P. J. (1953). The Theory of Steady Rotational Flow Generated by a Sound Field. *Journal of the Acoustical Society of America, 25*, 60-67.

Willard, G. (1953). Ultrasonically Indiced Cavitation in Water: A Step-by-Step Process. *The Journal of the Acoustical Society of America, 25*, 669-686.

Wilt, P. (1986). Nucleation Rates and Bubble Stability in Water - Carbon Dioxide Solutions. *Journal of Colloid and Interface Science, 112*, 530-538.

Xu, H., Han, Q., & Meek, T. T. (2008). Effects of Ultrasonic Vibration on Degassing of Aluminum Alloys. *Materials Science and Engineering A, 473*, 96-104.

Xu, H., Jian, X., Meek, T. T., & Han, Q. (2004). Degassing of Molten Aluminum A356 Alloy Using Ultrasonic Vibration. *Materials Letters, 58*, 3669-3673.

Yokoyama, E., Yoshizaki, I., Shimaoka, T., Sone, T., Kiyota, T., & Furukawa, Y. (2011). Measurements of Growth Rates of an Ice Crystal from Supercooled Heavy Water under Microgravity Conditions: Basal Face Growth Rate and Tip Velocity of a Dendrite. *Journal of Physical Chemistry B, 115*, 8739-8745.

Young, R. F. (1989). *Cavitation.* London: McGraw-Hill Book Company.

Yount, D., Gilary, E., & Hoffman, D. (1984). A microscopic investigation of bubble formation nuclei. *Journal of the Acoustical Society of America, 76*, 1511-1521.

Yu, D., Liu, B., & Wang, B. (2012). The Effect of Ultrasonic Waves on the Nucleation of Pure Water and Degassed Water. *Ultrasonic Sonochemistry, 19*, 459-463.

Yu, S., Feng, H., Li, Y., & Gong, L. (2009). Study on the Properties of Al–23%Si Alloy Treated by Ultrasonic Wave. *Journal of Alloys and Compounds, 484*, 360-364.

Yung, C.-N., De Witt, K. J., Brockwell, J. L., McQuillen, J. B., & Chai, A.-T. (1988). A Numerical Study of Parameters Affecting Gas Bubble Dissolution. *Journal of Colloid and Interface Science, 127*, 442-452.

Zhang, S., Liu, Z.-K., & Han, Q. (2008). Thermodynamic Modeling of the Succinonitrile-Water System. *Journal of Phase Equilibria and Diffusion, 29*, 247-251.

Zhang, S., Zhao, Y., Cheng, X., Chen, G., & Dai, Q. (2009). High-Energy Ultrasonic Field Effects on the Microstructure and Mechanical Behaviors of A356 Alloy. *Journal of Alloys and Compounds, 470*, 168-172.

Zhang, X., Inada, T., & Tezuka, A. (2003). Ultrasonic-Induced Nucleation of Ice in Water Containing Air Bubbles. *Ultrasonic Sonochemistry, 10*, 71-76.

Zhang, X., Inada, T., Yabe, A., Lu, S., & Kozawa, Y. (2001). Active Control of Phase Change for Supercooled Water to Ice by Ultrasonic Vibration 2. Generation of Ice Slurries and Effect of Bubble Nuclei. *International Journal of Heat and Mass Transfer, 44*, 4533-4539.

VITA

VITA

Milan Rakita earned degrees Master in Mechanical Engineering with minor in Manufacturing, and MSc in Mechanical Engineering with research area in Surface Engineering, all from University of Novi Sad, Faculty of Technical Sciences, in Novi Sad, Serbia. Prior to enrolling in the graduate studies at Purdue he worked at University of Novi Sad, Serbia, and Laboratory of Physics, Vinca Institute of Nuclear Sciences, Belgrade, Serbia. Some of the publications and the list of projects completed for Indiana-based companies and businesses are given below.

Journals

Rakita, M., Liu, Y., Yin, F., Wang, M., & Han, Q. (2013). Ultrasonic Shot Peening. *International Journal of Computational Materials Science and Surface Engineering, 5,* 189-209.

Liu, Z.W., Rakita, M., Han, Q., & Li, J.G. (2012). A Developed Method for Fabricating In Situ TiC_p/Mg Composites by Using Quick Preheating Treatment and Ultrasonic Vibration. *Metallurgical and Materials Transactions A, 43,* 2116-2124.

Liu, Z.W., Rakita, M., Han, Q., & Li, J.G. (2011). Microstructural Evolution of Reinforcements in the Remelting In Situ TiC/Al-12Si Composites Treated by Ultrasonic Vibrations, *Materials Research Bulletin, 46,* 1674-1678.

Kakaš, D., Škorić, B., & Rakita, M. (2004). Tribological Behavior of Duplex Coating Improved by Ion Implantation. *Thin Solid Films, 459,* 152-155.

Škorić, B., Kakaš, D., Bibić, N., & Rakita, M. (2004). Microstructural Studies of TiN Coatings Prepared by PVD and IBAD. *Surface Science, 566-568,* 40-44.

Škorić, B., Kakaš, D., Rakita, M., Bibić, N., & Peruško, D. (2004). Structure, Hardness and Adhesion of TiN Coatings Deposited by PVD and IBAD on Nitrited Steels. *Vacuum, 76,* 169-172.

Conference Proceedings

Rakita, M., Han, Q., & Liu, Z. (2013). Strain Rate as a Predictor of Hot Tearing Tendency in AZ 91 Magnesium Alloy. *AFS Transactions, 121*, 467-472.

Rakita, M., & Han, Q. (2009). Simulation of Solidification Defects for Prediction of Dross Formation in Aluminum 5182 Remelt Secondary Ingot. *Proceedings of the ASME International Manufacturing Science and Engineering Conference MSEC 2009 (West Lafayette, Indiana, USA),* pp.365-372.

Rakita, M., Kakaš, D., Škorić, B., Tomović, M., Han, Q., & Jackson, M. (2009). S-Type Cultivator Tines Which Comply With ISO Standard: FEM Analysis of Stresses and Manufacturing Issues. *Proceedings of the ASME International Manufacturing Science and Engineering Conference MSEC 2009 (West Lafayette, Indiana, USA),* pp. 373-380.

Škorić, B., Kakaš, D., & Rakita, M. (2005). Some Tribological Aspects of the Duplex Coatings with Additional Ion Bombardment. *Proceedings of the ASME World Tribology Congress (September 12-16, 2005, Washington, USA),* paper WTC2005-64218.

Kakaš, D., Rakita, M., Škorić, B., Novakov, T., Šiljegović, M., Dobrosavljević, A., Spasojević, V., Mitrić, M., & Ivković, B. (2005) Application of IBAD for Duplex Coating on Carburized Steel. *Proceedings of Vacuum Electron Ion Technologies VEIT (September 12-16, 2005, Sunny Beach, Bulgaria),* pp. 88.

Kakaš, D., Novakov, T., Škorić, B., & Rakita, M. (2005). Ion Beam Surface Modification of Different Tool Steels by Krypton Implantation. *Proceedings of Vacuum Electron Ion Technologies VEIT (September 12-16, 2005, Sunny Beach, Bulgaria)*, pp. 41.

Škorić, B., Kakaš, D., & Rakita, M. (2005). Structural, Mechanical and Tribological Behavior of TiN Coatings with Subsequent Ion Implantation. *Proceedings of the 11th European Conference on Applications of Surface and Interfaces Analysis (September 25-30, 2005, Vienna, Austria)*, pp. 112.

Rakita, M., Kakaš, D., Škorić, B., & Novakov, T. (2005). "Deposition of Industrial Scale Hard Coatings by IBAD", *Eight TESLA Workshop: Nanoscience and Biomedicine with Ion Beams (April 18-20 2005, Belgrade, Serbia)*, pp. 38

Škorić, B., Kakaš, D., & Rakita, M. (2004). Microstructural and Tribological Characterization of Duplex Coatings with Additional Ion Bombardment. *14th Congress of International Federation for Heat Treatment and Surface Engineering, (October 26-28, 2004, Shanghai, China)*, pp. 1229.

Kakaš, D., Škorić, B., & Rakita, M. (2004). Influence of Additional Ion Bombardment by Nitrogen on Characteristics of Duplex Coatings. *10th Joint Vacuum Conference, (September 18 - October 2, 2004, Portorož, Slovenia)*, pp. 47.

Škorić, B., Kakaš, D., & Rakita, M. (2003). "Influence of Ion Implantation on Wear Behavior of Duplex Coatings", *8th International Tribology Conference (October 8-10, 2003, Belgrade, Serbia)*, pp. 121.

Škorić, B., Kakaš, D., Bibić, N., & Rakita, M. (2003). Microstructural Studies of TiN Coatings Prepared by PVD and IBAD. *22th European Conference on Surface Science, (September 7-12, 2003, Prague, Czech Republic)*

Kakaš, D., Škorić, B., & Rakita, M. (2003). Tribological Behavior of Duplex Coating Improved by Ion Implantation. *8th European Vacuum Congress, (June 23-26, 2003, Berlin, Germany)*, pp. 158.

Škorić, B., Kakaš, D., Rakita, M., Bibić, N., & Peruško, D. (2003). Structure, Hardness and Adhesion of TiN Coatings Deposited by PVD and IBAD on Nitrited Steels. *International Summer School on Vacuum Electron Ion Technologies VEIT 2003 (September 15-19, 2003, Sunny Beach, Bulgaria).*

Engagement with Indiana-Based Companies and Businesses

1. Modification of the CPAP Oxygen/Air Valve Used in Emergency Medical Services
2. Rapid Tooling Technology for Manufacturing Dental Molds
3. Design of Balanced Air Flow Between Compartments of the Locker for Firefighters' Gear
4. Design of a Jig for Assembling Cable Reels
5. Selection of a Polymer or Polymeric Base Composite Material for the Ear Protector
6. Comparison of Consumption between Dishmaster® Faucet and Automatic Dishwashing Machines
7. Review of the Accelerated Wear Testing Method for Transmission Chains
8. Design Review and Calculations Pertaining to Piston Motion in the Algae Bioreactor
9. Finite Element and Analytical Stress Analysis of a Crane Assembly
10. Review of Specifications for Vibration Test
11. Finite Element Analysis of Stresses in the Polymer Electric Insulator and the Root Cause of Its Failure
12. Machine Design for Coating Nut Clusters with Chocolate
13. Synthesis of a Mechanism that Provides Short Stroke, High Force, and High Frequency Reciprocal Motion
14. Improving the Method of Fixing the Foam Slabs During Their Cutting
15. Analysis and Calculation of Strength and GDT of Spot Welded and Press Joints
16. Design of the Equipment for Automatic Unloading of Packaging Fixtures

17. Design of the Drying Cycle for Vending Machines
18. Automatic Knot Tying of Strings
19. Case Study of the Exhaust Fan Fracture
20. Stress Analysis and Safety Regulations for the Aerial Lift Vehicle
21. Modeling and Finite Element Analysis of Threads
22. Improvement of Tool-Life During the Machining of a Sandwich Composite Material
23. Analysis of Coated Tools for Machining Flywheels Made of Ductile Iron
24. Rapid Prototyping of a Bottle Cap with Two Ports
25. Implementation of Slitting Operations to the Equipment for Coating of Paper Rolls
26. Optimization of Safety Watch Design
27. Optimization of the Elevated Movable Cargo Tray for Vehicles
28. Design of the Casing for Equipment for Fast Forensics of Cell Phones
29. Design of Jigs for Drawers Assembly
30. Optimization of the Casting Process for the Piece 3345
31. Optimization of the Amaranth Popper
32. 3-D Scanning, Digitalization, and Modification of a Product
33. Optimization of the Aluminum Spinning Process
34. Design of Disposable Cup Holder Liner and Squeegee Handle for Cleaning Interior of a Rear Car Window
35. Design Optimization of a Tape Dispenser
36. Patentability Analysis of Two Products
37. Design of the Mechanism for Automatic Application of the Sticker on the Foam

Several additional projects on the optimization of metalcasting design